



Exploring the coupled ocean and atmosphere system with a data science approach applied to observations from the Antarctic Circumnavigation Expedition

Sebastian Landwehr¹, Michele Volpi², F. Alexander Haumann^{3,4}, Charlotte M. Robinson⁵, Iris Thurnherr^{6,7}, Valerio Ferracci⁸, Andrea Baccarini^{1,13}, Jenny Thomas⁹, Irina Gorodetskaya^{10,11}, Christian Tatzelt¹², Silvia Henning¹², Rob L. Modini¹³, Heather J. Forrer^{14,15}, Yajuan Lin^{16,17,18}, Nicolas Cassar^{16,17}, Rafel Simó¹⁹, Christel Hassler^{20,9}, Alireza Moallemi¹³, Sarah E. Fawcett¹⁴, Neil Harris⁸, Ruth Airs²¹, Marzieh H. Derkani²², Alberto Alberello²³, Alessandro Toffoli²², Gang Chen¹³, Pablo Rodríguez-Ros¹⁹, Marina Zamanillo¹⁹, Pau Cortés-Greus¹⁹, Lei Xue²⁴, Conor G. Bolas²⁵, Katherine C. Leonard^{11,26}, Fernando Perez-Cruz^{2,27}, David Walton^{4,†}, and Julia Schmale¹

¹Extreme Environments Research Laboratory, École Polytechnique Fédérale de Lausanne, Lausanne, Switzerland

²Swiss Data Science Center, ETH Zurich, Switzerland

³Atmospheric and Oceanic Sciences Program, Princeton University, Princeton, NJ 08540-6654, USA

⁴British Antarctic Survey, Cambridge CB3 0ET, UK

⁵Remote Sensing and Satellite Research Group, School of Earth and Planetary Sciences, Curtin University, Kent Street, Bentley, WA 6102, Australia

⁶Institute for Atmospheric and Climate Science, ETH Zurich, Switzerland

⁷Geophysical Institute, University of Bergen, and Bjercknes Centre for Climate Research, Bergen, Norway

⁸Centre for Environmental and Agricultural Informatics, School of Water, Energy & Environment Cranfield University, College Road, Cranfield MK43 0AL, Bedfordshire, UK

⁹Swiss Polar Institute, Lausanne, Switzerland

¹⁰Centre for Environmental and Marine Studies, Department of Physics, University of Aveiro, Aveiro, Portugal

¹¹Laboratory of Cryospheric Sciences, École Polytechnique Fédérale de Lausanne, Lausanne, Switzerland

¹²Leibniz Institute for Tropospheric Research, Leipzig, Germany

¹³Laboratory of Atmospheric Chemistry, Paul Scherrer Institute, Villigen, Switzerland

¹⁴Department of Oceanography, University of Cape Town, 7701, Cape Town, South Africa

¹⁵Earth, Ocean and Atmospheric Science Department, Florida State University, Tallahassee, FL 32306, USA

¹⁶Division of Earth and Climate Sciences, Nicholas School of the Environment, Duke University, Durham, NC 27708, USA

¹⁷Laboratoire des sciences de l'environnement marin, University of Brest, Brest, France

¹⁸Duke Kunshan University, Kunshan, Suzhou, Jiangsu, China

¹⁹Institut de Ciències del Mar (ICM-CSIC), Barcelona, Catalonia, Spain

²⁰Department F.-A. Forel for Environmental and Aquatic Sciences, University of Geneva, Geneva, Switzerland

²¹Plymouth Marine Laboratory, Plymouth PL1 3DH, UK

²²Department of Infrastructure Engineering, Faculty of Engineering and Information Technology, The University of Melbourne, Parkville, VIC 3010, Australia

²³Graduate School of Frontier Sciences, The University of Tokyo, Kashiwa, Japan

²⁴Department of Chemistry, College of Environmental Science and Forestry, State University of New York, Syracuse, NY 13210, USA

²⁵ITOPF Ltd., London EC1Y 1DT, UK

²⁶Cooperative Institute for Research in Environmental Sciences at the University of Colorado,
Boulder, CO 80309, USA

²⁷Department of Computer Science at ETH Zurich, Zurich, Switzerland

†deceased, 12 February 2019

Correspondence: Julia Schmale (julia.schmale@epfl.ch) and Sebastian Landwehr
(sebastian.landwehr@gmail.com)

Received: 22 March 2021 – Discussion started: 21 April 2021

Revised: 1 September 2021 – Accepted: 28 September 2021 – Published: 30 November 2021

Abstract. The Southern Ocean is a critical component of Earth’s climate system, but its remoteness makes it challenging to develop a holistic understanding of its processes from the small scale to the large scale. As a result, our knowledge of this vast region remains largely incomplete. The Antarctic Circumnavigation Expedition (ACE, austral summer 2016/2017) surveyed a large number of variables describing the state of the ocean and the atmosphere, the freshwater cycle, atmospheric chemistry, and ocean biogeochemistry and microbiology. This circumpolar cruise included visits to 12 remote islands, the marginal ice zone, and the Antarctic coast. Here, we use 111 of the observed variables to study the latitudinal gradients, seasonality, shorter-term variations, geographic setting of environmental processes, and interactions between them over the duration of 90 d. To reduce the dimensionality and complexity of the dataset and make the relations between variables interpretable we applied an unsupervised machine learning method, the sparse principal component analysis (sPCA), which describes environmental processes through 14 latent variables. To derive a robust statistical perspective on these processes and to estimate the uncertainty in the sPCA decomposition, we have developed a bootstrap approach. Our results provide a proof of concept that sPCA with uncertainty analysis is able to identify temporal patterns from diurnal to seasonal cycles, as well as geographical gradients and “hotspots” of interaction between environmental compartments. While confirming many well known processes, our analysis provides novel insights into the Southern Ocean water cycle (freshwater fluxes), trace gases (interplay between seasonality, sources, and sinks), and microbial communities (nutrient limitation and island mass effects at the largest scale ever reported). More specifically, we identify the important role of the oceanic circulations, frontal zones, and islands in shaping the nutrient availability that controls biological community composition and productivity; the fact that sea ice controls sea water salinity, dampens the wave field, and is associated with increased phytoplankton growth and net community productivity possibly due to iron fertilisation and reduced light limitation; and the clear regional patterns of aerosol characteristics that have emerged, stressing the role of the sea state, atmospheric chemical processing, and source processes near hotspots for the availability of cloud condensation nuclei and hence cloud formation. A set of key variables and their combinations, such as the difference between the air and sea surface temperature, atmospheric pressure, sea surface height, geostrophic currents, upper-ocean layer light intensity, surface wind speed and relative humidity played an important role in our analysis, highlighting the necessity for Earth system models to represent them adequately. In conclusion, our study highlights the use of sPCA to identify key ocean–atmosphere interactions across physical, chemical, and biological processes and their associated spatio-temporal scales. It thereby fills an important gap between simple correlation analyses and complex Earth system models. The sPCA processing code is available as open-access from the following link: <https://renkulab.io/gitlab/ACE-ASAID/spca-decomposition> (last access: 29 March 2021). As we show here, it can be used for an exploration of environmental data that is less prone to cognitive biases (and confirmation biases in particular) compared to traditional regression analysis that might be affected by the underlying research question.

1 Introduction

The Southern Ocean plays an important role in Earth's climate. Comparisons of climate models suggest that the 30 % of the global ocean surface south of 30° S strongly mitigates global surface warming. The region accounts for about 43 % of the uptake of anthropogenic CO₂ (labelled as (i) in Fig. 1) and 75 % of the excess heat uptake by global oceans (Frölicher et al., 2014). This substantial uptake of excess heat and CO₂ is due to the formation of large volumes of subsurface waters by subduction in this region (Fig. 1, (ii)), accounting for around 65 % of all global ocean subsurface water (DeVries, 2014). The Southern Ocean is not only responsible for the subduction of water masses, it is also the region where the deepest ocean waters return to the surface, accounting for about 80 % of the resurfacing of North Atlantic Deep Water and Antarctic Bottom Water (Talley, 2013) (Fig. 1, (iii)). Through this upwelling, it provides the surface ocean with important macronutrients, such as dissolved nitrate, phosphate, and silicate (Marinov et al., 2006). However, at the surface of the Southern Ocean itself, the consumption of these macronutrients through biological production is incomplete, due to the limited availability of iron, which determines the efficiency of the so-called biological carbon pump in this region (Tagliabue et al., 2017) (Fig. 1, (iv)). The unused macronutrients are then exported to lower latitudes, where they have been estimated to fuel about 75 % of the global ocean biological production (Sarmiento et al., 2004). While this overall important role of the Southern Ocean in the global climate system (through its ocean circulation and influence on the carbon and energy cycle) is widely accepted, very little is known about the local interactions between its components, i.e. the atmosphere, biosphere, sea ice, land, and ocean.

To explore interactions between the Southern Ocean system components, we apply an unsupervised learning method, sparse principal component analysis (sPCA). Application of the sPCA has two objectives: conducting an untargeted and therefore more objective analysis of data, where the method is less tailored to the science question as compared to more traditional regression analysis, and targeting a set of specific research questions (RQs).

RQ1. Is sparse principal component analysis an adequate tool to extract interaction processes inherent to a heterogeneous and temporally and spatially short dataset, which describes environmental variability?

RQ2. Is it possible to identify geographic locations (“hotspots”) that are common to several interaction processes?

RQ3. Which are the key observed environmental variables that strongly contribute to several interaction processes?

Specific answers to RQ1 are given in Sect. 3.5 with respect to model limitations and advantages and Sect. 5.2 with re-

spect to interaction processes. RQ2 is answered in Sect. 5.1, and RQ3 is answered in Sect. 5.3. Note that we focus on the proof of concept of the sparse principal component method by basing the interpretation primarily on the known processes of the Southern Ocean climate system. New scientific insights from this novel approach are described in Sect. 4.1.

1.1 Southern Ocean processes

The exchange of heat, freshwater, momentum, and chemical species (e.g. in the form of trace gases such as CO₂, dimethylsulfide, and aerosols) in the Southern Ocean is determined by the complex interaction of the atmosphere, ocean, land, ice, and microbial communities (Fig. 1). Between 40 and 60° S, the strong westerly wind belt develops nearly unhindered by land masses (Fig. 1, (v)), making the Southern Ocean the stormiest and fiercest ocean in the world (Hanley et al., 2010; Derkani et al., 2021). Winds and waves strongly modulate ocean mixing (Thorpe, 2007; Toffoli et al., 2012), biological production (Nicholson et al., 2016; Uchida et al., 2020), air–sea gas exchange (Wanninkhof et al., 2009; Gruber et al., 2019), sea ice dynamics (Alberello et al., 2020; Vichi et al., 2019; Holland and Kwok, 2012), and sea spray emission (Fig. 1, (vi)) relevant for cloud formation (Schmale et al., 2019; Quinn et al., 2017; Bigg, 1973). This storm track region is characterised by the frequent passage of extratropical cyclones leading to the formation of a quasi-persistent low-level cloud deck and regular precipitation (Fig. 1, (vii)) (Catto et al., 2012). Clouds can only form and persist when cloud condensation nuclei (CCN) and ice-nucleating particles (INPs) are present. Here, interactions between microbial activity and atmospheric chemistry come into play. Trace gas emissions from phytoplankton blooms can grow particles into the CCN size range (Fig. 1, (viii)) (Charlson et al., 1987; Pierce and Adams, 2006; Korhonen et al., 2008; Hoffmann et al., 2016; Schmale et al., 2019). The ocean–microbiology–atmosphere–cloud interactions strongly affect the radiation balance (Fig. 1, (ix)) and hydrological cycle of the region (Fig. 1, (x)) (Vergara-Temprado et al., 2018). To date, uncertainties in these processes contribute to biases in simulated cloud presence and lifetime, which lead to an overprediction of the ocean heat uptake in global climate models of up to 30 W m⁻² with implications on the regional energy balance, momentum transport, and ocean dynamics (Trenberth and Fasullo, 2010; Flato et al., 2013).

The presence of continents, islands, sea ice, and glaciers can strongly modify the local atmosphere–biosphere–ocean interactions, especially through their influence on ocean circulation and stratification, the marine boundary layer, and biological productivity. Islands can interrupt the zonal flow in the atmosphere and ocean, leading to horizontal and vertical mixing and transport (Rintoul, 2018). For example, hotspots of carbon and nutrient upwelling have been identified in close proximity to shallow ocean topography or islands (Fig. 1, (xi)) (e.g. Tamsitt et al., 2018). The supply of

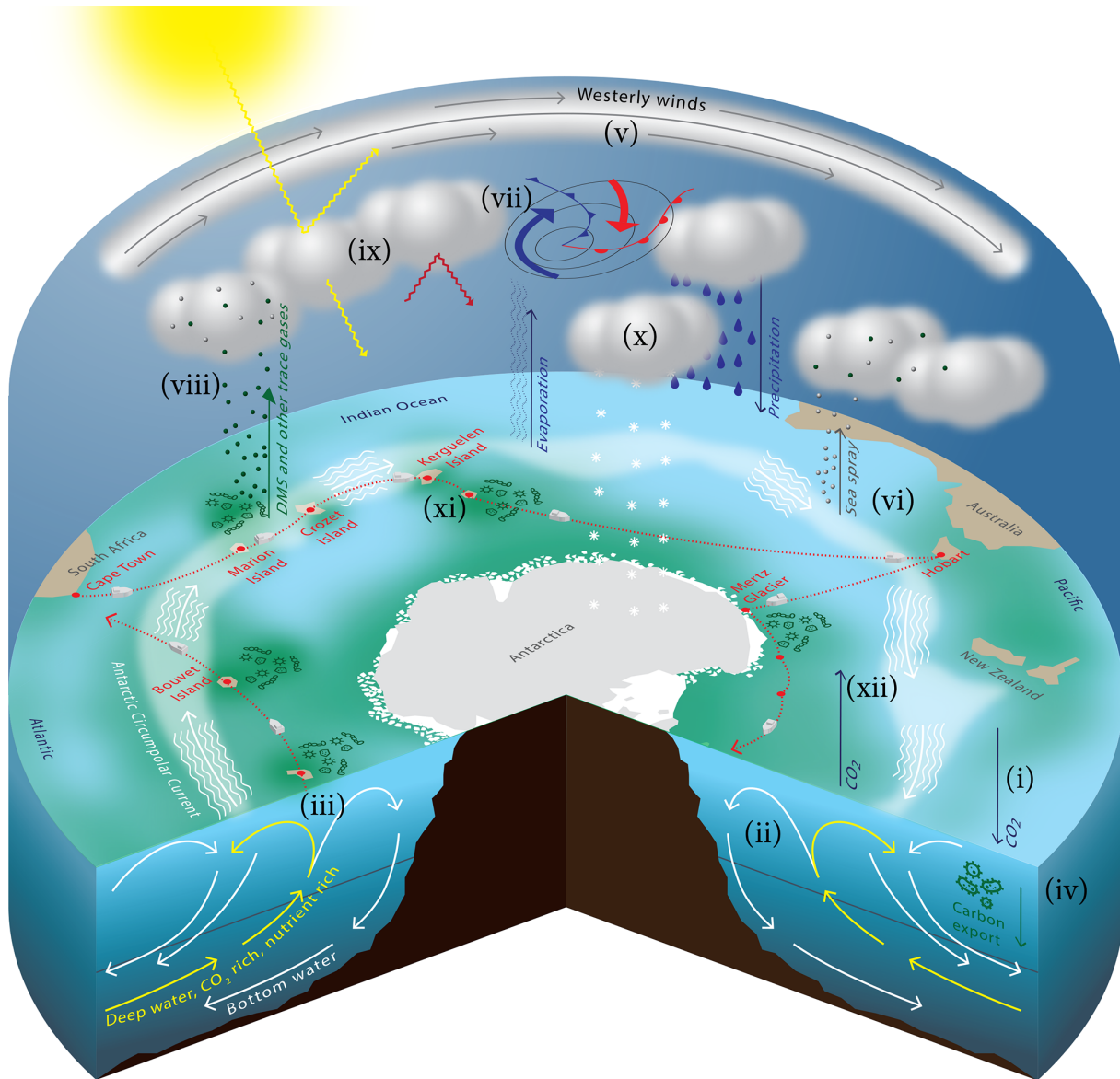


Figure 1. Conceptual illustration of selected Southern Ocean processes. The dashed red line represents the ACE cruise track. Letters indicate processes described in more detail in the introduction: (i) CO₂ uptake, (ii) formation of bottom water, (iii) upwelling of nutrient-rich water, (iv) biological carbon pump, (v) westerly storm track, (vi) formation of sea spray, (vii) cyclone activity and low-level cloud deck, (viii) emission of biogenic gases and secondary aerosol formation, (ix) cloud-modulated radiation budget, (x) evaporation and precipitation, (xi) nutrient (iron)-rich areas near islands through the island mass effect, (xii) meltwater inducing phytoplankton blooms.

iron from sediments or deep water can lead to hotspots of biological production in the close proximity to land masses and topographic features (e.g. Atkinson et al., 2001; Blain et al., 2007; Prend et al., 2019), which is known as the island mass effect (IME). Sea ice in the Southern Ocean forms and melts seasonally and alters the surface ocean stratification (Haumann et al., 2016), gas and heat exchange (Butterworth and Miller, 2016; Swart et al., 2019), and causes springtime blooms (Fig. 1, (xii)) (Uchida et al., 2019; Arteaga et al., 2020; Moreau et al., 2020). Due to the large number of pro-

cesses and their different spatial and temporal scales, a direct quantification of the processes that determine atmosphere–biosphere–ocean–ice–land interactions is challenging and requires large interdisciplinary datasets and new tools to analyse their covariance.

1.2 The expedition

In a single summer season the Antarctic Circumnavigation Expedition (ACE) (Walton and Thomas, 2018; Schmale et al., 2019) covered all three Southern Ocean basins, includ-

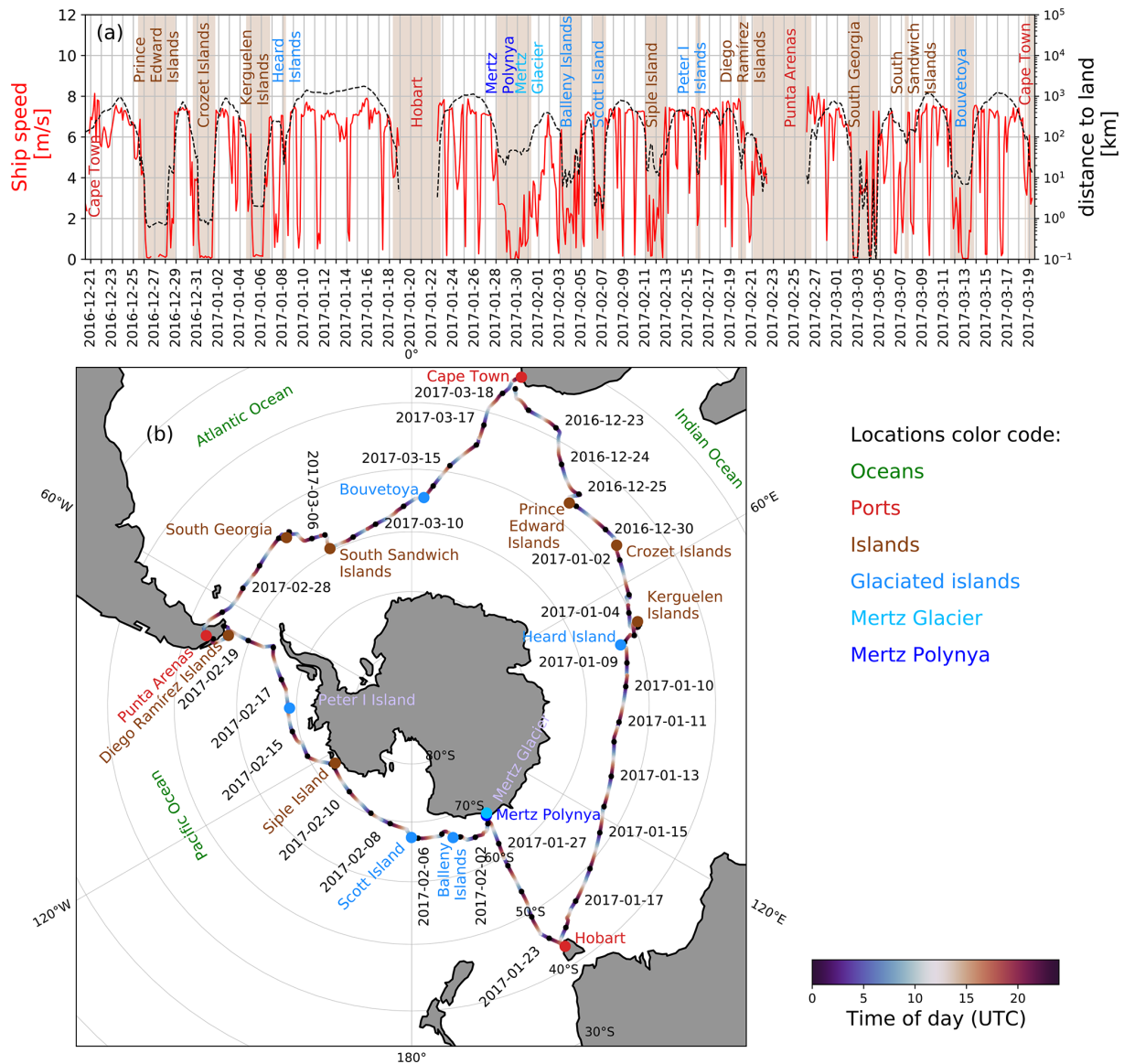


Figure 2. (a) Time series of the ship's speed (solid red line, left axis) and distance to land (dashed black line, right axis). Periods where the ship was within 100 km of the nearest land are indicated by brown shading, with the names of the locations provided. (b) Map of the ACE cruise track. Places visited by the ship (ports, islands, Mertz Glacier and Polynya) are marked and labelled with coloured bullets and text. The black dots and date ticks refer to the ship's position at midnight of the date specified (UTC), and time of UTC day is further indicated by the colour scale. Overlapping date ticks have been omitted for clarity.

ing visits to 12 remote islands, the marginal sea ice zone, and the Antarctic coast (Fig. 2). The in situ observations cover a wide range of variables related to the dynamic state of the ocean and the atmosphere, the freshwater cycle, atmospheric chemistry, ocean biogeochemistry, and microbiology. The dataset covers a large range of environmental conditions and process timescales; provides a unique opportunity for an interdisciplinary study to better understand the complex Southern Ocean system; and identifies relations between physical, chemical, and biological processes. Studying the above requires not only an interdisciplinary dataset

but also analytical tools capable of capturing the relations between the large number of original variables (OVs, i.e. observed and therefrom-derived variables), which vary over different spatial and temporal scales. In this work, we explore how a sparse matrix factorisation approach, i.e. sparse principal component analysis (sPCA), can connect these highly heterogeneous observations.

1.3 Unsupervised learning approach

Standard principal component analysis (PCA) (Hotelling, 1933) is a fundamental data analysis tool in many disciplines in the natural and environmental sciences. Also known as empirical orthogonal function (Denbo and Allen, 1984) in climate science and meteorology, it is mainly used to reduce the dimensionality of a dataset as a preprocessing step for further analyses and/or for visualisation (Demsar et al., 2013). Observations are treated as points in a multidimensional space, with each dimension representing an OV. The PCA rotates the input data so that the new axes, the principal components, are aligned to the direction of maximal variance. These dimensions are also known as latent variables (LVs). In practice, LVs can be seen as artificial output variables returned by the PCA algorithm that are linear combinations of the input OVs, i.e. the actual measurements. Therefore, LVs are the target variables that we aim to interpret in this study, where each LV summarises a specific aspect of the data, which we relate to natural processes. This approach has the advantage of reducing many OVs to a few LVs that we can interpret in terms of the processes that they represent. However, despite its value in providing uncorrelated LVs and summarising data variance in a few principal components, PCA decompositions are hard to interpret, due to the potentially large number of input variables that contribute to the definition of the LVs (i.e. OVs, which have non-zero entries in the weight matrix). Common attempts to interpret PCA relate the direction of the principal components to the input variables and assign them a user-defined meaning. Since it is difficult to do so for more than two or three dimensions, typically only a few dominant LVs are analysed, while LVs explaining the total variability only marginally are neglected. A caveat is also that PCA tends to fail when the number of OVs is very large or larger than the number of data points (Zou et al., 2006). These challenges are alleviated when using sPCA, where only a subset of the most informative OVs is used to construct each LV, while the remaining weights are forced to be zero, resulting in a sparse weight matrix. The OVs with non-zero weights form a subset (a cluster) of variables that are related to each other and compose a specific LV, which can be interpreted with one or several underlying processes. The information as to which OVs contribute to each LV, and in particular those which do not, greatly simplifies the interpretation of the LVs. Sparse PCA has found notable applications, amongst others, in genomics (Lee et al., 2010), ecology (Gravuer et al., 2008), biology (Li et al., 2017), and neuroscience (Baden et al., 2016). In all settings, sPCA can be used as a drop-in replacement for standard PCA, leading to decompositions with much-improved interpretability. In this work, we extend the sPCA framework by empirically estimating a bootstrapped distribution of sPCA weights and corresponding LVs, providing confidence intervals around measures of interest. We apply sPCA to a dataset of 111 OVs from the Antarctic Circumnavigation Expedition and choose

to obtain 14 LVs, which connect observations across the disciplines involved and serve as a basis for the exploration of processes described by the data.

Section 2 briefly describes the datasets used in this study. We elaborate on the sPCA approach in Sect. 3 and introduce the resulting LVs in Sect. 4. Detailed discussions of individual LVs can be found in Appendix A. In Sect. 5, we discuss the LVs in conjunction with regional phenomena and geographical hotspots and provide a synthesis of the findings. Our conclusions are provided in Sect. 6.

2 Data

2.1 The Antarctic Circumnavigation Expedition

The Antarctic Circumnavigation Expedition (ACE) (Walton and Thomas, 2018; Schmale et al., 2019) fully circumnavigated the Antarctic continent between 34 and 78° S aboard the RV *Akademik Tryoshnikov* during a single austral summer from 20 December 2016 to 18 March 2017. Figure 2a shows the time series of the ship speed and distance to land and Fig. 2b shows a map of the cruise track. Leg 1 of the expedition started in Cape Town, South Africa, from which the ship travelled through the Indian Ocean sector of the Southern Ocean to Hobart, Australia. Leg 1 featured open-ocean conditions with rough seas and the highest wind speeds encountered during the expedition. The expedition visited three remote islands: Marion Island (one of the Prince Edward Islands), the Crozet Islands, and Kerguelen Island during leg 1. During leg 2, from Hobart through the Pacific sector of the Southern Ocean to Punta Arenas, Chile, the ship stayed mostly close to the Antarctic continent, spending several days at the Mertz Glacier and explored the area that was previously covered by the glacier tongue that had broken off in February 2010 (Campagne et al., 2015). The expedition then visited the Balleny Islands, Scott Island, Siple Island, as well as the Marie Byrd Land coast, which was possible due to the unusual lack of sea ice in this region, before progressing to Peter I Island. Sailing northward along the west coast of the Antarctic Peninsula and across the Drake Passage, the expedition visited the Diego Ramírez Islands before reaching Punta Arenas. During leg 3, the ship returned through the South Atlantic back to Cape Town and visited South Georgia, the South Sandwich Islands, and Bouvetøya Island. In addition to these numerous sites, the expedition encompassed all the biogeochemical regimes of the Southern Ocean (Janssen et al., 2020), including the subtropical and subantarctic zones and areas south of the polar front, representing vast regions where primary productivity is known to be largely limited by the micronutrient iron. Much of the time was also spent along the Southern Ocean storm track between 40 and 60° S, with frequent passages of cyclones (Simmonds et al., 2003; Papritz et al., 2014). This region of cyclones is also responsible for a limited influence of anthropogenic air pollutants from the inhabited continents, making the visited region one of the

most pristine atmospheric regimes on Earth (Hamilton et al., 2014; Schmale et al., 2019). The expedition offered the possibility of studying the effect of weather systems on sea spray aerosol and trace gas concentrations in one of the fiercest environments on Earth (Hanley et al., 2010; Landwehr et al., 2020). Altogether, ACE provides a unique picture of the heterogeneous environmental conditions that characterise the Southern Ocean.

Generally, all atmospheric measurements were taken from either the container or monkey deck, i.e. 15 m and up to 31.5 m above sea level, respectively. Ocean measurements were either obtained from the underway water line, with an intake at the front of the ship at about 4.5 m below sea level, or from conductivity, temperature, depth (CTD) casts. Details of the sampling locations are given in the cruise report (Walton and Thomas, 2018), whereas details of the measurement methodologies are given in the Supplement Sect. S1.

2.2 Original variables and categories

In this section, we provide a short overview of the observed and variables derived therefrom, which are referred to as original variables (OVs). To present the OVs and to facilitate interpretation of the results, we assigned the variables to eight summary categories based on processes and phenomena they are associated with. The categories were defined by consensus among the authors, are intended to orient the reader, and are used for a more generalised presentation of the correlation structures in the ACE datasets, which have been identified by the sPCA analysis. To facilitate this, a colour is assigned to each category (see Fig. 6). Table 1 lists the categories and provides the symbols of the variables contained in each category. The OVs themselves are summarised in the Appendix tables, from Table B3 to Table B8, which provide the OV ID, the variable symbol, SI units, a description of the variable and the DOI of the published dataset, or a reference to the Supplement Sect. S1, where details on measurement methods and variable derivations are provided. Further, we provide a glossary for each OV, i.e. a brief description for a quick look-up, in the Appendix F. We assigned an ID to each of the 111 variables, e.g. wind speed (u_{10N}) is the original variable 1 (OV1). Both symbols and OV IDs are used in the figures.

3 Methods

3.1 Sparse principal component analysis (sPCA)

Sparse PCA, an unsupervised machine learning approach, was used to allow an easier interpretation of PCA solutions by encouraging weights (also known as principal directions in the PCA literature) to take values of exactly zero (Zou et al., 2006), while optimally summarising variance of the original data into a predefined number of components. Max-

imising data variance in a finite set of components guarantees minimal information loss in the solutions.

The standard PCA problem is formulated as follows (Hotelling, 1933):

$$\mathbf{U}_{\text{PCA}}, \mathbf{V}_{\text{PCA}} = \min_{\mathbf{U}, \mathbf{V}} \frac{1}{2} \|\mathbf{X} - \mathbf{UV}\|_2^2 \quad \text{subject to } \|\mathbf{V}\mathbf{V}^\top\| = \mathbf{I}, \quad (1)$$

which decomposes the original data matrix $\mathbf{X} \in \mathbb{R}^{N \times d}$, with N data points and d OVs, into a set of mutually orthogonal LVs (principal components) \mathbf{U} . \mathbf{I} is the $c \times c$ identity matrix, with c being the number of LVs. LVs are a linear combination of the original OVs and the assigned weights \mathbf{V} as $\mathbf{U} = \mathbf{X}\mathbf{V}^\top$, which are usually non-zero. It is therefore hard to unequivocally assign the importance of an OV to the composition of an LV. Note that \mathbf{X} is transformed into standard scores, i.e. centred to zero mean and reduced to unit standard deviation before optimisation.

Sparse PCA aims to solve a very similar problem but adds an additional constraint favouring some weights for each i th component (\mathbf{V}_i) to be exactly zero. Therefore, only a subset of the OVs contributes to the estimation of the corresponding LV \mathbf{U}_i . In these terms, the sPCA solution is obtained by:

$$\mathbf{U}_{\text{sPCA}}, \mathbf{V}_{\text{sPCA}} = \min_{\mathbf{U}, \mathbf{V}} \frac{1}{2} \|\mathbf{X} - \mathbf{UV}\|_2^2 + \lambda \|\mathbf{V}\|_1, \quad (2)$$

subject to $\|\mathbf{U}_i\|_2 = 1 \forall i$.

Due to the addition of the ℓ_1 norm ($\|\mathbf{V}\|_1$; i.e. the sum of the absolute of the components of \mathbf{V}) to the optimisation objective, the optimum can only be achieved when many of the weights of \mathbf{V}_i are zero, hence promoting sparsity. Sparsity is obtained automatically as the solution of Eq. (2) leads to the selection of the smallest possible subset of OVs to maximise the variance of the LV. We employ the efficient solver presented in Mairal et al. (2009) as implemented in the scikit-learn sparse PCA module (Pedregosa et al., 2011).

The model hyperparameter λ in Eq. (2), whose value is chosen by the user, controls how much the ℓ_1 norm participates in the definition of the optimum, i.e. it controls how sparse the solutions are. The other hyperparameter to be set is the number of LVs c .

The standard PCA has the ability to extract 100% of the data variance when considering a number of LVs that is equal to the number of OVs. While at a first glance this might be a strength of the standard PCA, in fact this comes at the cost of having typically a large number of small weights associated to OVs, which makes it difficult to unambiguously select a subset (or cluster) of OVs relevant for a specific LV. By using the sPCA approach presented here, the algorithm instead optimises these weights so that some are exactly zero. This approach makes it possible to interpret groups of OVs that contribute to any given LV and their association strength by looking at the subset of OVs with non-zero weights. Note that if one would discard OVs associated with small weights in standard PCA solutions, the explained variance would decrease and there is no guarantee that the resulting LVs are as

Table 1. Categories used to classify the original variables. The columns provide the name of the category and the abbreviation, and a list of the OVs, which were assigned to the category. The OV symbols are explained in Appendix Tables B1 to B8 (see Appendix B).

Category name (abbreviation)	Variables in the category
Atmospheric dynamics and thermodynamics (Atm. dyn.)	u_{10N} ; T_{air} ; S_{in} ; P_{air} ; PAR; mask _{CW} ; mask _{cyc}
Atmospheric side of the hydrological cycle (Atm. hydro.)	visibility; CL; SC; RH; $\delta^{18}O_{vap}$; δ^2H_{vap} ; dex_{cvap} ; w ; RR; SR; HHF
Atmospheric chemistry (Atm. chem.)	CH ₄ ; CO ₂ ; CO; O ₃ ; $N_{CCN,0.15}$; $N_{CCN,0.30}$; $N_{CCN,1.00}$; $\kappa_{CCN,0.15}$; $\kappa_{CCN,0.30}$; $\kappa_{CCN,1.00}$; H ₂ SO ₄ ; HIO ₃ ; MSA; SO ₄ ²⁻ ; Cl ⁻ ; $N_{INP,LV,-8}$; $N_{INP,LV,-20}$; $N_{INP,HV,-8}$; $N_{INP,HV,-20}$; $r_{fluo,fine3\sigma}$; $r_{fluo,coarse3\sigma}$; N_{Aitken} ; $N_{accumulation}$; $N_{seaspray}$; $N_{nitrate,PM_{10}}$; $N_{oxalate,PM_{10}}$; $N_{bromide,PM_{10}}$; $N_{MSA,PM_{10}}$; $N_{sodium,PM_{10}}$; $N_{ammonium,PM_{10}}$; $N_{potassium,PM_{10}}$; $N_{magnesium,PM_{10}}$; $N_{calcium,PM_{10}}$; Isoprene _{air}
Oceanic dynamics and thermodynamics (O. dyn.)	I_g ; H_s ; $T_{m-1,1}$; T_{sw} ; $\sigma_{0,sw}$; SSH; U_g ; MLD
Oceanic side of the hydrological cycle (O. hydro.)	S_{sw} ; C_i ; $\delta^{18}O_{sw}$
Ocean microbial community (O. microb.)	Chlide a ; Phaeob a ; Phaeophy a ; PSD _{slope} ; FvFM; Φ_{PSII}' ; σ_{PSII} ; σ_{PSII}' ; TChl a ; Chloro; Crypto; Cyano; DiatA; DiatB; Dino; Hapto8; Hapto67; Prasino; Pelago; Chl a_{fluo} ; $N_{totalbacteria}$; $N_{synechococcus}$; $N_{nanoeukaryotes}$; $N_{picoeukaryotes}$
Ocean biogeochemistry (O. biogeochem.)	POC; PON; C : N; Nitrate; Nitrite; Phosphate; Silicate; a_{nap}/a_p ; $a_{napslope}$; a_{CDOM} ; DMS; CSO; CS ₂ ; Isoprene _{sea} ; CHBr ₃ ; CH ₂ Br ₂ ; acrylate; DMSP; TEP; CSP; Ammonium; NCP
Topography (Topo.)	d_{land} ; d_{water}

different from each other as possible and therefore contain the least redundant information. In practice, sPCA optimises this thresholding process.

3.2 Estimation of statistical uncertainty using bootstrapping

Bootstrapping provides a robust approximation of the statistics by resampling the available data and computing measures of interest several times from the subsamples. We use this strategy to combine different sPCA solutions, which are based on subsamples of the dataset, and obtain an empirical distribution over the sPCA weights (\mathbf{V}) and corresponding LVs (\mathbf{U}). From the empirical distributions, we extract median, mean, median absolute deviation, and standard deviation to assess the robustness of the solutions with respect to noise and data outliers.

When running the sPCA optimisation, i.e. solving Eq. (2), on a given random subset of data points, the solutions differ typically in the order of the components, the magnitude of weights, and the explained variance. Also, the sign of the weights can be arbitrarily flipped for each solution: with the sign of the LVs flipped accordingly, however, the explained variance does not change. To compute statistics from the bootstrap runs, one must first align the different solutions in a meaningful way without losing the intrinsic variability brought by the bootstraps. Note that for every bootstrap the

value distribution of each OV varies and so does the influence of noise, and thus one cannot expect components across different sPCA bootstraps to be aligned directly, for instance according to their order or the amount of explained variance, as this value can vary.

For this work, we propose an approach based on alignment and thresholding. We first ran the sPCA on the full dataset, which we named “main” run. This first sPCA decomposition provides an ordered set (ordered by explained variance) of LVs and corresponding weights, which was used as reference for the alignment of the sPCA bootstraps. Next, we computed as many sPCA models as there are bootstraps, where each one of them relies on a random subset of the original data points. Each solution is then aligned to the main run components by a two-fold strategy. First, we tested whether it was necessary to invert the signs of the sPCA runs. To do so, we computed the correlation between the main sPCA run and each component from each bootstrap. All bootstraps that were clearly negatively correlated with any of the main run LVs were flipped in sign (remember that sign is arbitrary). Subsequently, for each LV from the main run, we computed a similarity score defined by a radial basis function (RBF):

$$s(\mathbf{V}_i, \mathbf{V}_j) = \exp \frac{-d(\mathbf{V}_i, \mathbf{V}_j)}{2 \cdot \bar{u}^2}, \quad (3)$$

where \bar{u} is the median Euclidean distance for all the pairs of weight vectors considered. Following this, the compo-

ment being the most similar and showing a similarity score above 0.5 was taken from each bootstrap and assigned to the ID of the main LV (note that $s(\mathbf{V}_i, \mathbf{V}_j) \in [0, 1]$, where 1 implies $\mathbf{V}_i = \mathbf{V}_j$). Bootstrapped statistics are obtained from these alignments. We report mean and standard deviations of weights and LVs but also the mean and standard deviation of the explained variance scores coming from each bootstrap. Note that some LVs might be derived from a number of aligned bootstraps lower than the total number of bootstraps. In that case, results might statistically be less robust, although we did not observe significant changes in statistical moments when using more bootstraps. Therefore, we also report the number of aligned bootstraps for each component.

This heuristic approach has three main benefits: first, the main run is only used as an alignment basis, and it does not influence bootstrap statistics. We made the assumption that noise does not strongly influence the main solution, at least in the first and most informative LVs. If components were driven by noise, the bootstrapped solutions would be dissimilar enough to prevent meaningful alignment. Secondly, the alignment to a main component avoids testing all the possible pairings, significantly simplifying the problem and greatly reducing the choice of potential matches. Finally, note that the set of LVs for every bootstrap is almost orthogonal. The orthogonality simplifies the selection of components based on the RBF similarity measure, as for every main component, at most one component from every bootstrap will be selected with $s(\mathbf{V}_i, \mathbf{V}_j) > 0.5$. However, as a result, the final set of averaged LVs might show higher correlations than the LVs of the individual bootstrap runs. The highest correlations between the averaged LVs was between LV1 and LV14 ($R^2 = 0.73$, Fig. C1a in Appendix C). A permutation test finds a p value of 0.0002 for that specific correlation (Fig. C1b in Appendix C). We used a nonparametric permutation test since the LVs are not normally distributed, as underlined by a normality test. However, note that none of the weight vectors corresponding to each LV shows significant correlations, as expected. Correlation between LVs can be expected, as different and potentially independent causes can show activations at similar positions in space and time.

3.3 Missing data and imputation

Most of the OV_s have gaps and missing data. To overcome the caveats of data gaps, we iteratively estimated missing data by inverting the sPCA model at the current iteration t , $\mathbf{X}^t \approx \mathbf{U}^{t-1} \mathbf{V}^{t-1}$. Using a derivation of the expectation maximisation method (Grung and Manne, 1998), we computed a first solution of the sPCA by replacing missing values with the sample mean, corresponding to zero after data standardisation as described below. By inverting the decomposition, we obtained a first guess reconstruction of the missing data, which is used to fill the gaps in the time series for the next iteration. This process is commonly referred to as data imputation. Note that the real observations are not altered in this

process. The reconstruction error is guaranteed to decrease (Grung and Manne, 1998), and we obtain the final decomposition after five imputation iterations. More iterations reduce the reconstruction error only marginally. The sparse decomposition affects the ability to reconstruct the variations over all the OV_s in the sense that OV_s associated with a zero weight over all LV_s cannot be accurately reconstructed.

3.4 Data preprocessing and model setup

Observations were recorded at various time resolutions, ranging from seconds in the case of wind speed to several hours for water samples taken from the underway sampling line (approximately every 6 h) and the 8 and 24 h aerosol filter samples (for some chemical compounds and ice nucleating particles). We chose to resample all observations to a 3 h resolution to obtain a uniform spatio-temporal grid along the cruise track. The raw data were first resampled to 3 h non-overlapping averages, regardless of the number of data points present in each 3 h window. This averaging smooths the data temporally, removing some high-frequency noise and fills missing observations on shorter time spans. Measurements and samples, which are available at a lower frequency, are assigned to the nearest 3 h window, leaving those windows which did not include an observation empty. The combined observations provide a data matrix $\mathbf{X} \in \mathbb{R}^{N \times d}$, with $d = 111$ columns for the original variables and $N = 710$ rows per time interval (at 3 h resampling).

Since we deal with very heterogeneous data, running the sPCA on the covariance between raw OV_s would provide a decomposition heavily influenced by OV_s showing wider dynamic ranges. In order to reduce the effect and harmonise the contribution of each OV, we renormalised the data to a common range (by computing standard scores) and a common probability distribution to reduce influence of heavy tails and outliers. Note that using standardised data corresponds to performing the sPCA on the correlation matrix rather than on the covariance. The distributions of the OV may be approximated with different distribution types: for example, aerosol number concentrations are often described with a lognormal distribution (Schmale et al., 2017); also some observations are better fitted by gamma distributions (Li et al., 2015); the wind speed is known to approximate a Weibull distribution (Hennessey, 1977); and rainfall may be best described with an exponential distribution (Woolhiser and Roldán, 1982). However, some variables show more complex multimodal distributions, e.g. water depth. Here, we classify the OV_s based on their distribution during ACE as either approximately normally or approximately lognormally distributed and apply a log transform in the latter case to obtain an approximately normal distribution (see the fifth column in the Tables B3 to B8 in Appendix B). Subsequently, we separately normalised each OV to standard scores by mean centring and reduction to unit standard deviations. For some OV_s, e.g. precipitation types (rain, snow, horizontal hydrometeor

flux), zero represents a valid observation, while at the same time they are better approximated by a lognormal distribution than by a linear distribution. Therefore, the actual zero values cannot be represented exactly by our preprocessing method. To avoid the loss of zero observations, we decided to replace these with a lower limit value (see Table D1 in Appendix D). Where available, we used the detection limit of the measurement device.

The model is optimised by extracting $c = 14$ principal components and using $\lambda = 1$. The c and λ values have been tuned by maximising the total explained variance, while maintaining the level of sparsity above $\frac{1}{3}$ of the number of OV. This rule of thumb led to interpretable results and has been kept. We ran five imputation iterations (see Sect. 3.3) and tested different input data resampling time intervals: 20, 180, and 720 min. Those intervals represent very short, medium, and long timeframes as compared to the sampling intervals of the OVs. We used 30 bootstraps to estimate the variations and observe that more do not lead to different estimates. Each bootstrap randomly samples 75 % of the available data with replacement. We did not tune this value but we expect its influence to be negligible if the number of bootstraps is set accordingly.

Our analysis pipeline can be summarised as follows: first, the measurements are preprocessed as described above in order to obtain the input OVs. Then, for each bootstrap, a random subset of data points is sampled, with replacement. This subset is used to compute an sPCA solution with the settings described above. Once all 30 bootstrap solutions are obtained, we perform the alignment of the principal components described in Sect. 3.2 and compute the distribution of the weights associated with each OV, the distributions of the LV activations, and the average explained variance per principal component. We then interpret these three outputs of the bootstrapped sPCA to understand the underlying natural processes that cause the variability described by each LV.

3.5 Model limitations and advantages

The main limitation of the proposed framework is that there is not an explicit underlying temporal model. Most phenomena show some level of smoothness in time, e.g. two observations acquired at short time intervals are more related than two observations acquired at times that are further apart. In our setting, after temporal resampling, we assume a data window is independent from all the others and our model does not provide a statistical representation of the temporal variations jointly to temporal evolution.

A second major limitation is the strict linearity assumption, as we are working on correlations. While this assumption might seem restrictive, we notice that large patterns in OV relationships can still be approximated by a simple linear function. Furthermore, linear models are much more robust to unquantified noise and ultimately easier to interpret thanks to the sparsity in the linear weights. We also notice that it

is difficult to develop a data-driven model evaluation, where numbers could objectively quantify the decomposition accuracy. However, as in most unsupervised learning tasks, there is no clear evaluation protocol. In this work, we rely on the evaluation of the correlations found by the model and how they compare to the current state of knowledge.

The data filling performed at the preprocessing step is complementary to the data imputation performed by sPCA. While the former is an independent data filling based on temporal averages, the latter can be seen as an estimation based on inverting the sPCA model on missing data, corresponding to a regression from non-missing OVs. The more correlated the OVs to the one containing a missing data point to be estimated, the better the estimation. The lower significance and correlations result in the tendency of assigning lower importance of sparsely measured OVs for the corresponding LVs. For example, the mixed-layer depth is only derived from the relatively sparse water column profile locations and therefore has a much lower temporal resolution compared to the other OVs in our dataset. As a consequence, it appears to be less important for air–sea exchange processes and biological production in our results, as one might expect. This issue is a clear limitation of our study that is important to consider when interpreting results. Therefore, the absence of a certain OV from our interpretation does not necessarily imply its absence in nature, but might be purely related to data scarcity. This limitation can be somewhat mitigated by running the model at lower temporal resolution (see Appendix E), but this would be at the expense of the information content of the denser time series.

The main advantage of the sPCA approach over its standard counterpart is the automatic selection of OVs by assigning non-zero weights for a given LV. The automatic optimisation of the weights associated with the OVs is done sequentially for each LV, starting from the one corresponding to the largest mode of variance. This ensures that all the LVs are as uncorrelated as possible, albeit not exactly. The use of sPCA has also the advantage of being less susceptible to noise and unimportant data variations. This advantage can be understood when contrasting the sPCA results with the large number of principal components with very low explained variance of the standard PCA. Although by considering these components the standard PCA is able to fully explain the data variance, such variance directions are of little practical use in our case, as it would be difficult to link them to natural processes. Compared to the standard PCA, sPCA is less likely to return components with very small explained variance, which are usually corresponding to noise. This advantage is further strengthened by our novel use of the bootstrap analysis, which promotes robustness to noise, meaning that OVs which contribute mainly through noise are identified as such. Data is resampled randomly, and the influence of noise can be observed in large fluctuations of the solution. Therefore, analyses relying on aggregated bootstrapped solutions are more robust to the influence of noise than the traditional

PCA or even a single run sPCA. Moreover, using sPCA over the standard PCA has also the benefit of not being susceptible to rank-deficient covariance matrices, in particular when the number of data points is smaller compared to the number of OV. Last, but not least, the exploratory character of the sPCA allows researchers to conduct an untargeted analysis and potentially find relationships or (spatial and temporal) patterns that would have been left undiscovered in a targeted analysis because one did not think of the possibility.

4 Sparse PCA results

4.1 Short summary of all latent variables and new insights

Figure 3 shows the time series of the 14 LVs, where the blue dots indicate the average of the principal components of the bootstrap runs and the shading indicates the 95 % confidence interval (± 2 standard deviations). The 14 LVs can be related to physical, biological and/or chemical processes, or changes in the environment that influence the variance of OV within each LV. We name each LV according to the process or environmental condition that they reflect (Table 2). These LV names result from our interpretation of what each LV represents as discussed in Appendix A. Overall, the sPCA solution describes 55 % of the variability of the 111 OV. Here we provide a short summary for all LVs, and in Sect. 4.2 we give an example description of LV9 focused on the marginal sea ice zone and snowfall. Detailed interpretations for each LV are provided in Appendix A.

The largest signal by far originates from the large-scale horizontal temperature and pressure gradients that exist between the low and high latitudes. The effect of these gradients on physical properties of the surface ocean and its activity are mostly captured in the two climatic zone signals (LV1 and LV14). The latitudinal temperature and pressure gradients give rise to the meridional advection of cold and warm air (LV3) with implications on cyclone activity (LV13) and the freshwater cycle with the intermittent character of precipitation events (LV4).

The sPCA led to some new insights into the Southern Ocean water cycle. We were able to systematically identify the different modes of variability in the isotopic signal of marine boundary layer water vapour. The OV $\delta^{18}O_{\text{vap}}$ and δ^2H_{vap} show significant contributions to climatological signals (LV1) and the relative humidity (RH) environment (LV3), while $dexc_{\text{vap}}$ mainly reflects the contrasting air–sea moisture fluxes in different RH environments. While an excess of precipitation over evaporation is generally thought to cause a relatively fresh Southern Ocean surface (Dong et al., 2008; Ren et al., 2011), surprisingly our large-scale assessment of concurrent precipitation and salinity measurements does not yield a direct response of the surface ocean salinity to precipitation events. Instead, we show that variations in surface ocean salinity are driven by the climatological (long-

term) patterns set by surface freshwater fluxes integrated over timescales longer than synoptic events (LV1) and seasonal melting on sea ice (LV9).

We also observe a latitudinal distribution of the nutrient availability and its effect on the productivity, which is highlighted in LV11, LV6, and LV8. This confirms, at the largest scale ever reported, nutrient limitation regimes for the sub-antarctic front, south of the polar front, and associated with the island mass effect as previously reported (Pollard et al., 2002; Blain et al., 2007; Cassar et al., 2007; Weber and Deutsch, 2010). Moreover, the sPCA successfully decouples the high spatial and temporal variability of iron-limited (LV8) and iron-fertilised blooms (LV6) and their dependence on nutrient availability (LV11), helping to identify the macro- and micro-nutrients responsible for changes to the biogeochemistry and microbial community structure and the source of those nutrients, e.g. upwelling, aeolian deposition, or sea ice melt.

The method further highlights the effects of diurnal variability of solar forcing on phytoplankton photosynthetic efficiency and trace gas oxidation (LV10), the seasonal variation of the solar forcing on dissolved and atmospheric trace gas concentrations, and the seasonal cycle in microbial productivity (LV7). While the sPCA confirmed known seasonal trends for a number of relatively long-lived key atmospheric trace gases (methane, CO, and ozone), it produced unexpected results for some of the reactive trace gases, notably isoprene (LV7). This result points towards a complex interplay between the seasonality of emissions (sources) and seasonality of oxidation pathways (sinks), which, coupled with the potential effect of transport from terrestrial sources, paint a very complex picture for atmospheric isoprene in the Southern Ocean. Further future analysis is required to better understand these processes.

The sPCA solution also clearly highlights aerosol sources (especially for INP and fluorescent aerosol) on (or in the proximity of) islands and continents (LV5), which was previously not as evident (Moallemi et al., 2021). We observe a clear link between wind speed and sea state and the concentration of large sea spray aerosol (LV12), tying them to the most wind-driven regions of the Southern Ocean. In contrast to that, the smaller accumulation mode particles (LV2) are ubiquitous because of their long lifetime and the various source processes contributing to their abundance.

4.2 Example LV description: marginal sea ice zone and snowfall (LV9)

LV9 has a very distinct regional signal that is mostly active during leg 2 of the cruise, with a clear peak between 27 January and 2 February 2017 when the ship passed through sea ice while approaching and leaving the Mertz region (Fig. 4a and b), explaining about $3.4(\pm 0.6)\%$ of the variance of all 111 variables (Table 2). The largest contribution to this LV comes from the sea ice concentration (C_i), i.e. fraction of sur-

Table 2. List of the 14 LVs in the sPCA solution. The columns denote the LV-ID (ranked by total variance explained by the master solution), the LV title, the number of matching LVs found in the 30 bootstrap runs, the variance explained by the LV, and the mean and standard deviation of the variance explained by the bootstrap runs.

ID	LV title	Bootstrap matches	Explained var. master run	Explained var. bootstrap runs
LV1	Climatic zones and large-scale horizontal gradients	30	9.2 %	9.5(±0.6) %
LV2	Drivers of cloud condensation nuclei population	30	4.6 %	4.4(±0.5) %
LV3	Meridional cold and warm-air advection	30	4.5 %	4.8(±0.4) %
LV4	Precipitation vs. dry conditions	30	4.4 %	3.9(±0.6) %
LV5	Distance to land	30	4.0 %	4.0(±0.3) %
LV6	Iron-fertilised biological productivity	30	3.7 %	3.8(±0.4) %
LV7	Seasonal signal	30	3.5 %	3.5(±0.2) %
LV8	Iron-limited biological productivity	30	3.4 %	3.5(±0.3) %
LV9	Marginal sea ice zone and snowfall	29	3.2 %	3.4(±0.6) %
LV10	Diel cycle	30	3.1 %	3.2(±0.2) %
LV11	Surface nutrient concentrations associated with mixing events and climatic and frontal zones	25	3.1 %	2.9(±0.4) %
LV12	Wind-driven conditions and sea spray aerosol	30	3.1 %	3.2(±0.4) %
LV13	Extratropical cyclone activity	25	2.7 %	2.6(±0.2) %
LV14	Climatic zones with local high-latitude hotspots	25	2.6 %	3.2(±1.4) %

face area covered by sea ice (Fig. 4c), which was unusually low during the austral summer season 2016/2017 (Schlosser et al., 2018).

The sPCA highlights four interesting characteristics of the coupled ocean, ice, and atmosphere system in the melting sea ice region. Firstly, positive LV9 periods are associated with a low surface ocean salinity (S_{sw}) and density ($\sigma_{0,sw}$; Fig. 4c). These relatively fresh and light surface waters suggest a stable surface ocean stratification associated with recently melted sea ice, confirming previous observations (Haumann et al., 2016). While other surface freshwater fluxes such as snow and glacial melt could have been responsible for the low-salinity surface ocean, the absence of a low $\delta^{18}O_{sw}$ in LV9 suggests no significant contribution of these fluxes. A second interesting observation is the large contribution of the wave period ($T_{m-1,1}$) to LV9 (Fig. 4c), with a significantly longer wave period in the partially ice-covered region when LV9 is positive. Therefore, the sPCA confirms that ice floes in the marginal ice zone dissipate wave energy (Squire, 2020; Arduin et al., 2020) with a faster rate for short-wave components of the spectrum (Meylan et al., 2018). Thirdly, net community production (NCP) and phytoplankton biomass (Chl a_{flu0}) are both positively correlated with LV9. Therefore, the sea ice melt appears to increase the water column productivity, most likely through iron fertilisation (Lannuzel et al., 2008, 2016) and/or enhanced water column stratification, relieving light limitation (Vernet et al., 2008; Cassar et al., 2011; Eveleth et al., 2017). A fourth aspect of LV9 is the large contribution of snowfall (SR). While a higher snowfall compared to rainfall is expected near the Antarctic coast in summer, it is unclear if there is a link between snowfall and the presence of sea ice in LV9 – an aspect

that requires further investigation. However, the sPCA suggests an atmospheric boundary layer over sea ice that is dominated by Antarctic continental air masses near the surface with moist and warm advection aloft (see back trajectories in Supplement Sect. S4) producing snowfall at times. Antarctic air masses near the surface in LV9 are indicated by the very low abundances of heavy water molecules (δ^2H_{vap} and $\delta^{18}O_{vap}$) in the atmospheric water vapour (w), and a low carbon monoxide (CO) concentration. The presence of sea ice thus helps to maintain Antarctic air masses properties over the ocean by forming a barrier between the ocean and the atmosphere, limiting the influence of surface fluxes on the air mass before it reaches the open ocean (see, e.g. Renfrew and Moore, 1999). Therefore, the sea ice influences the vertical atmospheric boundary layer structure, possibly favouring snowfall.

4.3 Latent variable timescales

We characterise the spatio-temporal variabilities captured by the LVs by a frequency analysis (see Fig. 5, which shows the periodogram of the LV series). Note that because the ship was mostly moving, spatial variability will appear as temporal variability and this needs to be taken into account when interpreting results. We can classify the LVs based on their peak period or spectral ranges of high activity: the 1 d period of LV10 is most obvious and reveals the relation of this LV to the diurnal cycle (solar radiation). The spectra of LV1 (climatic zones), LV5 (distance to land), and LV14 (Climatic zones with local high-latitude hotspots) have a distinct peak at a period of 30 d, which is about one-third of the total duration of the cruise and reflects the repeated travel from north to south and from continental influences to remote open-ocean

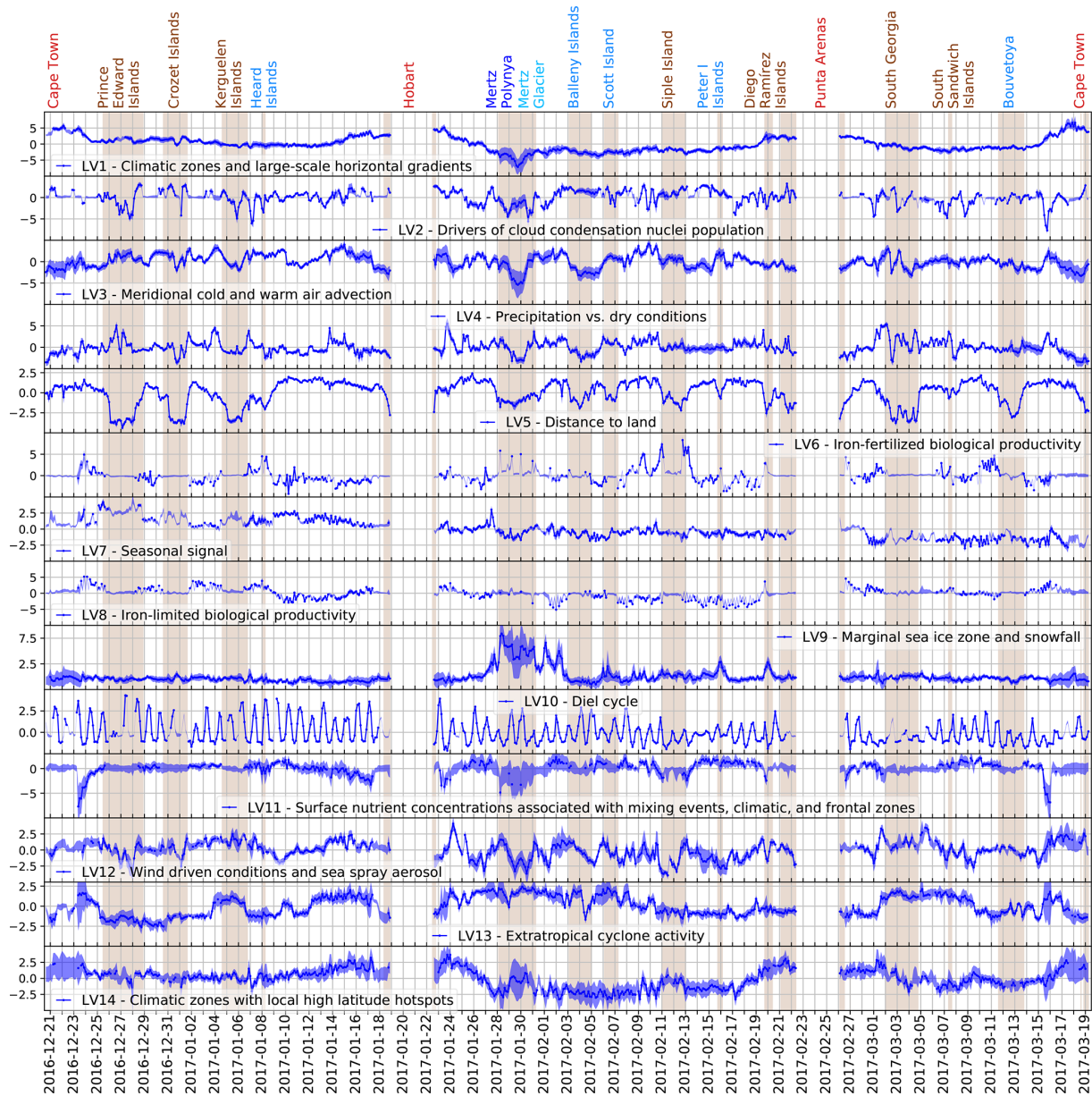


Figure 3. Time series of LVs. Each time series (blue dots) is calculated as the average of the principal components of the bootstrap runs, and the standard deviation (SD) is used to estimate the 95 % confidence interval as $\pm 2SD$. Mean activation of the LV is only shown if more than 50 % of the OV with the 50 % largest weights were observed. Brown shading indicates periods when the ship was within 100 km of the nearest shore. Places visited (ports, islands, and the Mertz Glacier and Polynya) are indicated at the top.

conditions during the three legs. Several LVs (LV3, LV12, LV4, LV11) show enhanced activity at approximately 3 to 10 d periods, which is related to synoptic timescales. For the remaining LVs most variations occur at periods longer than 10 d.

4.4 Contribution of the original variables to the latent variables

Figure 6 shows how much individual OVs contribute to different LVs. Most OVs co-vary with more than one LV, and all LVs are related to OVs from multiple OV categories as defined in Sect. 2.2 with the colour scheme shown in Fig. 6. Single OV contributions to the LVs are controlled by the sPCA weights. We represent them by plotting the explicit distribution obtained through bootstrapping as boxplots. Fig-

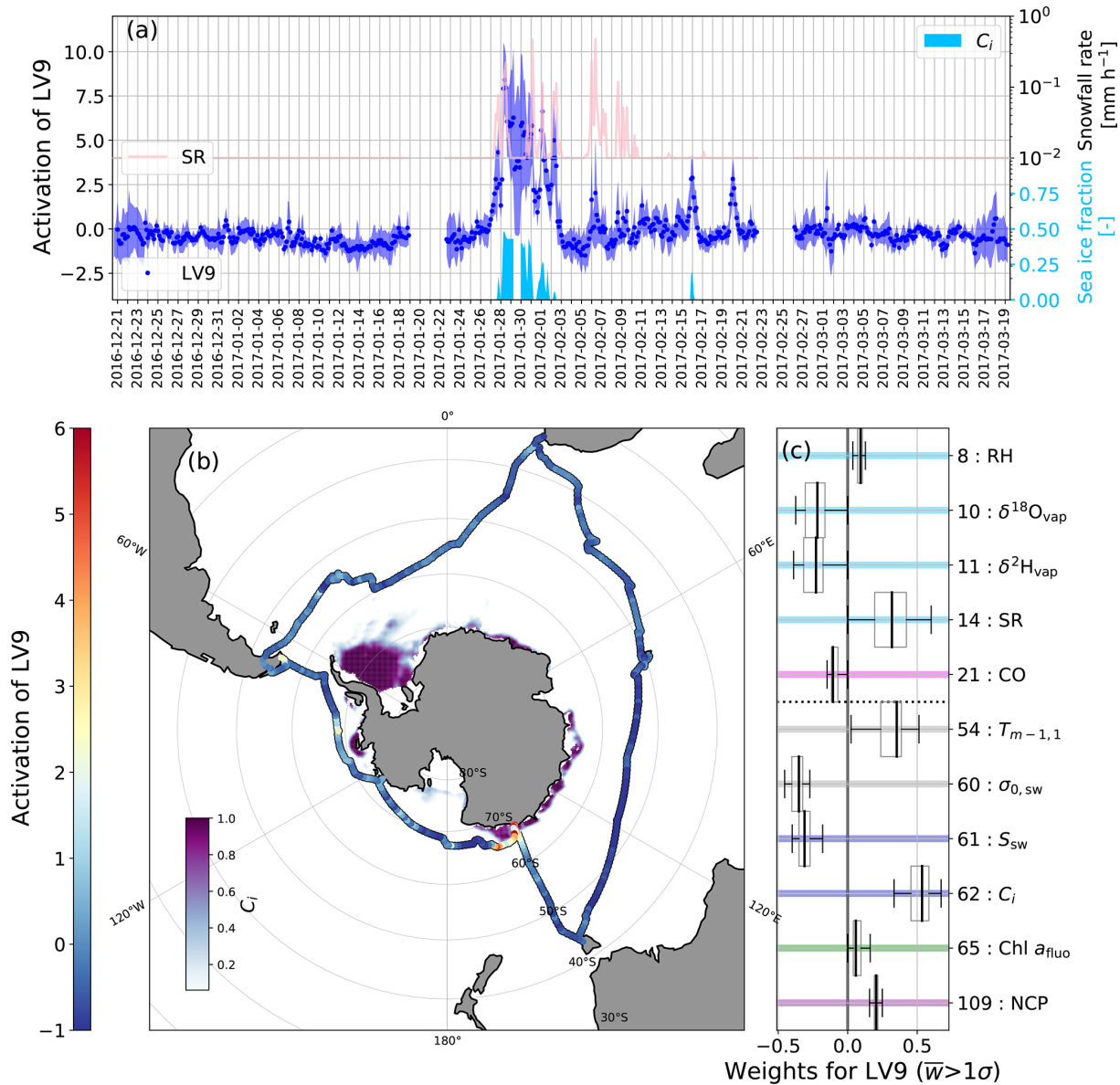


Figure 4. (a) Time series of the activation of LV9 “marginal sea ice zone and snowfall” (left axis), sea ice fraction (lower right axis), snowfall rate (upper right axis). (b) The ship track coloured by the activation of LV9 and the sea ice cover during ACE (Peng et al., 2013). (c) Box and whisker plots of the activated weights.

ures S1 to S4 in the Supplement show this representation for every LV. Non-zero median values represent variables, which are active for a specific LV for more than half of the bootstraps. We measured the significance of the weights by the ratio of their magnitude to their variability. In order to obtain robust measures, we used the median of the weights \tilde{w} and the median absolute deviation (MAD) over the bootstrap runs, with $\sigma = 1 \text{ SD} = 1.4826 \text{ MAD}$ for normally distributed data. Significance of the weight assignments is measured in terms of the ratio $\frac{\tilde{w}}{\sigma w}$. Note that the absolute sign of the weight is arbitrary: for the sPCA, opposite sign assignments lead to the same amount of variance. Within each LV,

a positive sign denotes positive correlation of the OV with the LV time series, and a negative sign denotes anticorrelation.

We quantified the dependency of OVs to each LV by computing their covariance. We scaled this value by the corresponding OV–LV entry in the weight matrix to make the covariance comparable across all OVs.

$$\text{cov}_{\text{scaled}}(X_i, U_j) = \frac{(X_i^T U_j) \cdot V_{ij}}{N_i} \quad (4)$$

As described in Sect. 3.5, we find that the capability of the sPCA reconstruction to explain the variability of the OVs

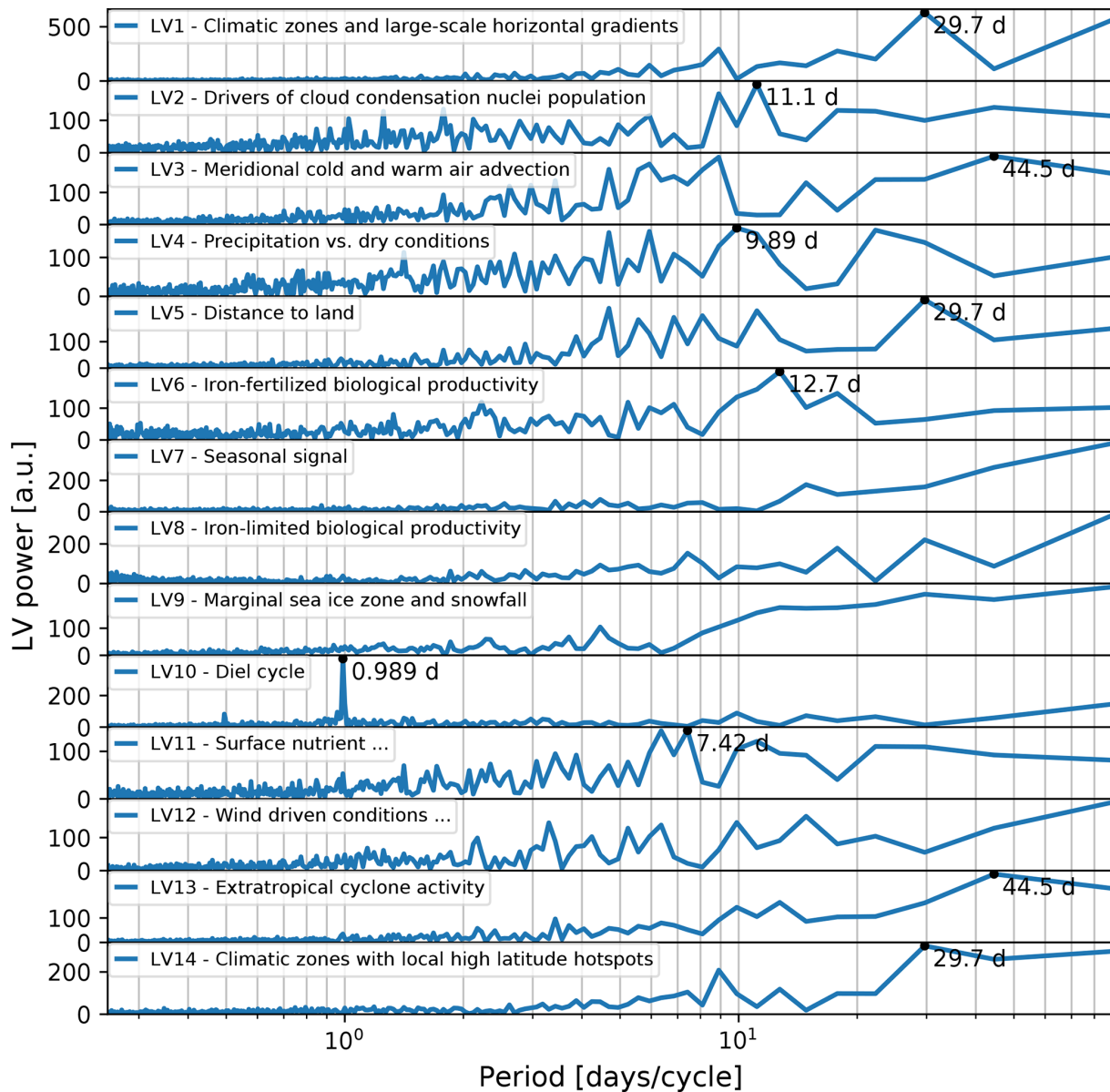


Figure 5. Periodograms of the LV activation time series. The black marker indicates the peak period in days (only shown if smaller than $\frac{1}{2}$ of the sample period).

(given by the sum of the scaled covariances) is very low for time series with a large fraction of missing observations.

5 Discussion

Sparse PCA is a powerful method to detect various features in a multi-variable and heterogeneous dataset. The key strengths of the method are as follows: first, sparse PCA has an untargeted exploratory character, i.e. the possibility of relating many different OV_s with each other and identifying correlations, which one might not intuitively address in a targeted analysis. Second, because sPCA can easily relate geo-

graphical information with all OV_s, it is possible to explore spatial patterns and obtain a geographic overview. This also allows us to identify geographical hotspots, as discussed in Sect. 5.1. Third, sPCA can help to identify original variables that are key to many processes, as discussed in Sect. 5.3. Due to the possibility of exploring a large number of OV_s at the same time, it becomes straightforward to isolate those OV_s that stand out. Fourth, we can explore which processes (LV_s) contribute to explaining the variability of the OV_s, as is shown in Fig. 6. The three main drawbacks of the method are (a) the absence of an underlying temporal model, which favours direct correlations in time and space, (b) the linearity

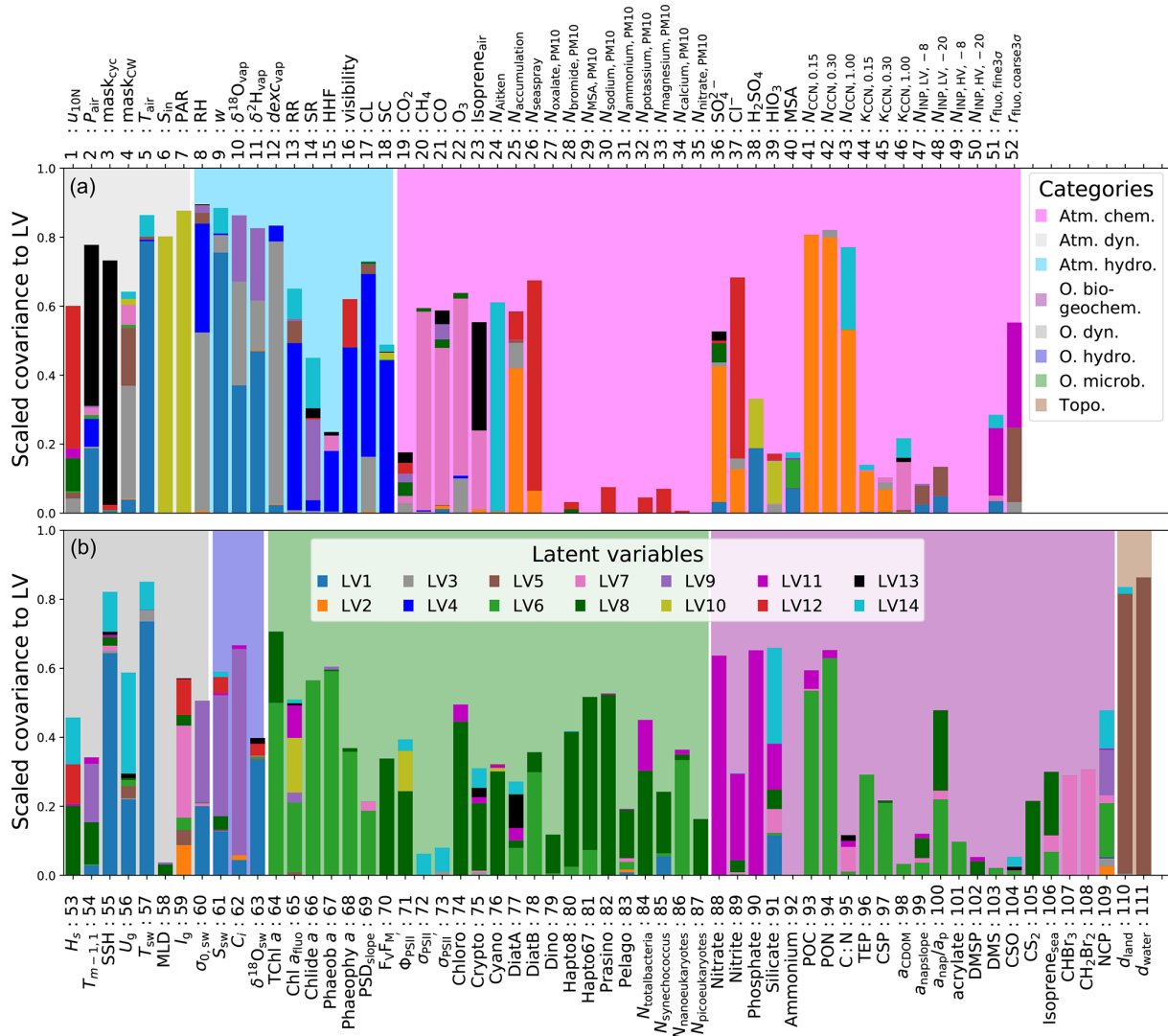


Figure 6. Covariance between the LVs and OVs scaled by the sPCA weights (see Eq. 4) as stacked bar plots, with the colour denoting the LV (see legend in panel b). OV categories (see Sect. 2.2) are indicated by the background shading (see legend in panel a).

assumption, which cannot reveal non-linear processes, and (c) OVs represented by sparse data that might not feature in LVs, which does not imply that they are not part of a process.

It is important to note that our study is constrained to the spatio-temporal scales of the ACE cruise (single season), the sampling intervals along the cruise track (varies among variables), and the chosen 3 h resolution for the sPCA analysis. This limitation has the important implication that we cannot identify variations and processes on longer scales, such as interannual variations, or shorter scales, i.e. the mesoscale or sub-mesoscale. For example, mesoscale eddies, which are an important driver of Southern Ocean variability, are not resolved by our analysis because the 3 h interval (about 57 km if the ship moved at 10 knots) is larger than the Rossby radius of deformation at these latitudes (Chelton et al., 1998).

Even though the ACE cruise covered a relatively long time period from late December to late March, the robustness of the derived seasonal signals from this dataset is limited. This limitation arises from the ship’s movement, thereby covering a wide range of environmental conditions. Thus, signals on timescales such as the seasonal signal depicted by LV7 need to be interpreted as integrated signals occurring on sufficiently large scales. For example, the seasonal variation of the intensity of solar radiation in LV7 shows a decrease anywhere across the Southern Ocean towards austral fall. We can also attribute a seasonal signal to phenomena that only occur during a certain period and certain location. For example, the melting of sea ice discussed in LV9 only occurred in a limited region at the time of the cruise, but it would have been a much more widespread signal if the cruise had taken place in austral spring when the sea ice cover was more extensive.

Therefore, it is important to note that we cannot discuss the full seasonal evolution of the signal because we only spent a few days in the sea ice region, but the input of freshwater from the melting sea ice emerges as an important seasonal phenomenon in our analysis.

In the following subsections, we highlight features identified by the sPCA, which occur across several LVs and OV: (5.1) particular geographical locations (hotspots) where many LVs responded, (5.2) LVs that give insight into atmosphere–ocean interactions, and (5.3) OVs that contribute to variability on many spatial and temporal timescales i.e. they appear in many LVs.

5.1 Hotspots of latent variable activation

The dimensionality reduction achieved by the sPCA allows for visual inspection of the joint variability of variable groups that are provided in the LV time series. Periods where several of these groups show large coinciding variability are of particular interest as they may indicate local hotspots of biological activity or events that fall outside the “normal” variability. In Fig. 7, hotspots are indicated along the cruise track during which a minimum of four LVs strongly responded. We grouped hotspots into three types.

Aerosols and precipitation. The first hotspot (P1), which we call “strong precipitation event”, coincides with the visit to the Prince Edward Islands (26 to 28 December 2016). Heavy and prolonged rainfalls (LV4) coincide with a reduction of Aitken (LV14), accumulation (LV2), and coarse mode aerosol concentrations (LV12). The observed decrease in aerosol concentrations lags up to 12 h behind the observed precipitation rates. This time lag is likely due to the fact that most particles are not removed through interception with falling rain but rather through activation in the cloud layer (Seinfeld and Pandis, 2016), and vertical mixing is required before the depleted air can be observed near the ground. Therefore, a time lag on the order of a few hours is conceivable (Lewis and Schwartz, 2004). However, due to the heterogeneity of the precipitation patterns, the depletion in the aerosol concentrations may have originated from rainfall events other than the ones observed. A similar but much shorter hotspot (P2) with activations of the same LVs occurred near the Kerguelen Islands (3 to 4 January 2017). Nine further strong rain and snowfall events (P3 to P8 and S1 to S5 in Fig. 7b) with precipitation rates $> 0.1 \text{ mm h}^{-1}$ are less clearly reflected in the three aerosol-related LVs. There are also three occurrences where LV4 shows strong negative activation (driven by low visibility) and LV12 and LV2 strong negative activations (few particles) during rather weak precipitation events (X1 to X3 in Fig. 7b). In general, the time series of LV2 and LV12 show stronger resemblance in periods with low aerosol concentrations than for high concentrations. We interpret this as a relatively strong similarity in the sink processes of accumulation and coarse mode aerosols rather than in their sources.

Advection of Antarctic air. Hotspot A1 (Fig. 7c) was observed near Mertz Glacier, where the ship stayed from 27 January until 2 February 2017 (see Sect. A3.2). The advection of cold Antarctic air masses (12:00 UTC on 28 January until 12:00 UTC on 30 January 2017) led to a sudden drop of the air temperature to the lowest value encountered during ACE (-10°C). This drop in temperature is reflected in the lowest values of LV1 indicating the greatest polar influence observed and in LV3 indicating the strongest air–sea temperature gradient during the cruise. At the same time, conditions were dry, as indicated by the negative activation of LV4. During the event, a large increase in the Aitken mode particle number concentration (N_{Aitken}) over the otherwise low concentrations in the Pacific sector was observed (see Fig. A2). This increase was caused by the strongest new particle formation event measured during the entire expedition (Baccarini et al., 2021). In fact, this event constitutes the most pronounced difference in the time series of LV1 (climatic zones and large-scale horizontal gradients) and LV14 (hotspot-driven climatic zones).

Hotspots of ocean productivity. There are a number of well-known ocean productivity hotspots in the Southern Ocean near Subantarctic islands and the Antarctic continent. Two hotspot locations were observed in LV6 and LV14 at Siple Island (B1) and near the Mertz Glacier (B2 in Fig. 7d). These hotspots are fuelled by local iron enrichment due to the effects of topography and sea ice melt as described in Sects. A6.2 and A3.2. The result is increased biological productivity, more microbial biomass, and other secondary products such as gel-like organics, protein-rich particles, and trace gases. Note that we also find LV6 and LV14 responses around Kerguelen (LV6), South Georgia (LV6, LV14), South Sandwich Islands (LV6), and Bouvet (LV6, LV14), but the responses were driven by OVs other than those indicating increased productivity.

5.2 Atmosphere–ocean interactions

Figure 8 shows the activation of categories in each LV. For example LV4 contains only OVs from the two categories “Atmospheric dynamics and thermodynamics” and “Atmospheric side of the hydrological cycle” (Fig. 8), while LV1 contains OVs from all categories except “Topography” (Fig. 8). The categories contain different numbers of OVs. In order to make activations comparable they are shown as ratios of the activated OVs per category over the total number of OVs per category.

In most LVs, we find a coinciding activation of variables in the “Atmospheric dynamics and thermodynamics” and in the “Oceanic dynamics and thermodynamics” categories, which are related to local coupling of wind and waves, larger-scale variations of air and water temperature, and characteristics of the ocean currents. Such a relation between the atmosphere and ocean is, however, missing for precipitation (LV4; Fig. 8) and incoming solar radiation (LV10; Fig. 8). These LVs only

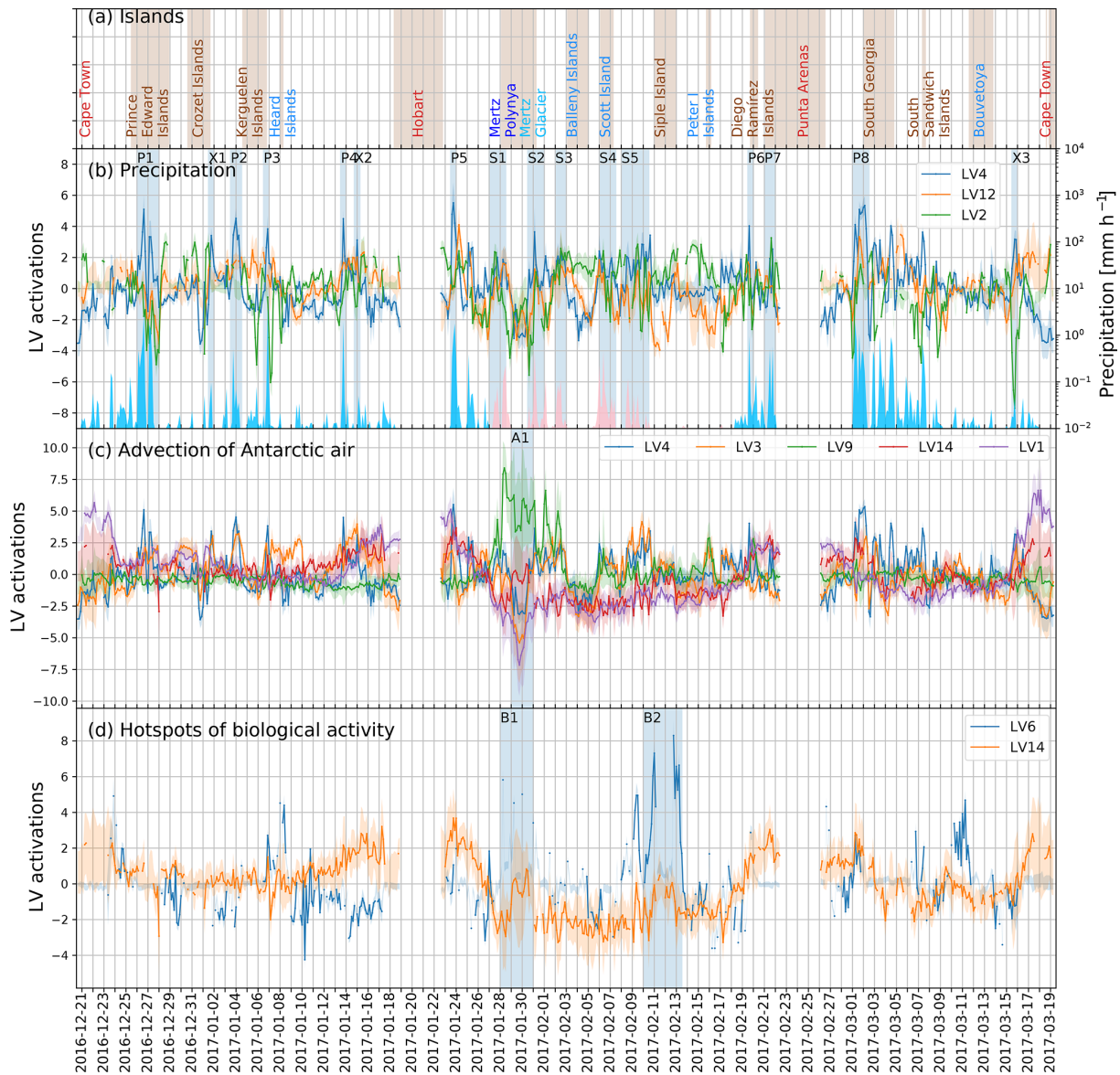


Figure 7. (a) Indicators for the islands. (b) Time series of LV4, LV12, and LV2 with precipitation hotspots (rainfall P1 to P8, snowfall S1 to S5) and situations of reduced visibility (X1 to X3). (c) Time series of LV4, LV3, and LV9 with the advection of Antarctic air (A1). (d) LV6 and LV14 with two biological hotspots (B1 and B2).

activate OVs from the “Atmospheric dynamics and thermodynamics” category but not from the “Oceanic dynamics and thermodynamics”. One possible explanation for the absence of a clear influence on the ocean is that the precipitation (LV4) and the diurnal cycle (LV10) represent strong variation of atmospheric OVs on timescales of less than a day, which might be too short to trigger considerable oceanic variability of detectable strength.

For the “Oceanic” and “Atmospheric hydrological cycles” categories we find a similar pattern. Links between ocean and atmosphere are visible for LVs with a strong low-frequency (> 1 month) component like the climatic zones (LV1; Fig. 8),

the seasonal signal (LV7; Fig. 8), and intermediate frequencies (in the order of days) such as sea ice cover (LV9; Fig. 8), and cyclone activity (LV13; Fig. 8). LVs that happen on short timescales, for example strong precipitation-related variations of LV4, trigger only a weak ($\bar{w} < 1\sigma$) marine reaction, e.g. in the local surface water salinity (see Fig. A4), which predominantly varies over larger spatio-temporal scales due to mixing processes, the cumulative effects of rainfall and evaporation (Dong et al., 2009; Ren et al., 2011), sea ice formation and melting (Haumann et al., 2016), and glacial meltwater (Jacobs, 2002).

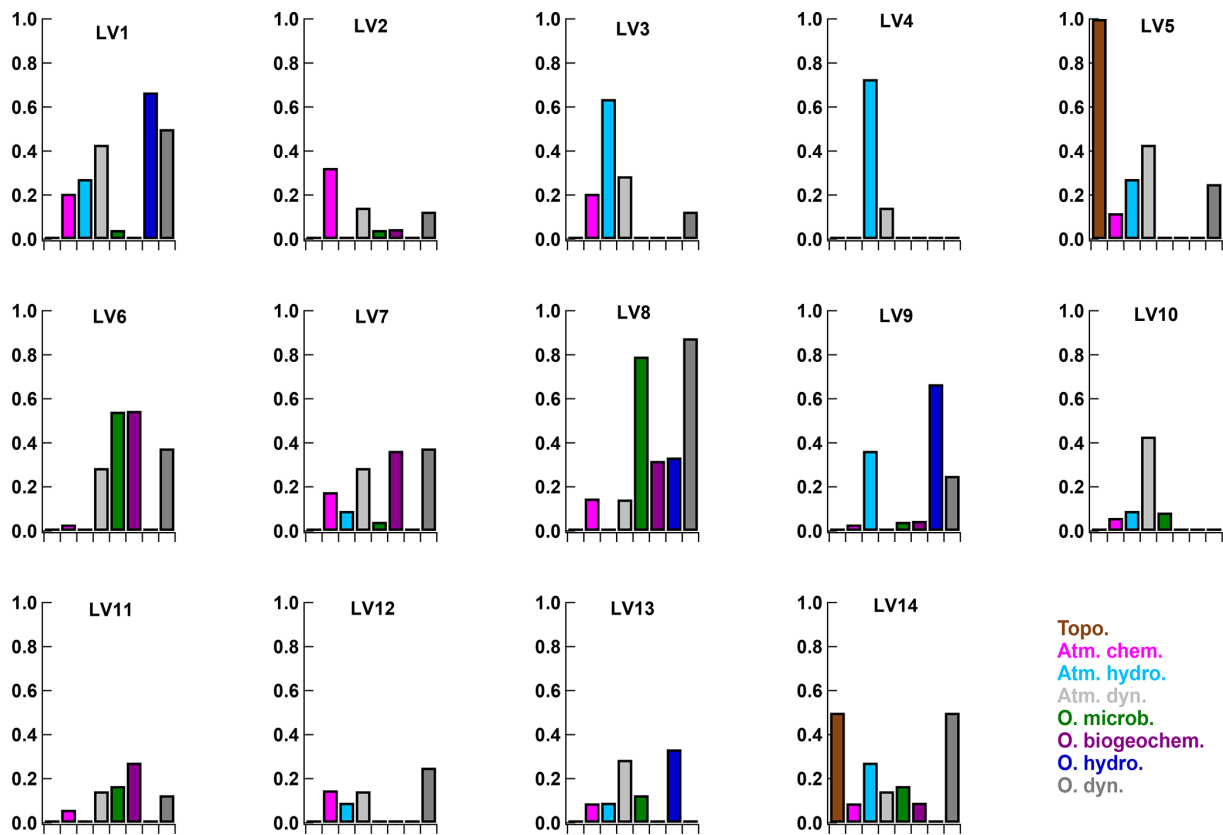


Figure 8. Bar charts showing the activation of OV categories in each LV. The bar colour denotes the categories as given in the legend and in Table 1. The bar length denotes the number of active OVs ($\bar{w} > 1\sigma$) per category divided by the total number of OVs per category.

Coupling of OVs from the “Oceanic biogeochemistry” and “Oceanic microbial community” categories with OVs from the “Atmospheric chemistry” category is rare. The relationship between dimethyl sulfide (DMS)-emitting microbial communities, trace gases, and aerosol chemical composition is long known. However, a direct correlation, as would be discovered by the sPCA, cannot be expected, due to the timescales involved. Atmospheric DMS oxidation in the Southern Ocean is estimated to take 2–5 d (Chen et al., 2018) and during this time the air mass will move away from the microbial activity area. Hence, a direct correlation is not observed. A hint of the connection between microbial activity and atmospheric DMS concentrations is given by the higher MSA concentrations at higher latitudes (see LV1 Sect. A1.1) and by the positive weight of MSA in particulate matter smaller than $10\mu\text{m}$ in LV6, which describes the occurrence of iron-fertilised plankton blooms (see Sect. A6.2).

The above observations show that our analysis targets processes that manifest themselves in rather local correlations, such as the established link between wind speed and sea state or correlations based on smooth variations over time and space, such as the large-scale horizontal gradients in the air and sea water temperature and the hydrological cycle. To better understand the ability of the sPCA to capture non-

local processes occurring with a time lag or those affected by transport across larger scales, we analysed air mass back trajectories. This analysis provides a valuable extension to infer potential relations of the observed signals with up-wind conditions and air mass history. Two examples are the advection of cold or warm air (see LV3 – “Meridional cold- and warm-air advection”, Appendix A), and the removal of accumulation mode aerosols during successive precipitation events (see LV2 – “Drivers of the cloud condensation nuclei population”, Appendix A). To include processes occurring with a time lag or those affected by transport across larger scales, the coupling with air mass back-trajectory analysis provides a valuable extension to infer potential relations of the observed signals with upwind conditions and air mass history, for example the advection of cold or warm air (see Sect. A2.1) or the removal of accumulation mode aerosols during successive precipitation events (see Sect. A4.1).

Note that these findings would not change fundamentally if we were to choose a coarser categorisation of the OVs by merging the “Atmospheric/ocean dynamics and thermodynamics” and “Oceanic/atmospheric hydrological cycles” categories.

Table 3. OVs which occur in four or more LVs with $(\bar{w} > 2\sigma)$.

Symbol	Variable	ID	List of LVs with $\bar{w} > 2\sigma$	No. LVs
mask _{CW}	cold- and warm-air mass advection	OV4	LV3, LV5, LV6, LV7, LV10	5
I_g	Median light intensity in mixed layer	OV59	LV5, LV2, LV6, LV7	5
u_{10N}	10 m neutral wind speed	OV1	LV3, LV5, LV8, LV12	4
RH	Relative humidity	OV8	LV3, LV4, LV5, LV9	4
P_{air}	Atmospheric surface pressure	OV2	LV1, LV4, LV7, LV13	4
U_g	Surface ocean geostrophic velocity	OV56	LV1, LV5, LV6, LV14	4
SSH	Sea surface height	OV55	LV1, LV7, LV8, LV14	4

5.3 Key original variables

Figure 6 shows the scaled covariances ($\text{cov}_{\text{scaled}}$; Eq. 4) between the OVs and LVs as stacked bar plot for each of the OVs. The $\text{cov}_{\text{scaled}}$ provides a measure of the contributions of the LVs to the reconstruction of an individual OV. We observe that most OVs are related to more than one LV. The inclusion of an OV in multiple LVs can occur for several reasons: (i) the OV may be important for or affected by a number of processes and can thus be seen as key variable in the dataset, (ii) derived variables are more likely to occur in several LVs as they are strongly correlated to the multiple observed variables from which they were constructed, or (iii) coincident correlations, which, while they cannot be ruled out completely, are not very likely due to the 3-month-long observation periods. Table 3 shows OVs that occur in four or more LVs with weights that satisfy $\bar{w} > 2\sigma$, i.e. where the model assigns a high level of significance to the correlation between OV and LV. Here, we discuss these top seven OVs.

The ranking is led by the cold and warm temperature advection mask (mask_{CW}), which features in 5 of the 14 LVs. The frequent occurrence of mask_{CW} in the LVs highlights the importance of the air–sea temperature difference, which describes the thermal disequilibrium between the ocean and the atmosphere. The mask_{CW} correlates strongest ($\text{cov}_{\text{scaled}} = 0.33$) with LV3, which relates to the meridional advection of cold or warm-air masses (see Sect. A2.1), and secondly ($\text{cov}_{\text{scaled}} = 0.17$) with LV5, which relates to the ship’s location relative to the nearest land (see Sect. A3.1). The sPCA results also isolate a weak seasonal trend (LV7) ($\text{cov}_{\text{scaled}} = 0.06$) and diel variations ($\text{cov}_{\text{scaled}} = 0.02$) of mask_{CW} (LV10).

Like mask_{CW}, the derived variable, median light intensity within the ocean mixed layer (I_g) shows ($> 2\sigma$) contributions to five LVs, which is due to the inclusion of other OVs in the calculation of I_g (see Supplement Sect. S1.9 for the calculation). For example, the strong link with the seasonal signal (LV7) reflects the decreasing solar radiation intensity and period over the progression of ACE. The anticorrelation of I_g with the wind-driven conditions (LV12) likely results from the deepening of the oceanic mixed layer in stormy conditions. In addition, the decrease of I_g closer to land (LV5) is

likely caused by the increased light attenuation of the higher particulate matter concentrations in the surface ocean.

Surface wind speed (u_{10N}) is strongly linked to four LVs. In LV12, it drives the sea spray aerosol concentration (N_{seaspray}). LV8 (iron-limited biological productivity) reveals a positive correlation of wind speed, significant wave height (H_s), and period ($T_{m-1,1}$) with biological productivity indicators because the microbial community profits from an increased nutrient supply due to the stronger vertical mixing in rougher sea conditions (Carranza and Gille, 2015). The sPCA resolves the higher probability of high wind speeds during cold-air advection compared to warm-air advection (see LV3). As discussed in Sect. A3.1, the weak anticorrelation of wind speed and the distance to land (d_{land}) may be either due to orographic enhancement of wind near land or the coincidence of some island visits with the passage of storms.

Due to their meridional pattern, the satellite-derived sea surface height (SSH) and surface ocean geostrophic velocity (U_g) both occur in LV1 and LV14, which relate to the climatic zones and large-scale horizontal gradients. U_g is also affected by the sea bed topography (LV5), while a seasonal change in SSH is related to the change in water temperature (LV7). In addition, the two OVs are linked to microbial activity. U_g shows relations to the observed patterns in iron-fertilised productivity as represented by LV6, with high productivity occurring close to land masses where currents are weaker and productivity is stimulated by the island mass effect (Doty and Oguri, 1956; Blain et al., 2007). The activation of SSH in LV8 shows that distinctive changes to the ocean dynamics and thermodynamics in open waters during ACE, represented by SSH and other OVs in that category, appear to be important for facilitating the re-supply of much-needed dissolved iron to the iron-starved surface microbial community.

The appearance of atmospheric pressure (P_{air}) in several LVs (LV1, LV4, LV7, and LV13) reflects the importance of atmospheric pressure and especially atmospheric pressure gradients in shaping variations in large-scale atmospheric dynamics. The overall meridional pressure gradient (LV1) is modulated by synoptic-scale variability due to the life cycle of cyclones and anticyclones over the Southern Ocean. Measurements of atmospheric pressure are thus indicative of cy-

clone activity (LV13) and the passage of the cyclones' cold and warm front and related precipitation events (LV4). Seasonal variations in surface pressure are further described by LV7.

In summary, we find that state variables of the environment such as the air–sea temperature difference, wind speed, sea surface height, surface ocean geostrophic velocity, atmospheric pressure, and median light intensity in the ocean mixed layer are critical for the identification of Southern Ocean processes and they relate to chemical and biological processes in the atmosphere and ocean. We suggest that these variables should be given high importance in the planning and execution of future large-scale research campaigns, in long-term observational networks, and satellite-based monitoring, such that numerical models can be assessed in their capability of accurately describing these key variables.

6 Conclusions

We applied the unsupervised machine learning method sparse principal component analysis to a heterogeneous dataset of 111 original variables (OVs) from the Southern Ocean, which were measured during the 3-month long Antarctic Circumnavigation Expedition. These variables describe the physical, chemical, and biological state of the surface ocean and the lower atmosphere during the 2016/2017 austral summer season. Scientific interpretations are given for the 14 latent variables resulting from the sPCA. Together they explain 55 % of the total variance of the 111 OVs.

The resulting 14 latent variables offer a new statistical perspective on relationships between physical, chemical, and biological processes, as well as air–sea interactions over the Southern Ocean, in line with existing knowledge. Our results describe processes in the following domains: large-scale circulation (LV1, LV14), atmospheric and oceanic advection (LV3, LV4, LV13), geographical effects (LV5, LV9), atmospheric chemical processes (LV12, LV2), marine microbial dynamics (LV6, LV8, LV11), and solar forcing (LV7, LV10). We classified the OVs into eight categories comprising “Oceanic and atmospheric dynamics and thermodynamics”, the “Oceanic and atmospheric side of the hydrological cycle”, “Atmospheric chemistry”, “Ocean biogeochemistry”, “Oceanic microbial community”, and “Topography”. Most of the LVs include oceanic and atmospheric OVs from multiple categories, which supports the notion of the Southern Ocean as a heavily interconnected system.

Our large survey of the Southern Ocean and sPCA analysis reaffirmed the important role of the oceanic circulations and frontal zones in shaping the nutrient availability, which controls biological community composition and productivity (LV6, LV8, LV11, LV14). We identified a strong regional impact of sea ice on sea water salinity, on the dampening of surface waves, and on increased phytoplankton growth and net community productivity (LV9). This strong control of the sea

ice on the ocean points towards important impacts that possible future sea ice changes in the region could have on the physical and ecological system. Various atmospheric chemical regimes were identified. For example, LV12 establishes the link between large sea spray particle concentrations and heavy sea state and hence the region of the westerly wind belt. LV2 describes the dominant and ubiquitous role of accumulation mode aerosols for cloud seeding, while LV14 illustrates the negative latitudinal gradient of the Aitken mode particles with modulations by local hotspot sites near coastal Antarctica and certain islands.

A number of further hotspots were identified across several LVs. These represent specific features such as strong precipitation, cold-air mass outbreaks, and the presence of sea ice and islands, all with implications for atmospheric and marine processes. While it is beyond the scope of this work to analyse these events in more detail than provided in the discussion section and Appendix A, it appears that a better understanding of the types, timescales, and implications of processes at the hotspots is needed. The identification of hotspots demonstrates the ability of sPCA to highlight outstanding features across the Southern Ocean.

While most OVs contributed to less than four LVs, seven OVs contributed to four or five LVs and were hence interpreted as key variables. They include the air–sea temperature difference, upper-ocean light intensity, wind speed, relative humidity, atmospheric pressure, oceanic geostrophic velocity, and sea surface height. We suggest that these variables should be given high importance in future research campaigns, long-term observational networks, and satellite-based monitoring, such that they can be used to evaluate numerical models in their capability of accurately describing Southern Ocean processes.

The interpretation of the results requires the combination of expert knowledge on the various original datasets and the components of the environmental system that they describe. At the same time, the sPCA results provide an ideal basis for the interdisciplinary exploration of multivariate datasets, because they can be used to visualise the complex relations between the OVs in an accessible way. The linearity, which may be seen as a strong limitation of the method, is a strength in this context because it warrants full traceability of the decomposition weights and LV activations back to the original variables.

Our extension of the sPCA method to estimate uncertainty with the bootstrap approach reduces the influence of spurious correlations caused by measurement errors or extreme events, which cannot be properly accounted for within the linear framework of the method. The uncertainty estimates proved to be valuable information for the interpretation process, as they allowed the separation of robust and spurious correlations. In combination with the iterative imputation of missing observations, the uncertainty analysis makes the method particularly suited for real-world data with gaps and

outliers. We therefore recommend this method for further application to environmental datasets.

We find that sPCA is capable of resolving many of the complex connections between the OV's and of providing estimates of their relative importance for the observed variability of each OV. On the one hand, the sPCA can be used to find relationships between observed quantities which appear jointly in a latent variable. On the other hand, one can also analyse how important environmental processes, i.e. latent variables, are for the variability of the observed variables, by using the reconstruction of the OV's from the LV's. Examples are the effects of meridional variations (LV1, LV14), enhanced biological production near melting sea ice (LV9), and the island mass effect (LV6) on net community production (see Fig. 6). In combination, these two steps make sPCA a powerful tool for the exploratory analysis of multivariate datasets. At the same time we note that while many relationships can be identified by sPCA, some cannot be resolved because they do not establish themselves as direct correlations between the observed variables due to time lags or insufficient data availability. For example, the contribution of biogenic trace gas emissions to the chemical aerosol composition remains unidentified due to the timescales of the related atmospheric chemical reactions and the coarse time resolution of some of the data.

There is no explicit underlying spatial or temporal model in sPCA, such that the method is capable of resolving multiple important co-existing regimes within the temporal and spatial dimension. For example, within the spatial component there are a number of separate regimes simultaneously influencing microbial dynamics and biogeochemistry, such as large meridional changes in nutrient supply from upwelling vs. local advective and other input processes near land masses or melting sea ice. To date, multivariate models, which can cope with spatial and temporal components at the same time and provide such simple statistical output for interpretation are rare. Therefore, we believe that the approach presented here extends the use of data science in environmental disciplines by providing enhanced interpretation of connected processes (Blair et al., 2019).

Appendix A: Detailed discussion of each LV

The following subsections provide in-depth analyses of the 14 latent variables in the context of the original variables which contribute to them. A contribution is considered if the median value of the contributing weight is larger than its single standard deviation from the bootstrap runs. The LV's are grouped based on the six themes (i) climatological background provided by the large-scale ocean and atmosphere circulation (LV1 and LV14); (ii) atmospheric and oceanic advection, cyclones, and precipitation (LV3, LV4, and LV13); (iii) the effect of islands, continental land, and sea ice (LV5 and LV9); (iv) aerosol concentrations (LV2 and

LV12); (v) ocean microbial dynamics (LV11, LV6, and LV8); and (vi) solar forcing (LV7 and LV10). A further synthesis of the result discussions is provided in Sect. 5.

A1 Climatological background provided by the large-scale ocean and atmospheric circulation

A1.1 LV1 – Climatic zones and large-scale horizontal gradients

Latent variable 1 (LV1) explains most of the variance (9.2 %) in all the 111 analysed original variables (see Table 2 and Fig. A1). It mirrors the climatic background conditions during ACE and ranges from strongly positive LV1 values in the lower latitudes to strongly negative values in the high latitudes. These climatic zones are reflected in the strong horizontal gradients in the air (T_{air}) and surface ocean temperature (T_{sw} ; Fig. A1a) and in the atmospheric water vapour mixing ratio (w). These three variables contribute most to LV1 and are correlated positively with LV1 (Fig. A1c). The most positive LV1 values occurred during the warmest conditions at the beginning and end of the cruise near Cape Town (Fig. A1b). The most negative LV1 values were found during the coldest conditions on 29 January 2017 when the ship was near the Mertz Glacier and under the influence of Antarctic air masses during a cold-air outbreak event (see the LV3 and LV9 discussions below). In contrast with the most positive LV1 values, which are governed by both high atmospheric and ocean temperatures, the most negative LV1 values are largely caused by low atmospheric temperatures alone. This difference can be explained by the absolute lower bound of the ocean temperature being set by the freezing point.

A second major contribution to LV1 is associated with oceanic regions as reflected by the large contributions of sea surface height (SSH), surface ocean potential density anomalies ($\sigma_{0,\text{sw}}$), and surface ocean geostrophic velocity (U_g). This influence of the oceanic conditions can also be depicted by a change of the LV activation when crossing major oceanic fronts (Fig. A1b). Different frontal zones are associated with different ocean biogeochemistry, which is typically associated with nutrient concentrations and their ability to limit primary producers as observed during this expedition (Janssen et al., 2020). However, the observed macronutrients (N, P, and Si) are not activated in LV1, suggesting a more complex situation across the Southern Ocean. Several zonal deviations associated with ocean currents were observed in LV1 as it changed from positive to negative values while the ship was moving from Patagonia to South Georgia on a similar latitude band (Fig. A1b). These decreasing LV1 values across a similar latitude band can be explained by the northward deflection of polar waters with the Antarctic Circumpolar Current (ACC) driven by topography as outlined by the Subantarctic Front, Polar Front, and Southern ACC Front in this region, leading to a strong decline of T_{sw} , SSH, and surface ocean salinity (S_{sw}) and an increase in $\sigma_{0,\text{sw}}$ along

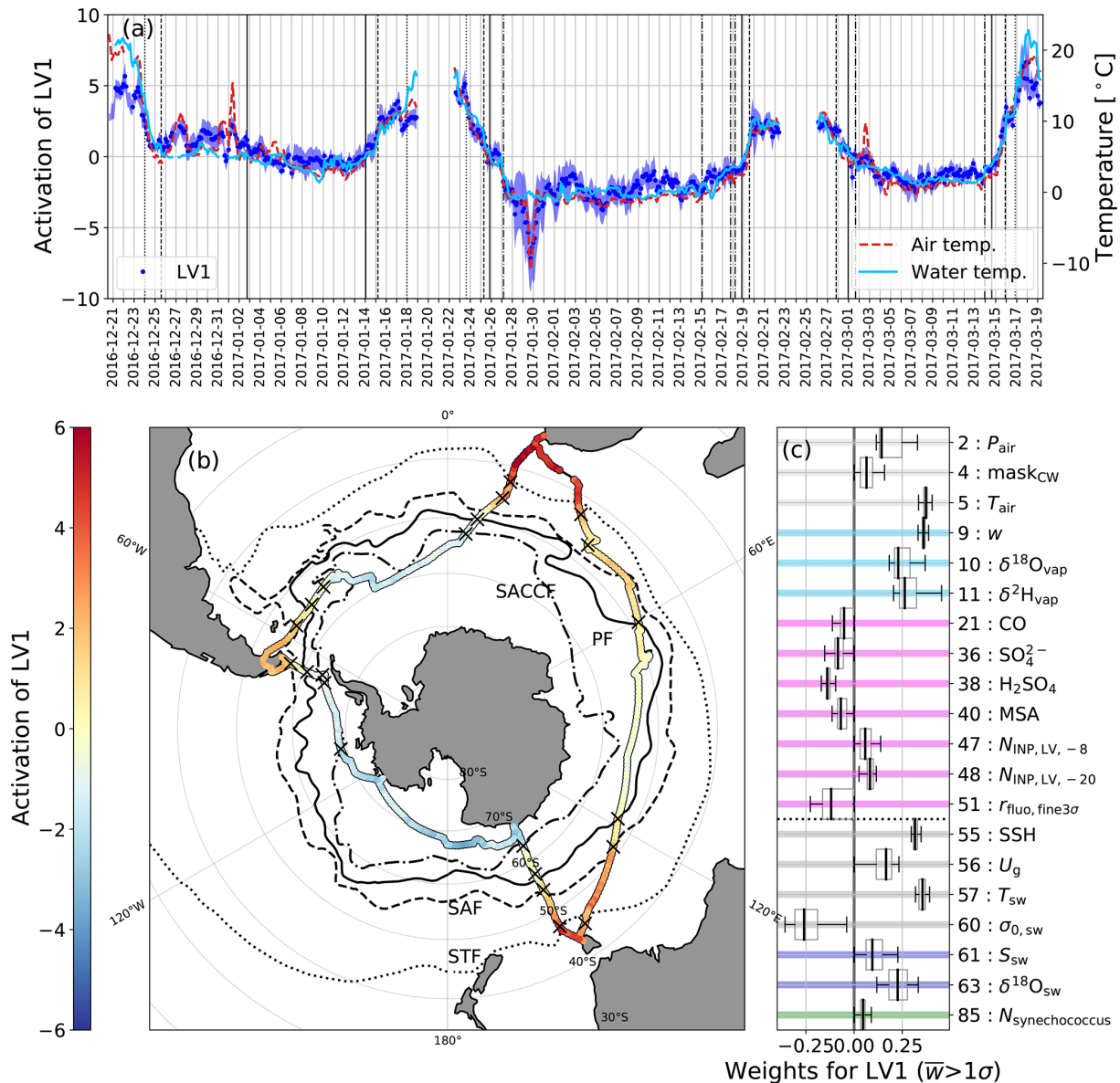


Figure A1. (a) Time series of the activation of LV1 (left axis) and of the air and water temperatures (right axis). Crossings of the oceanic fronts, which were derived from observations during ACE, are indicated by vertical lines (see Supplement Sect. S1 for details), from north to south, as the Subtropical Front (STF; dotted), Subantarctic Front (SAF; dashed), Polar Front (PF; solid), and Southern ACC Front (SACCF; dash-dotted). (b) Map of the ship track coloured by the activation of LV1. Climatological frontal positions (Orsi et al., 1995) are shown as black lines and are denoted as in (a). Crosses indicate the ACE data-derived frontal positions. (c) Box and whisker plots of the activated weights from the bootstrap runs (only weights with $\bar{w} > 1\sigma$ are shown). The colours indicate the OV categories (see Fig. 6).

this cruise transect. This climatological position of ocean currents leads to relatively cool ocean surfaces compared to near-surface air temperature and is likely responsible for the positive weight of the air advection mask (mask_{CW}) in LV1 (see also the discussion of LV3 below). The opposite, i.e. a signature from the warm West Australian and East Australian boundary currents, is visible south of Tasmania and east of South Africa with the overall most positive LV1 activations. Moreover, zonal gradients can also be observed in the south-

ernmost parts (about 65°S to about 74°S) of the cruise in the Pacific sector, where the lowest LV1 values of the entire cruise occur in the south-western Pacific and slightly higher LV1 values occur in the central and eastern parts of the transect (Fig. A1b).

The interpretation that LV1 describes climatological background conditions rather than variations on the timescales of, e.g. weather (LV12 and LV4), season (LV9 and LV7), or the diel cycle (LV10) is supported by its low frequency (Fig. 5)

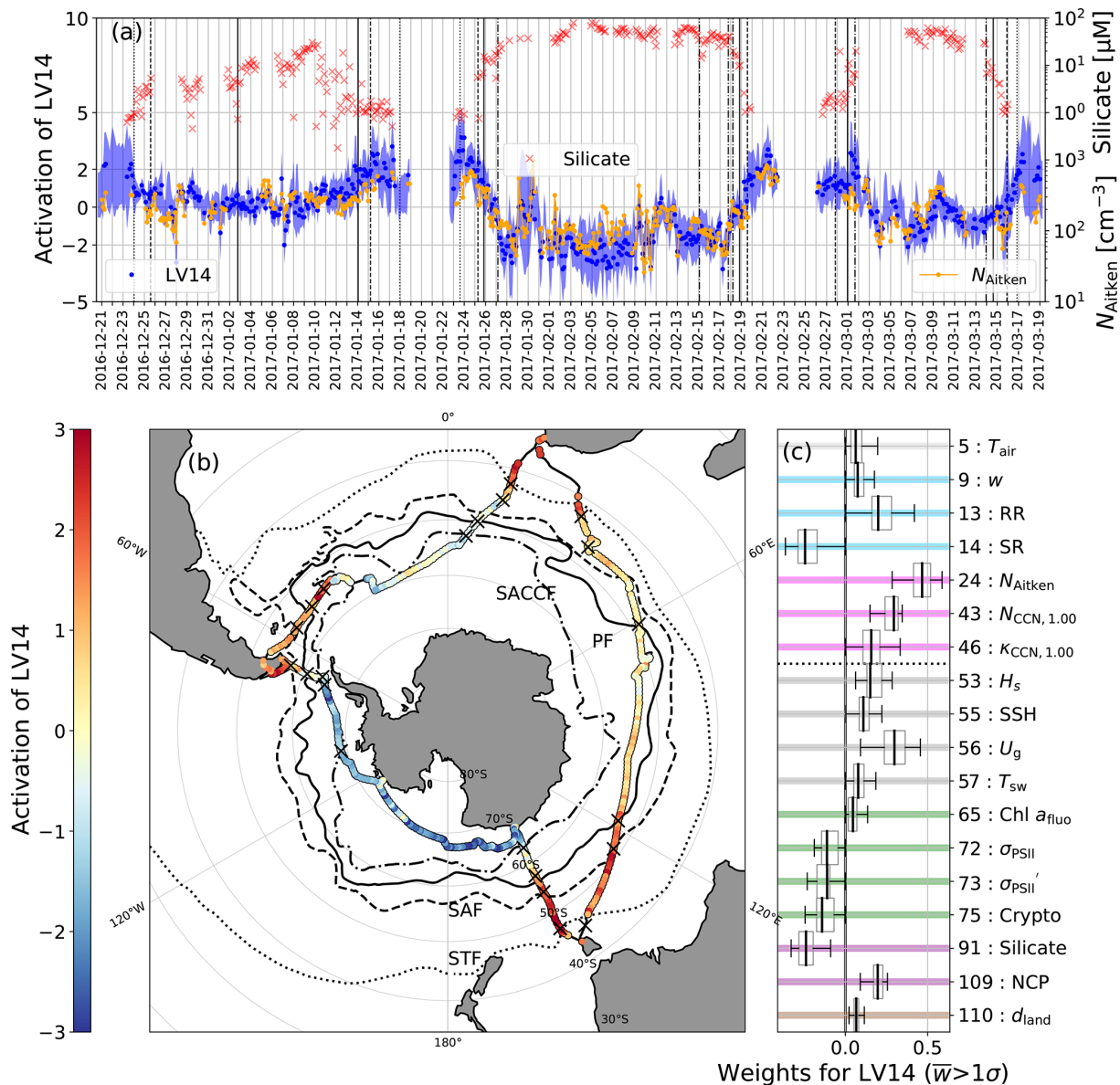


Figure A2. (a) Time series of the activation of LV14 “Climatic zones with local high-latitude hotspots” (left axis), the silicate concentration (top half of the right axis), and the Aitken Mode particle number concentration (bottom half of the right axis). (b) Map of the ship track (circles) coloured by the activation of LV14. (c) Box and whisker plots of the activated weights. See the caption of Fig. A1 for details on the oceanic fronts and frontal crossings.

and numerous OV_s with a known strong climatological influence. LV1 has the highest contribution to the variance in the stable water isotopic composition of water vapour ($\delta^2 H_{\text{vap}}$, $\delta^{18} O_{\text{vap}}$) and seawater ($\delta^{18} O_{\text{sw}}$; Fig. 6). Such a large influence of the climatic zones on the meridional distribution of the atmospheric and oceanic stable isotopic composition during ACE has been noticed and described in detail by Thurnherr et al. (2020) and Haumann et al. (2021), respectively. The overall southward declines in these isotope ratios and S_{sw} are caused by a loss of moisture from the atmosphere to the ocean. LV1 also has the second highest contribution to

the atmospheric pressure (P_{air} in Fig. 6), reflecting the transition from climatologically high-pressure subtropical regions to the circumpolar trough surrounding Antarctica, characterised by high cyclone activity (Papritz et al., 2014).

LV1 additionally includes information about atmospheric chemistry and microphysics. Gas-phase concentrations of sulfuric and methanesulfonic acid (MSA) are higher at higher latitudes. These higher concentrations are consistent with emissions of DMS that result from higher summertime microbial activity (phytoplankton) near the Antarctic coast. DMS is converted into the aforementioned gaseous acids

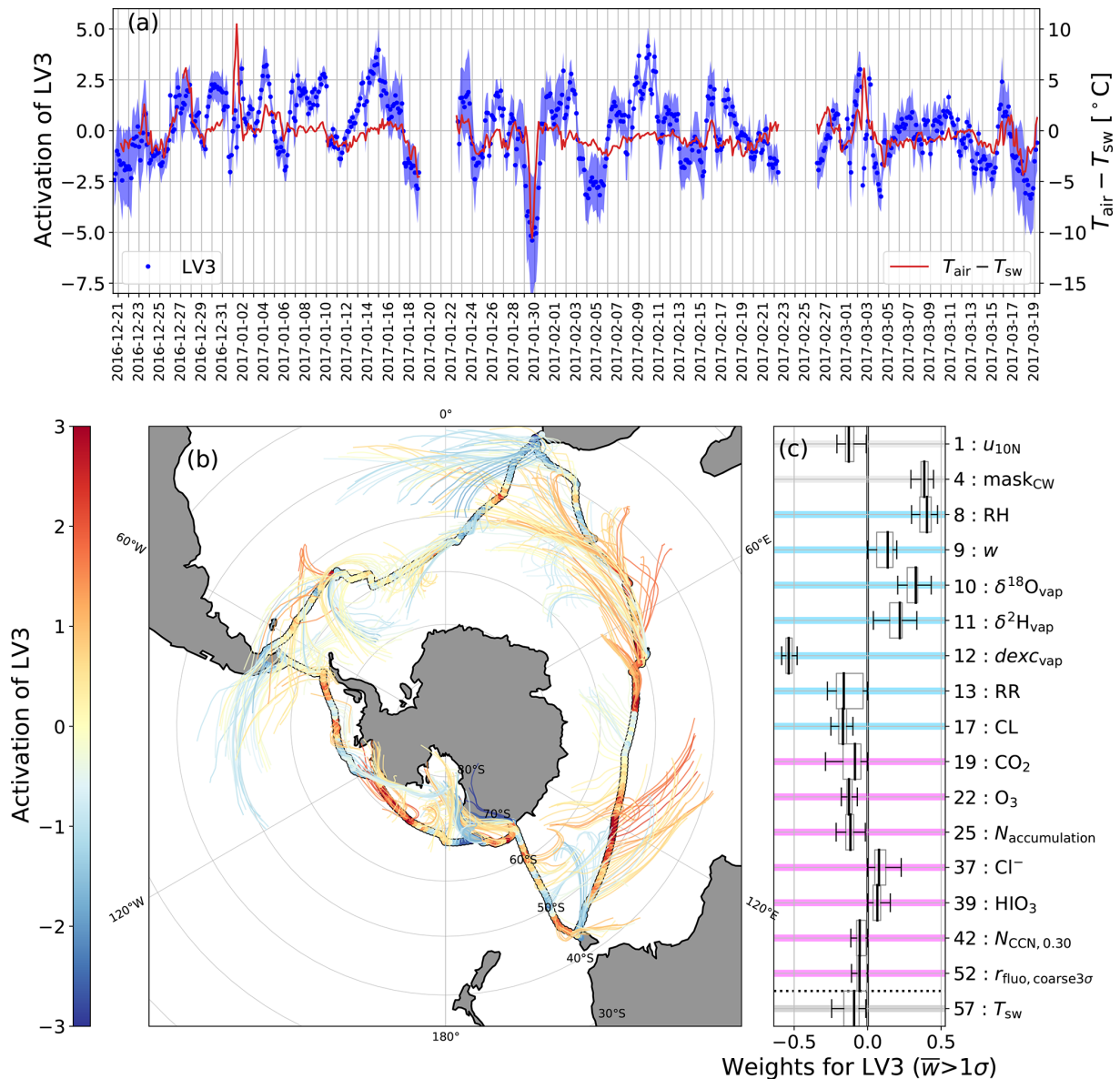


Figure A3. (a) Time series of the activation of LV3 “Meridional cold- and warm-air advection” (left axis) and the difference between the air and seawater temperatures (right axis). (b) Map of the ship track (circles) coloured by the activation of LV3. The median track of the air mass backward trajectories “released” at the measurement location and calculated up to 48 h prior to the release are shown as thin lines coloured by the activation of LV3. (c) Box and whisker plots of the activated weights.

in the atmosphere, which promote new particle formation and aerosol growth (Lana et al., 2011; Chen et al., 2018; Schmale et al., 2019) and are consequently found as sulfate and MSA in the aerosol particles. In general during ACE, ice-nucleating particles (INP) at -20°C ($N_{\text{INP}, -20}$) decreased with increasing latitude. Given that at this temperature, i.e. -20°C , the dominant INP is mineral dust, the observed relationship is plausible. At lower latitudes $N_{\text{INP}, -20}$ increases, where dust emissions from Africa, Australia, and South America potentially contribute (Welti et al., 2020).

In summary, the largest variance in the 111 analysed variables during ACE (9.2%) results from the climatic zones along the cruise track, ranging from warm and humid subtropical conditions in the most northern regions during the cruise (positive LV1 values) to cold and dry polar conditions at southern high latitudes (negative LV1 values). These conditions are reflected in both the surface atmosphere and ocean variables.

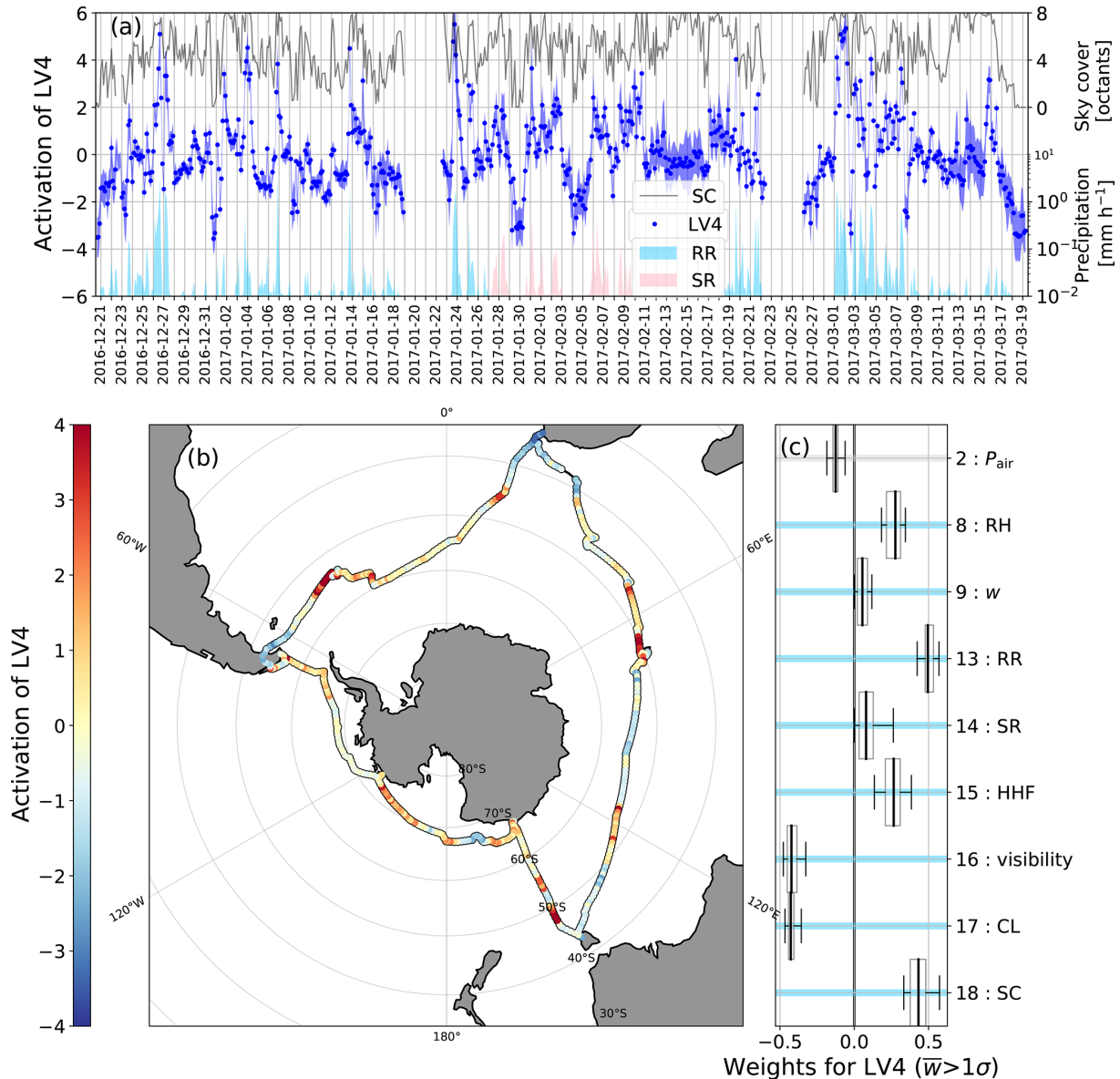


Figure A4. (a) Time series of the activation of LV4 “Precipitation vs. dry conditions” (left axis) of the sky cover in octants (top half of the right axis) and the three-hourly average precipitation rates as shaded areas (rain rate in blue and snowfall rate in pink) (bottom half of the right axis). (b) Map of the ship track (circles) coloured by the activation of LV4. (c) Box and whisker plots of the activated weights.

A1.2 LV14 – Climatic zones with local high-latitude hotspots

The time series of LV14 is largely similar to LV1, with a correlation coefficient of 0.73 and a p value of 0.02 (see Fig. C1 in Appendix C). However, the amplitude of LV14 is smaller and explains only $3.2(\pm 1.4)\%$ of the total variance. The general difference between LV14 and LV1 arises from the opposite sign in LV14 in some high latitude regions, where suddenly some variables go against the large-scale gradient. Examples are near the Mertz Glacier (28 January, 12:00 UTC until 30 January, 00:00 UTC), near Siple Island (11 February,

00:00 UTC until 13 February, 00:00 UTC), on the northern side of South Georgia (1 March, 00:00 UTC until 2 March, 00:00 UTC), and before approaching Bouvetøya (8 March, 00:00 UTC until 11 March, 00:00 UTC), where especially the biological activity tracers chlorophyll a and net community production (Chl a , NCP), as well as the Aitken mode particles, show variations against the large-scale meridional trend. Further, the change in the amplitude of LV14 north of the SAF is weaker compared to the variability south of the SAF when comparing to LV1. Air and water temperature and the water vapour mixing ratio (w) and sea surface height (SSH), which are all dominant in LV1, are also active

in LV14. However, they have much lower importance compared to the weights of other OV's in LV14 such as rain rate (RR) and snowfall rate (SR), which have opposing trends and indicate a transition from rainfall in lower latitudes to preferential snowfall near Antarctica.

The OV with the largest weight in LV14 is the number concentration of particles in the Aitken mode (N_{Aitken}). Particles in the Aitken mode are typically smaller than 80 nm in diameter (the median and interquartile range for the Aitken mode diameter during ACE were 38 and 24–47 nm, respectively Schmale et al., 2019) and are mostly considered to be formed from gas to particle conversion. In the context of the spatial distribution of LV14's activation, the positive weight of N_{Aitken} indicates that they increase with proximity to the non-glaciated continents and decrease close to Antarctica, with the exception of two new particle formation (NPF) events near the Mertz Glacier (29 January, 30–31 January) related to the special environmental conditions encountered there (low temperature, low concentration of larger aerosol, and relatively high solar irradiance). LV14 also explains a considerable fraction of the variance of the number of particles acting as cloud condensation nuclei at a supersaturation of 1 % ($N_{\text{CCN},1.00}$) further north. At such high water vapour saturation the smaller Aitken mode particles become competitive to the larger accumulation mode particles, which generally dominate the cloud condensation nuclei (CCN) population (see Sect. A4.1). In addition, the hygroscopicity parameter of particles acting as CCN at 1 % supersaturation ($\kappa_{\text{CCN},1.00}$) contributes to LV14, underlining the role of such small particles as cloud seeds where LV14 has a strong positive activation.

Several oceanic OV's included in LV14 show clear latitudinal variations. The surface geostrophic current velocity (U_g) was generally high in regions of positive LV14 activation, especially during times spent on the northern flank of the ACC. During these times, we also notice an increased significant wave height (H_s) and expected general northward increases in the sea surface height (SSH) and sea surface temperature (T_{sw}). Surface ocean silicate concentrations (silicate) increase with latitude (Sarmiento et al., 2004; Freeman et al., 2018), as shown by the negative correlation with LV14. Its gradient largely coincides with the latitudinal gradients in the physical quantities and the frontal positions due to its consumption by diatoms that favourably grow in higher latitude waters (Freeman et al., 2018). Diatoms are a large-sized species of phytoplankton that specifically require this macronutrient. The broad latitudinal trends in the distribution of silicate are driven by physical processes, e.g. the lateral supply from the southerly upwelling of the Circumpolar Deep Water source. The phytoplankton communities south of the Polar Front are typically larger in size relative to lower latitudes. This is supported by the positive loading of the cryptophyte (Crypto) variable which is driven by an isolated peak in the biomass of cryptophytes, a larger sized phytoplankton. In addition, σ_{PSII} and σ'_{PSII} , which are the func-

tional absorption (light-harvesting) cross sections of photosystem II of phytoplankton in the day and night, respectively, have positive weights because the absorption cross section co-varies with phytoplankton taxa and size (Moore et al., 2005; Suggest et al., 2009). They generally decrease with increasing cell size, hence underlining that large phytoplankton resides further south. In contrast, net community production (NCP) and fluorescence of in-water chlorophyll *a* ($\text{Chl } a_{\text{fluo}}$) both show a positive weight due to the lower concentrations at higher latitudes.

In summary we interpret LV14 as a second group of OV's whose variability is largely affected by the climatic zones and large-scale latitudinal gradients (as in LV1), but with distinct local signals near the Mertz Glacier and near some of the islands and a more moderate latitudinal change north of the SAF.

A2 Atmospheric and oceanic advection, cyclones, and precipitation

A2.1 LV3 – Meridional cold- and warm-air advection

LV3 represents the effects of atmospheric large-scale to mesoscale and oceanic large-scale advection on the atmospheric composition and stability and explains 4.8(± 0.4)% of the total variance. The highest contributions to LV3 stem from relative humidity (RH) and deuterium excess in water vapour (dex_{vap} ; see Fig. A3), reflecting the effect of the differing strengths of ocean evaporation in different RH environments on the isotopic composition of water vapour in the marine boundary layer. Strong ocean evaporation at low RH leads to high dex_{vap} in the evaporated water vapour due to strong non-equilibrium effects during isotopic fractionation. This anticorrelation of RH and dex_{vap} has been observed and discussed in previous studies (Uemura et al., 2008; Gat, 2008; Pfahl and Sodemann, 2014; Aemisegger and Sjolte, 2018).

The correlation of the cold and warm temperature advection mask (mask_{CW}) with RH shows the importance of the large-scale, meridional horizontal advection in shaping the RH environment (Thurnherr et al., 2021). Due to the increased saturation-specific humidity at high temperature, RH decreases if cold-air masses are advected towards the Equator over a relatively warm ocean surface, and vice versa for warm-air advection over a relatively cold ocean surface. Furthermore, low abundances of heavy water molecules ($\delta^2\text{H}_{\text{vap}}$ and $\delta^{18}\text{O}_{\text{vap}}$) and low water vapour mixing ratios (w), which are normally observed for atmospheric water vapour at high latitudes (see also LV1), are seen with low RH indicating meridional large-scale advection from the south. The different flow patterns of the air masses for cold and warm temperature advection can be seen with 2 d backward trajectories in Fig. A3b, which often show an equatorward flow for cold and a poleward flow for warm temperature advection, respectively.

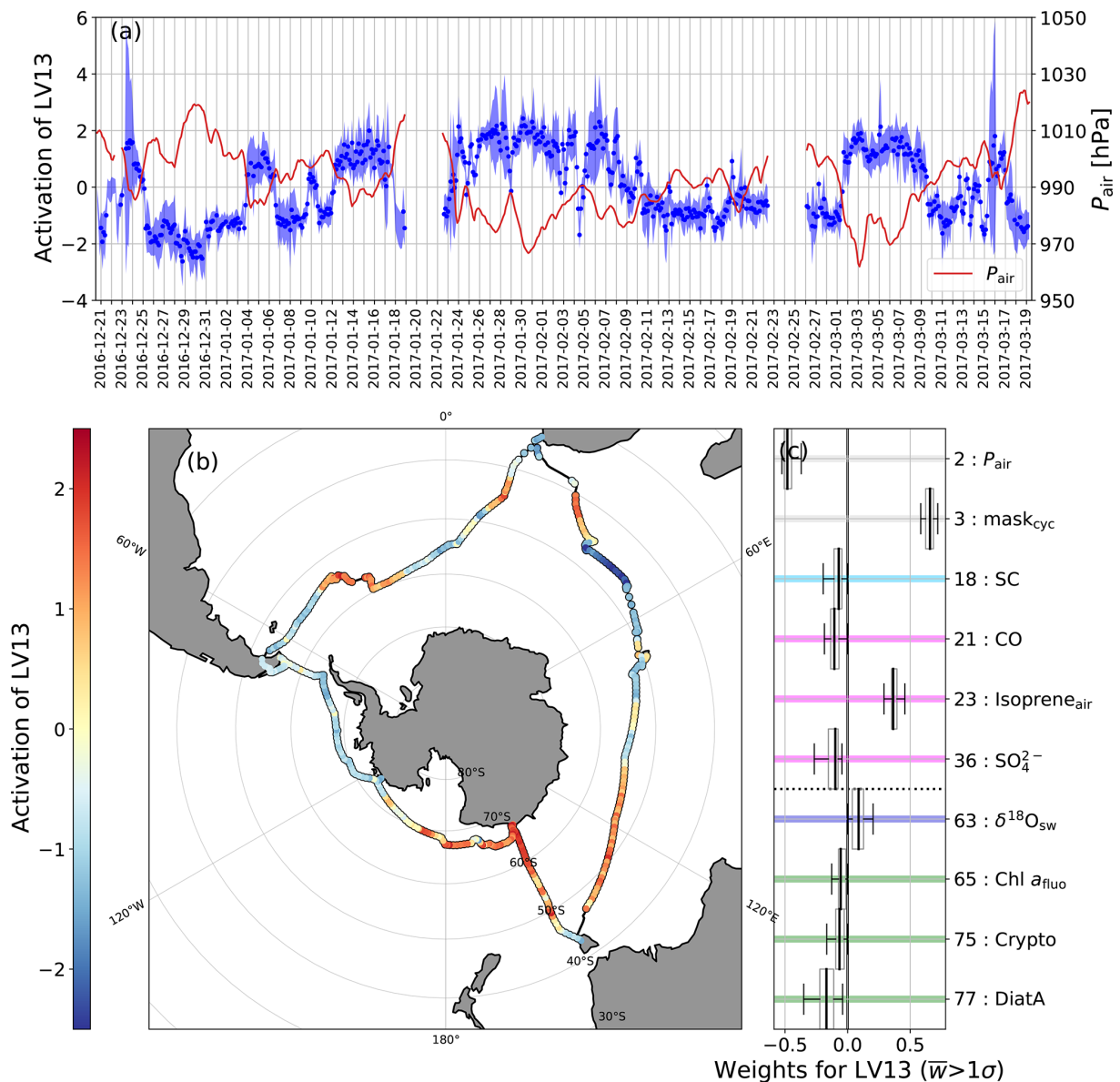


Figure A5. (a) Time series of the activation of LV13 “Extratropical cyclone activity” (left axis) and of the atmospheric pressure (right axis). (b) Map of the ship track (circles) coloured by the activation of LV13. (c) Box and whisker plots of the activated weights.

While the mask_{CW} has a large weight in LV3, the sea water temperature (T_{sw}) contributes only weakly and the air temperature (T_{air}) does not have any median contribution to this LV. This absence of significant contributions by T_{sw} and T_{air} illustrates the importance of the difference between the ocean and atmospheric temperatures rather than their absolute values in shaping the RH environment. Therefore, while LV1 represents the large-scale horizontal gradients in the atmosphere and ocean, LV3 is mostly associated with vertical gradients between the atmosphere and the ocean due to large-scale meridional advection. The negative weights of T_{sw} show that regional T_{sw} anomalies due to oceanic currents can contribute to the air–sea temperature differences. For ex-

ample, in the region of the warm Agulhas current around 30° E, where relatively warm Indian Ocean waters are advected under a relatively cool atmosphere, a negative activation of LV3 is seen (see Fig. A3b).

Next to the dominant OVs, RH, dex_{vap}, and mask_{CW} in LV3, weaker weights are seen for several OVs, which further characterise the different RH environments. We observe a tendency of higher cloud level (CL) and higher atmospheric ozone (O_3) concentrations during dry conditions (low RH). This might indicate enhanced vertical mixing in the marine boundary layer during cold-air advection, which might lead to the entrainment of free tropospheric air masses with higher O_3 concentration into the marine boundary layer

(see Fig. A3c). Such entrainment is particularly likely for the high ozone concentrations observed during a cold-air outbreak from Antarctica, where air masses descended from further aloft. For elevated ozone concentrations between South Georgia and Cape Town, continental pollution outflow from South America cannot be ruled out because CO concentrations are also slightly elevated. An occurrence of higher surface wind speeds (u_{10N}) during the advection of cold air (i.e. negative activation of LV3) can be seen, especially for the Pacific sector where high wind speeds are expected during cold-air outbreaks near the Antarctic continent (see e.g. Kolstad, 2017). High surface wind speed in extratropical cyclones is often associated with the cold front but can occur in both the warm and cold sector of the cyclone and shows a complex mesoscale structure (see e.g. Browning, 2004). It is therefore not straightforward to associate high wind speed with areas of cold- and warm-air advection during the passage of extratropical cyclones, which is also represented by the weaker correspondence of the surface wind speed with LV3 activation for the Indian Ocean and Atlantic sector (not shown). On the synoptic timescale, i.e. 3 to 6 d, which is the dominant frequency of LV3 (Fig. 5), rainfall occurs more often during the advection of cold-air masses. Conversely, comparing specifically strong cold and warm advection, which occurred in regions with an air–sea temperature difference of at least 1.0°C , it has been shown that warm advection is associated with stronger rainfall than cold advection (Thurnherr et al., 2021). Rainfall in the Southern Ocean is mostly related to atmospheric fronts (Catto et al., 2012), which mark the boundaries of cold- and warm-air advection. In this study, cold- and warm-air advection is defined to include these frontal zones between the regions of cold- and warm-air advection. If frontal rainfall more strongly impacts regions of cold advection, it could be the reason for the difference in rainfall occurrence during cold- and warm-air advection to former studies. The contributions of LV3 to the total covariance of rainfall is, however, small compared to LV4 (Fig. 6).

A further contribution to LV3 is given by the accumulation mode aerosol number concentration ($N_{\text{accumulation}}$) with high concentrations during the advection of cold air. Accumulation mode particles are washed out during rainfall and are thus expected to show lower concentrations with increased rainfall, which is in apparent contradiction with the higher rainfall during cold-air advection compared to warm-air advection. The low concentration of $N_{\text{accumulation}}$ during warm-air advection might be explained by precipitation before the air arrives at the measurement location. Backward trajectories show more precipitation occurring for the 5 d prior to arrival for warm-air advection than for cold-air advection (not shown). Therefore, the low concentration of $N_{\text{accumulation}}$ during warm-air advection could be explained by the occurrence of rainfall before arrival at the measurement location. The same logic can be applied to cloud condensation nuclei number concentrations at a supersaturation of 0.3 %

($N_{\text{CCN},0.30}$), which also exhibit a negative loading. Accumulation mode particles constitute the largest fraction of this type of CCN.

In summary, the large-scale advection of air masses or ocean currents leads to near-surface vertical temperature and humidity gradients in the atmosphere. These situations and the induced processes are reflected by LV3 and best represented by the synoptic timescale variability of atmospheric relative humidity and the isotopic composition of the atmospheric water vapour.

A2.2 LV4 – Precipitation vs. dry conditions

LV4 represents the direct effects of single precipitation events, which occur on the timescale of hours (see Fig. A4), on humidity and visibility in the marine boundary layer and explains 4.4 % of the total variance in the data. LV4 shows high contribution from rainfall (RR) and relatively smaller contribution from snowfall (SR). Both RR and SR positively correlate with cloud cover (sky cover; SC), relative humidity (RH), and horizontal hydrometeor flux (HHF) and are anti-correlated with horizontal visibility (visibility), lowest cloud level height (CL) and atmospheric pressure (P_{air}). Thus, LV4 features almost exclusively OV's from the category “Atmospheric hydrological cycle” (with the exception of P_{air}).

Total precipitation is mostly represented by rainfall, with a small contribution of snowfall. Approximately 70 % of all precipitation over the Southern Ocean is related to atmospheric fronts (Catto et al., 2012), and thus LV4 is representative of the timescale of mesoscale atmospheric dynamics, which is embedded in to the large-scale atmospheric flow as also seen in the dominant period of several days for LV4 (Fig. 5). Furthermore, no contribution from the cold and warm advection mask is present, which shows that LV4 reflects the dominance of the processes other than the large-scale advection, highlighting single precipitation events of several hours with a recurrence period of several days. These events are embedded in the large-scale advection of cold and warm air (LV3), which is reflected in several similarities in the time series variations of LV4 and LV3 (see Fig. 3) and a moderate correlation of -0.54 between the two LV time series (see Fig. C1 in Appendix C).

In summary, LV4 illustrates the effect of mesoscale precipitation events on the horizontal visibility and cloud level in the marine boundary layer. These events are embedded in the large-scale advection of cold and warm air and lead to a clear increase in relative humidity and cloud coverage.

A2.3 LV13 – Extratropical cyclone activity

LV13 explains $2.6(\pm 0.2)\%$ of the variance and features predominantly low-frequency variations. The two most important OV's contributing to LV13 are the atmospheric pressure (P_{air}) and the cyclone mask (mask_{cyc}), which indicates the occurrence of extratropical cyclones along the ACE cruise

track. P_{air} and mask_{cyc} are anticorrelated as extratropical cyclones are identified by a minimum in P_{air} (Fig. A5). LV13 explains the largest part of the variability in P_{air} during ACE (Fig. 6) and illustrates that the passage of extratropical cyclones is the main reason for pressure variations over the Southern Ocean.

Extratropical cyclones are generally associated with precipitation, high wind speed and enhanced cloud cover (Field and Wood, 2007). The absence of precipitation and snow-fall rates (RR and SR) and wind speed ($u_{10\text{N}}$) and the anticorrelation of sky cover (SC) with mask_{cyc} in LV13 do not agree with the general picture of extratropical cyclones and might be related to the different dominant spatial and temporal scales of these variables compared to extratropical cyclones. While extratropical cyclones cover a relatively large area and were often identified over a period of several days and up to a week along the ACE track, the aforementioned variables show strong variations on the timescale from hours to a few days. Furthermore, RR, SR, $u_{10\text{N}}$, and SC are more strongly associated with specific features within extratropical cyclones, such as the cyclone's sectors and fronts (Hobbs, 1978; Browning, 1990), than with the entire cyclone as also shown with LV3 and LV4 (Figs. A3 and A4). The organisation of clouds along frontal structures could also explain the anticorrelation of SC and mask_{cyc} as areas of frequent cyclone occurrence do not coincide with the areas of high front frequencies, which are located equatorward of the cyclone maxima in the Southern Ocean (Papritz et al., 2014).

The increase in surface ocean seawater oxygen isotopic fraction ($\delta^{18}\text{O}_{\text{sw}}$) in areas with low atmospheric pressure could indicate an increased upwelling of subsurface waters that are characterised by higher $\delta^{18}\text{O}_{\text{sw}}$. The upwelling could occur either through increased surface mixing related to the passing storm or increased vertical advection associated with a surface divergence of the seawater.

The anticorrelation of some of the microbial biomass production indicators, namely the passive chlorophyll *a* fluorescence (Chl a_{fluo}), cryptophyte (Crypto), and diatom (DiatA) type contribution to chlorophyll biomass with the cyclone activity, may be due to light limitation introduced by the stronger wind-driven mixing in the water column. However, the enhanced mixing can also lead to upwelling or lateral advection of iron (Ellwood et al., 2015), which would benefit phytoplankton growth. Note that the contribution of LV13 to the variability of these biomass precursors is small (see Fig. 6).

There is no apparent explanation for the inclusion of carbon monoxide (CO), the mass concentration of sulfate in non-refractory particulate matter (SO_4^{2-}), and the atmospheric isoprene concentration ($\text{Isoprene}_{\text{air}}$), and further analysis is beyond the scope of this work. We mention them here because their contributing weight to the LV is larger than their single standard deviation from the bootstrap runs.

In summary, LV13 mainly represents the variations in atmospheric pressure due to the passage of extratropical cy-

clones, which are the main drivers of pressure variations over the Southern Ocean.

A3 The effect of islands, continental land, and sea ice

A3.1 LV5 – Distance to land

LV5 represents the ship's position relative to the closest landmass and associated terrestrial influences with positive values occurring close to land and negative ones for the open-ocean sections (see Fig. A6a). It captures $4.0(\pm 0.3)\%$ of the variability in the dataset.

As shallower waters are found closer to land, water depth (d_{water}) and distance to land (d_{land}) each exhibit a positive loading. Both variables represent the highest contributions to LV5. The geostrophic velocity (U_g) is generally low in the shallower continental shelf waters where large-scale oceanic horizontal pressure gradients are absent. In conjunction with a positive loading for U_g , this effect is represented by high LV5 values close to land. The available light within the surface mixed layer of the water column (I_g) also appeared to decrease at locations closer to landmasses. The reduction of I_g is likely driven by increased light attenuation from higher particulate matter concentrations in the surface ocean (Tilzer et al., 1994; Perissinotto et al., 1992; Blain et al., 2001) or changes to the depth of the surface mixed layer (by definition, I_g is the median light intensity within the mixed layer; see Sect. S1.9 “Microbial, biogeochemical and optical properties” in the Supplement and Behrenfeld et al., 2005). This is due to, e.g. variations in the bathymetry, horizontal water flows, or introduction of fresh water sources (Dong et al., 2008).

A connection between marine and atmospheric quantities is made through the cold and warm temperature advection mask (mask_{CW}). Here, the negative loading could indicate advection of (terrestrial) warm air near land, rather than glacier-covered islands, in the Indian Ocean and Atlantic Ocean sectors. Warm-air advection is underlined by a negative loading for air temperature (T_{air}) and positive loading for relative humidity (RH), indicating drier and warmer air close to land. Further, negative loading for the rain rate (RR) and the wind speed at 10 m above mean sea level ($u_{10\text{N}}$) can be seen, which might be related to their orographic enhancement near land. During ACE, atmospheric frontal systems often passed while the ship was close to subantarctic islands. Therefore, a negative loading for $u_{10\text{N}}$, mask_{CW} , and RR might be due to a coincidental overlap of island visits and the passage of frontal systems. For the height of the lowest cloud level (CL), a negative loading was found, indicating that the cloud deck was lower over the open ocean where moist air (negative loading of RH) leads to a lower cloud condensation level.

Negative weights for the ratio of coarse fluorescent to total aerosol particles ($r_{\text{fluo,coarse}3\sigma}$) and ice-nucleating particle concentrations at both -8°C ($N_{\text{INP,LV,-8}}$) and -20°C

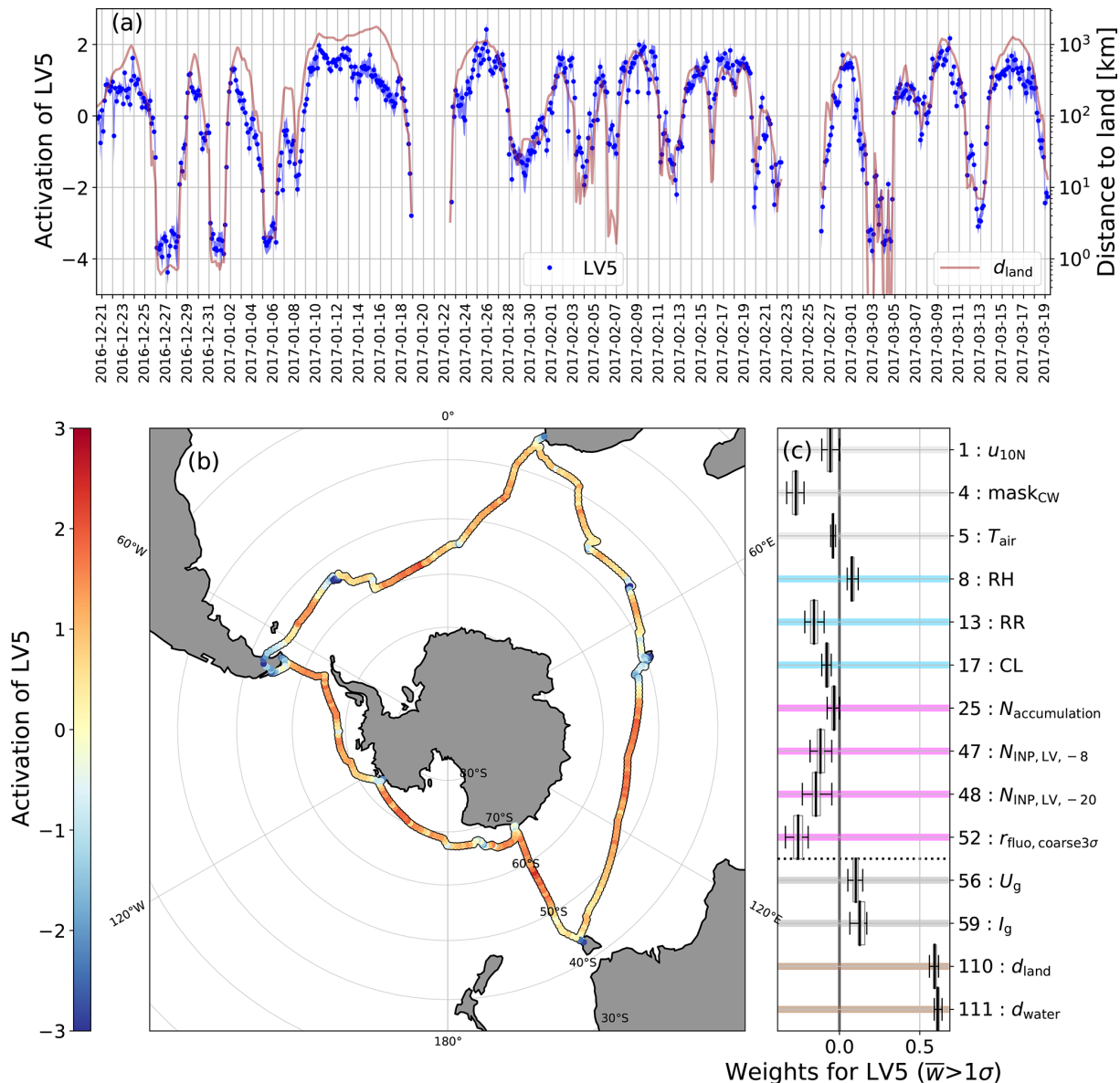


Figure A6. (a) Time series of the activation of LV5 (left axis) and of the distance to the nearest shoreline (d_{land} , right axis). (b) Map of the ship track coloured by the activation of LV5. (c) Box and whisker plots of the activated weights.

($N_{INP, LV, -20}$) show an increase closer to land. Particles acting as INP at different temperatures are associated with different particle sources (-8°C : biogenic origin; -20°C : mineral origin). Fluorescent particles can be emitted from the ocean during sea spray generation (Wilson et al., 2015) but can also originate from land, in which case they would correspond to pollen, fungal spores, and plant or animal detritus (Després et al., 2012; Fröhlich-Nowoisky et al., 2016). Such types of biological particles are known to act as INP efficiently at higher temperatures (Kanji et al., 2017). Therefore, the grouping of fluorescent aerosol particles with independently measured INP is consistent with expectations. The fact that both types show elevated concentrations near

land points towards coastal regions with increased oceanic biological activity and vegetated land being the source (Mason et al., 2015; McCluskey et al., 2018). In addition, accumulation mode particles ($N_{Accumulation}$) exhibit a weak negative loading. It is conceivable that more condensable trace gases are emitted from land and productive coastal areas that contribute to accumulation mode particle formation. On the continents, human activities lead to emissions, and on subantarctic islands animal colonies are responsible for ammonia emissions (Schmale et al., 2013), a precursor to secondary aerosol mass.

In summary, LV5 demonstrates terrestrial influences on measurements when the ship's track is close to land. Visits

to smaller islands and the larger continental ports coincided with increased concentrations of ice-nucleating and fluorescent particles, as well as frontal systems that influenced air temperature and humidity as well as the altitude at which clouds formed.

A3.2 LV9 – Marginal sea ice zone and snowfall

LV9 has a very distinct regional signal that is mostly active during leg 2 of the cruise, with a clear peak between 27 January and 2 February 2017 when the ship was going through sea ice while approaching and leaving the Mertz region (Fig. 4a and b). Despite its variance being limited to a relatively short part of the expedition, LV9 explains $3.4(\pm 0.6)\%$ of the variance of all 111 variables (Table 2). The largest contribution to this LV comes from the sea ice concentration (C_i), i.e. fraction of surface area covered by sea ice (see Fig. 4c and the weights table for LV9 in the Supplement). Generally, sea ice cover in the Southern Ocean was unusually low during the austral summer season 2016/2017 (Schlosser et al., 2018), so much so that the cruise could go further south than originally planned during large parts of leg 2 (Walton and Thomas, 2018). The only other region where the ship went through broken sea ice was around Peter I Island, where LV9 has a much smaller and shorter secondary peak on 15 and 16 February 2017 (Fig. 4a and b). According to the satellite-derived sea ice concentration, the ship only went through partial ice cover, with a maximum of 48 % ice cover in the Mertz region on 31 January 2017.

A second set of prominent signals associated with the positive LV9 periods are a low surface ocean salinity (S_{sw}) and density ($\sigma_{0,sw}$; Fig. 4c). Relatively fresh and light surface waters in conjunction with a partial sea ice cover suggest a stable surface ocean stratification associated with recently melted sea ice, since sea ice is the dominant driver of the surface ocean salinity and stratification in the high-latitude Southern Ocean (Haumann et al., 2016). While other surface freshwater fluxes such as snow and glacial melt could have been responsible for the low-salinity surface ocean in this region, the absence of a low $\delta^{18}O_{sw}$ in LV9 suggests no significant contribution of these fluxes to this LV. This interpretation is confirmed by the dominant sea ice contribution to the surface ocean freshwater flux balance in the Mertz region during ACE (Haumann et al., 2021). The low surface ocean salinity and density associated with LV9 might be the cause for other, smaller peaks in the LV9 time series in the absence of sea ice (Fig. 4a).

An interesting observation is the large contribution of the wave period ($T_{m-1,1}$) to LV9 (Fig. 4c), with a longer surface wave period in the partially ice-covered regions. Ice floes in the marginal ice zone dissipate wave energy (Squire, 2020; Arduin et al., 2020) with a faster rate for short-wave components of the spectrum (Meylan et al., 2018). The sPCA confirms these results, with a significantly longer wave period in the partially ice-covered region when LV9 is positive,

but no substantial effects are noticed for the surface significant wave height.

Snowfall (SR) has the fourth largest contribution to LV9 and occurred both during the time in the sea ice in the Mertz area and in regions outside the sea ice cover in the south Pacific sector (Fig. 4a) under varying atmospheric conditions. While a higher contribution of snowfall compared to rainfall is expected near the Antarctic coast in summer, it is unclear if there is a link between snowfall and the presence of sea ice in LV9. In the Mertz region, where LV9 is active, the 2 d back trajectories initiated near the surface are found predominantly over the continent with some contribution from the oceanic regions (see Supplement Sect. S4). The snowfall occurring during this period is due to the advection of maritime air masses associated with transient low-pressure systems near the Adélie Land coast observed during ACE, as typically found in this area (Servettaz et al., 2020). ACE radiosonde profiles showed a tendency for the RH increasing at upper levels prior to snowfall events, while during snowfall the entire boundary layer was near or at water vapour saturation. This confirms the back-trajectory analysis (see Supplement Sect. S4) showing that the maritime air advection happens in the upper marine boundary layer, while near-surface layers are dominated by a concurrent advection of continental air. The latter vertical atmospheric structure has been observed at the Adélie Coast during the advection of moist air at upper levels in the warm sector of extratropical cyclones (Vignon et al., 2019; Jullien et al., 2020).

The very low abundances of heavy water molecules (δ^2H_{vap} and $\delta^{18}O_{vap}$) of atmospheric water vapour (w) in LV9 are likely dominated by low isotopic values observed near the Mertz Glacier and are characteristic for Antarctic air masses. Due to the close proximity to the continent and the presence of sea ice acting as a barrier between the ocean and the atmosphere, it is possible that the continental air mass is only marginally affected by surface fluxes before it reaches the open ocean, which has, for example, been observed in airborne measurements over the Labrador Sea (Renfrew and Moore, 1999). A dominant signal of Antarctic air masses near the surface over the sea ice near the Mertz Glacier would also explain the low carbon monoxide (CO) concentrations in the air, since Antarctic air would be expected to contain less CO. Interestingly, near-surface relative humidity (RH) is slightly higher during positive activations of LV9, which might be caused by (i) moist advection from the ocean during snowfall events, (ii) evaporation from the ocean surface in fractured sea ice zones during advection of continental air, and possibly (iii) the sublimation of deposited or falling snow. Moreover, the low air temperature above the sea ice can further increase RH due to the temperature dependency of the saturation vapour pressure. More detailed analyses, which go beyond the scope of this study, are needed to assess the relative importance of these processes for the situation represented by LV9.

Net community production (NCP) and phytoplankton biomass (as estimated by the fluorescent chlorophyll *a* concentration $\text{Chl } a_{\text{fluor}}$) are both positively correlated with LV9. Cassar et al. (2011) showed that NCP in the Southern Ocean was consistently low when mixed layers are deeper than about 45 m, regardless of iron availability, suggesting light limitation to be the driving factor. For shallower mixed layers, NCP correlated with iron sufficiency as estimated by variable fluorescence. In this regard, sea ice melt could influence water column productivity through (1) Fe fertilisation (Lannuzel et al., 2008, 2016) and/or (2) enhanced water column stratification, relieving light limitation (Vernet et al., 2008; Cassar et al., 2011; Eveleth et al., 2017). Mixed-layer depths in 32 profiles in the Mertz region were generally shallower than 40 m (average $24 \text{ m} \pm 11 \text{ m}$). Hence, relief from light or iron limitation due to ice melt could explain the LV9 NCP pattern.

In summary, LV9 provides interesting new insights into processes associated with melting sea ice in the marginal ice zone and snowfall during the austral summer. These processes include a salinity-driven stable surface ocean stratification, an associated phytoplankton bloom, dissipation of surface waves, and an atmospheric boundary layer that is dominated by Antarctic continental air masses near the surface with moist and warm advection aloft producing snowfall at times.

A4 Atmospheric microphysical and chemical processes

A4.1 LV2 – Drivers of the cloud condensation nuclei population

LV2 explains the second largest fraction of variance of all 111 OV_s ($4.4(\pm 0.5)\%$). The activation of LV2 positively correlates with the concentration of cloud condensation nuclei at a supersaturation of 0.15 %, 0.3 %, and 1.0 % ($N_{\text{CCN},0.15}$, $N_{\text{CCN},0.30}$, and $N_{\text{CCN},1.00}$) very closely (Fig. A7a). The most positive activations of LV2 (corresponding to high N_{CCN}) are near the continents, the islands in the Indian Ocean, and along the coast of Antarctica in the Pacific sector (Fig. A7b). The same locations were identified by Schmale et al. (2019) for $N_{\text{CCN},0.20}$ in a study focused on the ACE aerosol measurements.

The number of available CCN is strongly connected to the particle number in the accumulation mode ($N_{\text{accumulation}}$), particles between roughly 80 nm and 1 μm in diameter, which is also strongly positively correlated to LV2. Moreover, particulate sulfate (SO_4^{2-}) follows the same pattern. It is known to contribute a large mass fraction to the accumulation mode over the Southern Ocean (e.g. Raes et al., 2000; Quinn et al., 2017). There, one important source of particulate sulfate is the pathway via photooxidation of dimethyl sulfide (DMS) emitted by marine microbial activity (Quinn and Bates, 2011; Weller et al., 2011). In parallel to sulfate, methanesulfonic acid (MSA) is produced and also con-

tributes to accumulation mode particle mass. Schmale et al. (2019) observed a connection between MSA concentration as measured by 24 h filter samples ($N_{\text{MSA},\text{PM}_{10}}$) and the CCN number concentration. This link is not reflected in LV2. The absence might be due to the low MSA sampling frequency (daily samples), which is a limitation to the here presented analysis (see Sect. 3.5).

Particulate chloride (Cl^-), a surrogate for sea spray, and the number concentration of coarse particles, a proxy for sea spray (N_{seaspray}), correlate positively with LV2, indicating their contribution to the CCN budget. Their variability contributes less than those of sulfate and the accumulation mode. While sea spray particles are extremely good CCN, the smaller contribution to LV2 can be expected because their absolute contribution to the CCN budget is smaller than that of the accumulation mode (Schmale et al., 2019). Large sea spray particles defined here as $> 700 \text{ nm}$ only occur in low number concentrations.

The CCN population is linked to the hygroscopicity of the particle ensemble, which is expressed as the hygroscopicity parameter κ at different supersaturations (Petters and Kreidenweis, 2007) ($\kappa_{0.15}$, $\kappa_{0.3}$). More in-depth analysis shows that the hygroscopicity decreases with decreasing CCN number Schmale et al. (2019). The positive relation might be caused by the air mass history, i.e. washout of more hygroscopic particles is consistent with the decrease in availability of CCN. The sPCA does not directly account for air mass history because upstream measurements are not available. To check our hypothesis concerning washout, we investigated the precipitation rate along the backward trajectories for the previous 3 d (see Fig. A8). The 72 h integrated surface precipitation along the trajectories shows high precipitation in situations with low CCN number and sulfate concentrations. This correlation agrees with our hypothesis of a simultaneous decrease in CCN number concentration and the particles' hygroscopicity due to the washout of hygroscopic particles during precipitation. The positive correlation of the weights of cold and warm temperature advection masks (mask_{CW}) and CCN number concentrations in LV2 seems to be in contradiction to this hypothesis because enhanced precipitation is expected during warm-air advection (see also LV3), which would lead to low CCN number concentrations. Furthermore, an opposite correlation of mask_{CW} and accumulation mode aerosols in LV2 and LV3 is seen, which could indicate that different processes during warm-air advection are important in these two LVs. While LV3 mainly represents the contrasting properties of cold- and warm-air advection, which includes the rainout of accumulation mode aerosols during warm air advection, mask_{CW} in LV2 might represent the relevance of cloud processes for CCN number concentrations. The frequent formation and dissipation of clouds during warm air advection might be conducive to the formation of accumulation mode aerosol and CCN through heterogeneous sulfate chemistry, i.e. addition of sulfate to particles through processes in cloud droplets (Hoppel and Frick,

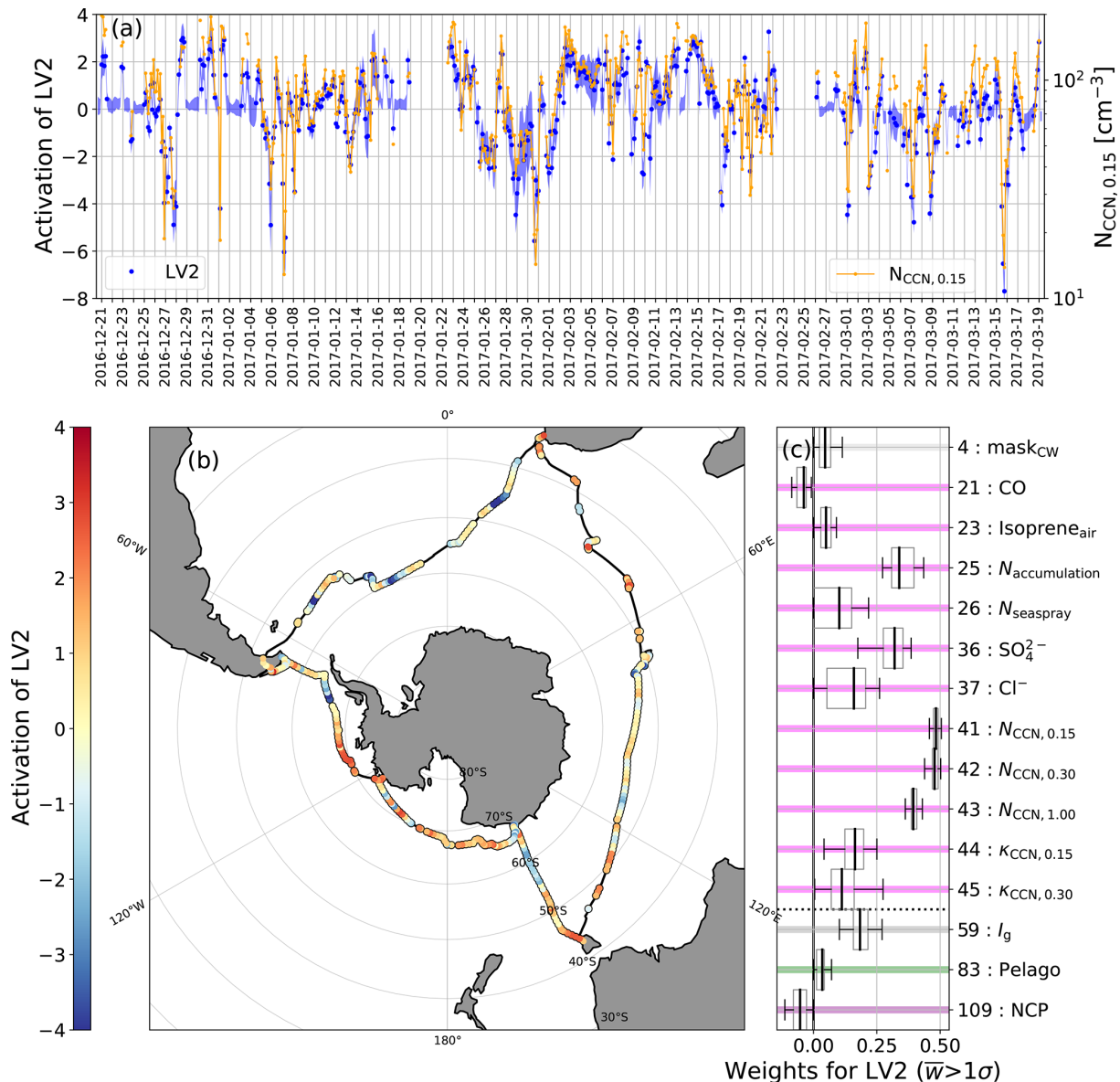


Figure A7. (a) Time series of the activation of LV2 “Drivers of CCN population” (left axis) and of the CCN number concentration at 0.15 % super saturation ($N_{\text{CCN},0.15}$, right axis). (b) Map of the ship track coloured by the activation of LV2. (c) Box and whisker plots of the activated weights.

1990; Schmale et al., 2019). This may lead to a positive correlation of CCNs and the mask_{CW} . Further investigations are needed to clearly identify the relevant processes during precipitation and in clouds for the CCN number concentrations represented by LV2. We refer the reader to Lee et al. (2013) for a comprehensive investigation on aerosol processes relevant to CCN number concentrations and their uncertainty.

In summary, LV2 represents the particles and chemical constituents able to act as CCN and the processes leading to variability in CCN number concentrations. For ACE, the CCN number concentrations are strongly related to the accumulation mode and sulfate concentrations. The main process

leading to variability in CCN number concentrations most likely is the washout of hygroscopic particles due to precipitation upwind of the measurement site.

A5 LV12 – Wind-driven conditions and sea spray aerosol

LV12 groups the OV_s related to sea spray aerosols (SSAs) along with some meteorological (wind speed, cyclone flag) and physical oceanographic (significant wave height) variables (see Fig. A9). This grouping is consistent with the known mechanisms of sea spray aerosol production (Lewis

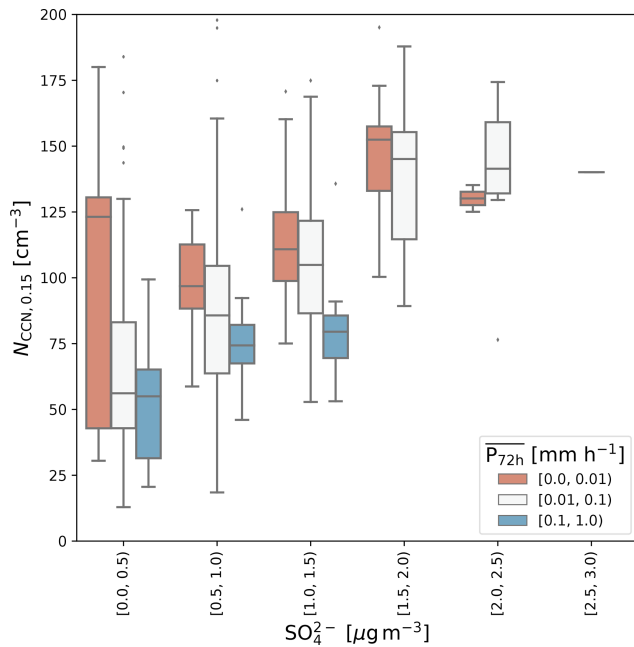


Figure A8. Box and whisker plots of $N_{\text{CCN},0.15}$ as a function of the particulate SO_4^{2-} concentration and the average ERA5 total precipitation rate along the air mass back trajectories over 72 h before arrival.

and Schwartz, 2004): surface winds generate breaking waves and resulting bubble clouds known as whitecaps. When the submerged bubbles rise to the ocean surface and burst, they eject droplets of seawater into the atmosphere (Monahan et al., 1986). These droplets dry out and form so-called sea spray aerosol. The strong correlation of wind speed ($u_{10\text{N}}$), significant wave height (H_s), and SSA number concentrations ($N_{\text{sea spray}}$) to LV12 are entirely consistent with these physical processes, as well as the weaker correlation of the cyclone flag variable (mask_{cyc}), which is associated to stronger winds.

SSA particles are composed of complex mixtures of sea salt compounds, organic compounds, and marine biological material (Quinn et al., 2015). Therefore, the mass concentrations of sea-salt-related elements measured in aerosol samples also contribute positively in LV12 (i.e. chloride, Cl^- ; sodium, $N_{\text{sodium,PM}_{10}}$; magnesium, $N_{\text{magnesium,PM}_{10}}$; potassium, $N_{\text{potassium,PM}_{10}}$; sulfate, SO_4^{2-} ; bromide, $N_{\text{bromide,PM}_{10}}$; calcium, $N_{\text{calcium,PM}_{10}}$, where the latter four have median weights smaller than 1 standard deviation and are therefore not shown in Fig. A9c). This grouping is consistent with previous studies that have observed moderate to strong correlations between the number of SSA particles and the aerosol mass concentrations of elements comprising sea salt (Modini et al., 2015; Quinn et al., 2017). Since SSA particles contain sea salt they are hygroscopic and efficient CCN. Therefore, it is interesting to note that all of the CCN OV's are absent in LV12. The absence can be explained by recent studies

that suggest that, on average, SSA particles only form a minor fraction of the total marine CCN budget (Modini et al., 2015; Quinn et al., 2017; Schmale et al., 2019), which instead appears to be dominated by accumulation mode non-sea salt sulfate aerosols (e.g. see the discussion of LV2 in Appendix A4.1).

In terms of aerosol size distribution modes smaller than sea spray, the concentration of accumulation mode aerosol particles makes a strong negative contribution to LV12 (i.e. it is anticorrelated to wind speed and SSA concentrations). Accumulation mode particles likely contain large fractions of particulate sulfate, produced secondarily, including by aqueous-phase cloud processes (see LV2 Sect. A4.1). They are also efficient CCN. The anticorrelation between the concentrations of SSA and accumulation mode particles in this LV could have potential physical explanations. For example, the onset of windy and stormy conditions conducive to very strong SSA production and net enhancement of SSA concentrations may also result in less photochemical or cloud-processed sulfate production (Fossum et al., 2020) or increased losses of accumulation mode particles through deposition on the ocean surface (Landwehr et al., 2020) or by precipitation scavenging (see the discussion of LV3 and LV4 in Sects. A2.1 and A2.2), which would all tend to suppress accumulation mode particle concentrations. However, the observed anticorrelation between SSA and accumulation mode aerosol concentrations could potentially also be explained by a methodological, misclassification artefact related to the mode fitting analysis procedure that was used to separate these two size distribution modes (see Supplement Sect. S1).

The size distributions of dried SSA particles peak at diameters of around $0.2\ \mu\text{m}$ and therefore contain substantial contributions from particles with diameters in the range from ~ 0.1 to $1\ \mu\text{m}$ (Prather et al., 2013). The strong contribution to this size range means that SSA particles are effective at scattering solar radiation and thereby reducing visibility through the atmosphere. The strong negative weight of visibility in LV12 (i.e. anticorrelation between visibility and SSA concentrations) is consistent with this physical reasoning. The median light intensity in the mixed layer below the ocean surface (I_g) also makes a strong negative contribution to LV12 (i.e. it anticorrelates with SSA concentrations). This OV is derived from measurements of the photosynthetically active radiation available at the ocean surface and the oceanic mixed-layer depth (see Supplement Sect. S1 and glossary entry for I_g in Appendix F). Since the measured photoreactive radiation does not contribute to LV12, the negative contribution of I_g to the LV is more likely a result of a deepening of the mixed-layer depth during stormy conditions.

The time series of LV12 activation (Fig. A9a) is consistent with a weather-driven process. LV12 was activated episodically as synoptic-scale weather systems passed over the research vessel every 3 to 6 d. This is consistent with previous marine aerosol studies that suggested that SSA production is an episodic process occurring during higher wind speed

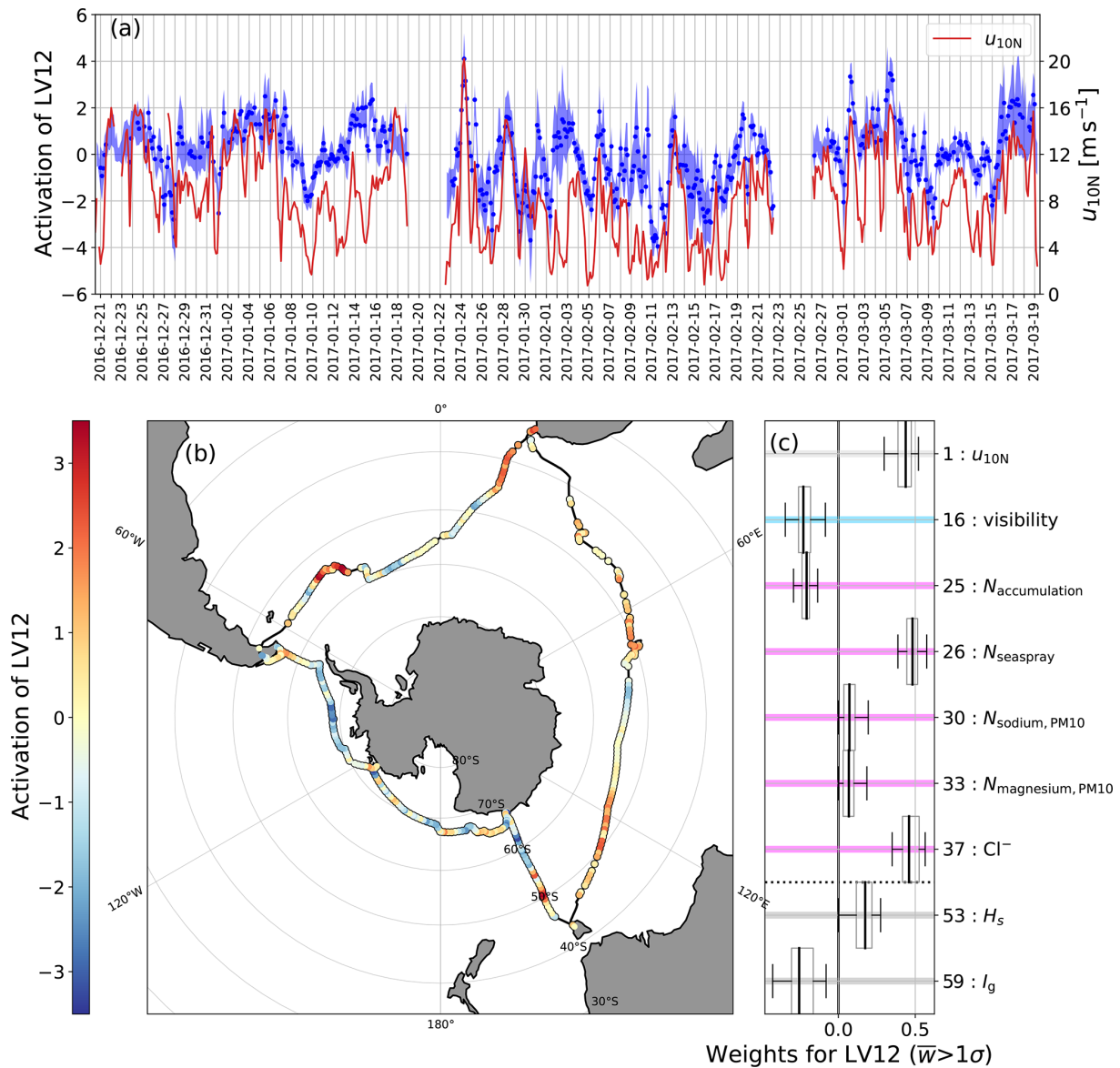


Figure A9. (a) Time series of the activation of LV12 “Wind-driven conditions and sea spray aerosol” (left axis) and the 10 m neutral wind speed (u_{10N} , right axis). (b) Map of the ship track coloured by the activation of LV12. (c) Box and whisker plots of the activated weights.

conditions (e.g. Modini et al., 2015). The map of LV12 activation (Fig. A9b) clearly shows that LV12 was most consistently positively activated during the open-ocean legs 1 and 3, where weather systems with strong winds were encountered (see also Schmale et al., 2019). During leg 2, close to sea ice and the Antarctic continent, the baseline of LV12 is shifted and positive activations of LV12 appear for shorter and sharper periods, which may have been related to shifting regional wind directions between the ocean and the continent.

In summary, LV12 describes the production of sea spray due to stormy conditions and the absence of accumulation mode aerosols in these instances.

A6 Ocean microbial dynamics

Latent variables LV6, LV8, and LV11 work in concert to capture the major physical and chemical features that dictate the dynamics of phytoplankton and bacteria in the sunlit layer of the Southern Ocean and their biogeochemical activity. Collectively they explain 10.2% of the variance in the 111 OVs (see Table 2), with 59 OVs across the 3 LVs having weights $\bar{w} > 1\sigma$. In the Southern Ocean, critical resources for phytoplankton and bacteria include macronutrients such as silicate (captured by LV11) and micronutrients such as iron (Fe; LV6 and LV8 for Fe fertilised and Fe limited productivity, respectively), as well as light availability. However, the distribution and interplay of these resources is spatially and tem-

porally heterogeneous (Boyd, 2002). Both the sub-optimally low photochemical efficiency of photosystem II measured during the night ($F_V F_M$, Fig. A12) and persistent low ratio of dissolved iron:nitrate measured from Cape Town to Punta Arenas (Janssen et al., 2020) suggested generally Fe-limited productivity during ACE, as previously reported in the Southern Ocean (Moore et al., 2013).

A6.1 LV11 – Surface nutrient concentrations associated with mixing events, climatic, and frontal zones

LV11 (Fig. A10) activation corresponds primarily to the dissolved concentrations of nitrate and phosphate, which are positively correlated with the LV activation. The distribution of these nutrients is controlled by physical processes, biological consumption, and respiration and remineralisation (Sarmiento et al., 2004; Freeman et al., 2018). The strongest negative activation of LV11 occurs south of Africa near the Subantarctic Front (SAF) in the Atlantic Sector and near the Subtropical Front (STF) in the Indian Sector. The major ocean fronts in the Southern Ocean physically divide the surface ocean, resulting in distinctly different surface seawater properties in the zones between the fronts. Moving southwards, nutrient-rich deep waters are progressively raised closer to the surface and subsequently entrained into the mixed-layer (Pollard et al., 2002; Weber and Deutsch, 2010), resulting in increased nitrate, nitrite and phosphate concentrations. Silicate has a lower contribution to LV11 compared to other nutrients, as stable high concentrations are only observed south of the Southern Antarctic Circumpolar Current Front (SACCF) in the signal of LV14.

The biological OV's contributing to activation of LV11 (OV's Chl a_{fluo} , particulate organic carbon (POC), particulate organic nitrogen (PON), $N_{\text{totalbacteria}}$, $r_{\text{fluo,coarse}3\sigma}$, and $r_{\text{fluo,fine}3\sigma}$, explained below) are a product of the nutrient supply to the surface ocean and the complex controls on productivity across the Southern Ocean. Despite high concentrations of macronutrients (OV's nitrate and phosphate), iron acts as a key limiting nutrient for biological growth as indicated by low dissolved Fe concentrations (Janssen et al., 2020) and by persistently low photosynthetic efficiency throughout the voyage ($F_V F_M < 0.3$; further explored in LV8). Hence, much of the Southern Ocean is classified as a high-nutrient low-chlorophyll (HNLC) region.

This low growth–high (macro-)nutrients vs. high growth–low (macro-)nutrient scenario within HNLC areas drives the anticorrelation observed between nutrient concentrations and the overall biomass “indicators” chlorophyll a (from fluorescence; Chl a_{fluo}), particulate organic carbon (POC), particulate organic nitrogen (PON), and bacterial abundance ($N_{\text{totalbacteria}}$) in LV11. Chl a , POC, and PON are the major organic pools synthesised by phytoplankton for use in, or as a result of, their photosynthetic process (Cullen, 1982). Bacterial abundance has a relatively high negative contribution to LV11 (see Fig. A10), as bacterial concentrations are

linked to the availability of dissolved organic matter (a product of particulate organic matter including POC and PON) and nutrients (Church et al., 2000; Kirchman et al., 2009).

The ratio of coarse and fine fluorescent aerosol particles to total aerosol particle numbers in the atmosphere ($r_{\text{fluo,coarse}3\sigma}$; $r_{\text{fluo,fine}3\sigma}$), which are negatively correlated with LV11 activation, are also linked with bacterial concentrations in the Southern Ocean (Moallemi et al., 2021). The likely source of the fluorescent particles is sea spray enriched with organic matter, specifically bacteria (Moallemi et al., 2021).

The complex interactions between microbial biological OV's and biogeochemical OV's drives the remaining LV11 activation not described above. Negative activation of LV11 near Mertz and Siple Island was due to enhanced growth of phytoplankton, which also increased biological consumption of nitrate and phosphate, as observed by Janssen et al. (2020) at Mertz. A subtle signature of negative LV11 activation is also observed at locations near subantarctic islands and the Antarctic landmass where increased phytoplankton productivity and growth are indicated by Chl a_{fluo} . The influence of the islands on phytoplankton productivity is explored further in LV6. Conversely, the strongest positive activation of LV11 occurs in the open-ocean regions away from oceanic frontal and landmass influences, particularly evident south of the Polar Front (PF) in the Pacific and Atlantic sectors. These positive activations share similarities with the biological responses captured in LV8 in relation to severe Fe limitation (captured by $F_V F_M < 0.3$).

In summary, LV11 captures the availability of dissolved macronutrients in the Southern Ocean and the complex relationships between dissolved nutrient availability and the growth and productivity of phytoplankton and bacteria.

A6.2 LV6 – Iron-fertilised biological productivity

Activation of LV6 (Fig. A11a) closely follows the patterns in POC, PON, and Chl a concentration (TChl a and Chl a_{fluo} ; Fig. A11b), where increases are attributed to an increase in larger-sized phytoplankton. These larger-sized phytoplankton include diatoms (DiatA, DiatB) and haptophytes (Hapto67), the latter likely also contributing to the nanoeukaryote population ($N_{\text{nanoeukaryotes}}$). As a result, presence of these taxa increased the overall particle size ($< 100\mu\text{m}$) demonstrated by a flattening (or reduction) in the particle size slope (PSDslope). Diatoms and *Phaeocystis* sp. (a type of haptophyte) are well-known opportunistic bloom-forming species in the Southern Ocean, which can rapidly respond to iron replenishment and are widely linked to increases in Chl a and carbon production (Schoemann et al., 2005; Arrigo et al., 2010).

The strongest activation of LV6 (Fig. A11) occurred at biological hotspots within the Southern Ocean. These include subantarctic islands and glaciers, specifically Siple Island and Mertz Glacier, where alleviation from iron limi-

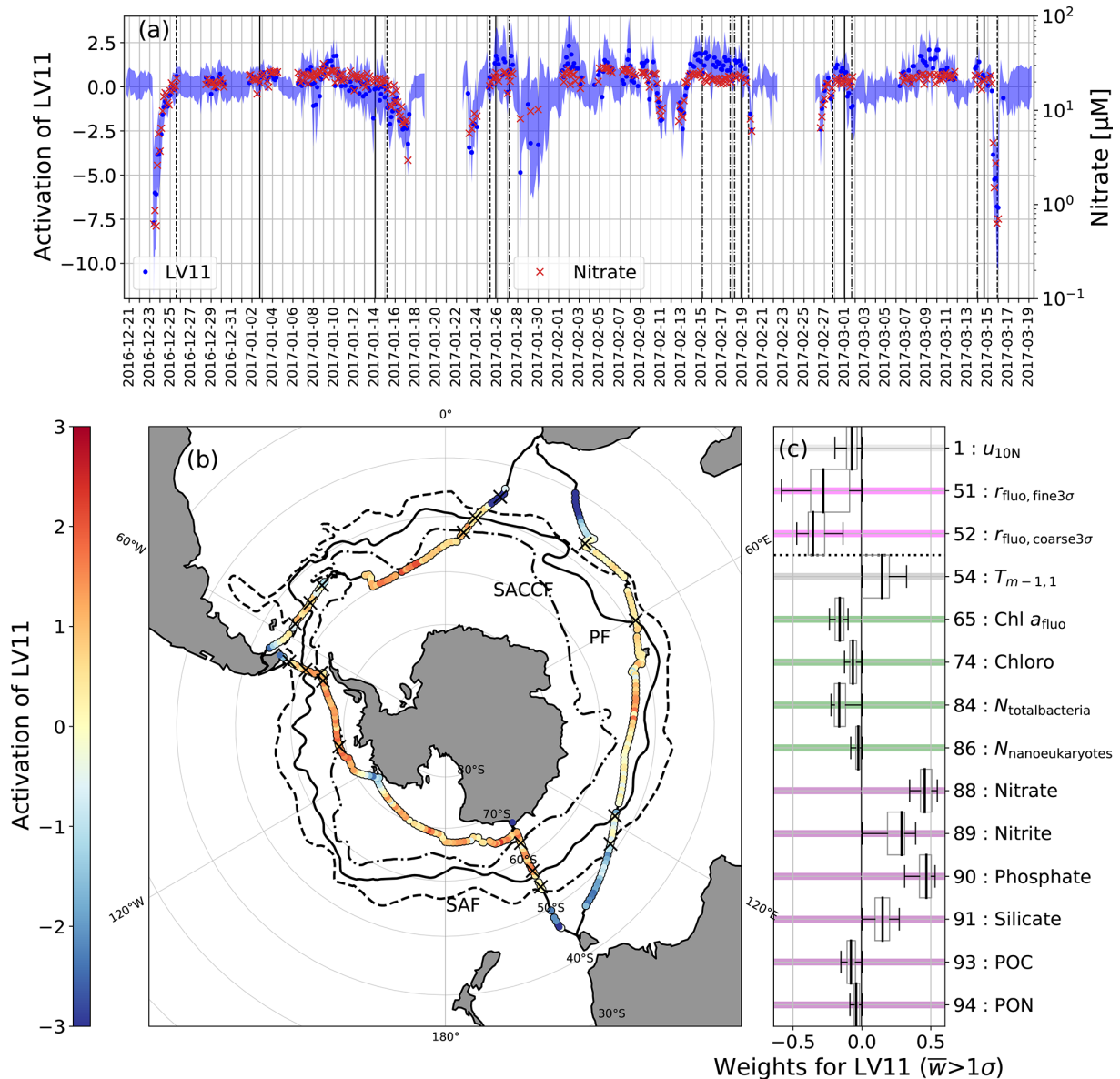


Figure A10. (a) Time series of the activation of LV11 and the concentrations of nitrate (right axis). (b) Map of the activation of LV11. (c) Weights of the OV contribution to LV11 for which the bootstrap median was larger than 1σ . See caption of Fig. A1 for details on the oceanic fronts and frontal crossings.

tation is known to occur due to terrestrial–marine interactions attributed to the island mass effect (IME) (Doty and Oguri, 1956; Blain et al., 2007), sea ice and glacial melting, and changes in currents (satellite derived geostrophic flow, U_g ; Blain et al., 2001; Mongin et al., 2008; Hawkings et al., 2014). Such localised Fe enrichment was measured at Mertz, Balleny, and Kerguelen islands during ACE (Janssen et al., 2020). Iron enrichments in the surface waters from the Ross Sea and the Atlantic sector could be related to sedimentary and sea ice inputs (Coale et al., 2004; Lannuzel et al., 2010), while IME and atmospheric dust deposition could be invoked in the Atlantic sector (Jickells et al., 2005; Cas-

sar et al., 2007). In these Fe-enriched hotspots, the highest concentrations of Chl a and marine particulate organic matter and the highest abundances of diatoms and haptophytes were observed. In addition, the ratio of Chl a degradation pigments to Chl a , including pheophorbide a (Pheoba) and pheophytin (Phaephyta), increased significantly, suggesting increased consumption by zooplankton (Shuman and Lorenzen, 1975; Ingalls et al., 2006), which can intensify the Fe recycling and iron ability to support net community production (NCP). In contrast, the ratio of the Chl a degradation pigment chlorophyllide a (Chlide a ; an indicator of cell death) to Chl a decreased significantly (Wright et al., 2010).

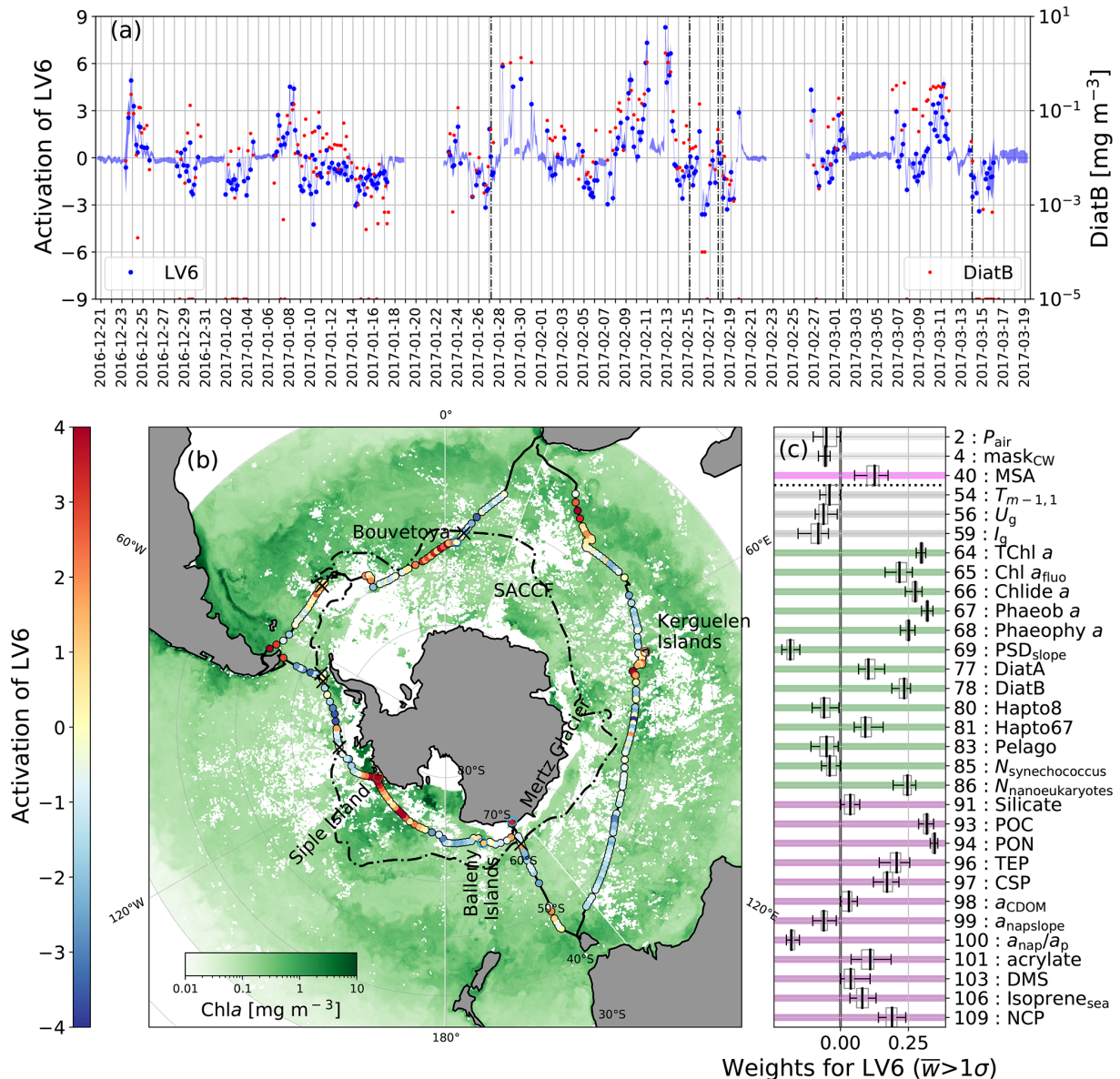


Figure A11. (a) Time series of the activation of LV6 (left axis) and the pigment biomass attributable to diatom type phytoplankton (DiatB, right axis). (b) The activation of LV6 over a satellite-derived map of monthly average Chl *a* concentrations (18 December to 16 January for the Indian ocean sector, 17 January to 17 February for the Pacific sector and 26 February to 21 March for the Atlantic sector). (c) Weights of the OV contributions to LV6 for which the bootstrap median was larger than 1σ . See the caption of Fig. A1 for details on the oceanic fronts and frontal crossings.

The vigorous biological productivity associated with LV6 is further supported by activation of LV6 following NCP patterns. NCP, the balance between photosynthetic carbon fixation by phytoplankton and community carbon consumption by respiration, was generally consistent with trends in Chl *a* and marine particulate organic matter. This is to be expected as NCP is equal to net primary production (NPP) minus heterotrophic respiration, and Chl *a* generally correlates with NPP. Strong correlations between NCP and Chl *a* have been reported in earlier studies (Cassar et al., 2011). Exceptions to

this appear on transit between the Balleny and Scott Islands (4 to 5 February 2017) and on transit northward through the Antarctic and Polar Frontal Zones in the Atlantic Sector (14 to 16 March 2017) where NCP is not correlated with Chl *a* and is also abnormally low ($< -10 \text{ Mmol O}_2 \text{ m}^{-2} \text{ d}^{-1}$). Apparent deep mixing in these areas likely results in light limitation leading to a reduction in NCP as has been observed previously (Cassar et al., 2011).

Activation of LV6 is also driven by seawater transparent exopolymer particles (TEP), Coomassie stainable parti-

cles (CSP), and to lesser extent acrylate and dissolved isoprene (C_5H_8). In addition to synthesising POC and PON, phytoplankton also produce and release gel-like organics such as polysaccharide-rich TEP (Zamanillo et al., 2019) and protein-rich CSP (Engel et al., 2020), the biogenic trace gas isoprene, and the organic compound acrylate, which is a non-volatile byproduct of the production cycle of the trace gas dimethyl sulfide (DMS). As documented in other publications, each of these secondary compounds are positively correlated with phytoplankton biomass indicators (Chl *a*, POC, PON; Zamanillo et al., 2019; Rodríguez-Ros et al., 2020), abundances of diatoms (DiatA, DiatB; Zamanillo et al., 2019; Rodríguez-Ros et al., 2020), and haptophytes (Hapto67; Zamanillo et al., 2019; Rodríguez-Ros et al., 2020; Kinsey et al., 2016), all of which show important contributions to LV6. Even though the contribution of seawater DMS was very low, there was a considerable positive contribution by one of its atmospheric oxidation products, gaseous methanesulfonic acid (MSA). However, this latter contribution appears to be mostly driven by a period of high atmospheric MSA concentrations in the vicinity of Bouvetøya Island, coinciding with increased ocean microbial activity. Oxidation of DMS is the only known source of MSA; therefore, it is difficult to explain a direct causal link between the higher MSA concentration and the enhanced microbial activity without a correspondingly higher DMS concentration, which was not measured in this case. In general, it is rare to observe a direct connection between microbial activity in the ocean and DMS oxidation products such as MSA and sulfuric acid when using linear correlation analysis. This is due to, for example, the relatively long lifetime of atmospheric DMS (2 to 5 d in the Southern Ocean) (Chen et al., 2018) and the influence of various environmental conditions on the different oxidation product yields (Barnes et al., 2006).

In summary, LV6 depicts hotspots of biological productivity by phytoplankton and bacteria, which are driven largely by the island mass effect.

A6.3 LV8 – Iron-limited biological productivity

Many OV's contribute to LV8, which in essence appears to represent the typical HNLC waters of the Subantarctic and Polar Frontal Zones of the Southern Ocean, depicting the resource limited open-ocean environment, where biomass accumulation (e.g. total chlorophyll *a*; TChl *a*) and productivity is commonly co-limited by light and iron availability (Boyd, 2002; Boyd et al., 2007) (Fig. A12b) and also potentially by silicate availability north of the SACCF.

In HNLC waters, the microbial community is more diverse than in higher-productivity waters (Ishikawa et al., 2002; Wright et al., 2010; Wolf et al., 2013; Cassar et al., 2015; Eriksen et al., 2018), indicated by the inclusion of many different OV's representing different taxa, including prasino-phytes (Prasino), haptophytes (Hapto8 and Hapto67), chloro-phytes (Chloro), cyanobacteria (Cyano) and *Synechococ-*

cus ($N_{\text{synechococcus}}$), cryptophytes (Crypto), picoeukaryotes ($N_{\text{picoeukaryotes}}$), pelagophytes (Pelago), and dinoflagellates (Dino). Overall, the abundance of taxa and the concentrations of biogenic compounds, such as dimethylsulfoniopropionate (DMSP), carbon disulfide (CS_2), and dissolved isoprene (Isoprene_{sea}; Rodríguez-Ros et al., 2020; Rodríguez-Ros et al., 2020), are closely and positively related to TChl *a* and photosynthetic efficiency ($F_V F_M$ and Φ'_{PSII}). Their positive contributions to LV8 activation suggests that phytoplankton and bacterial growth and productivity in the open ocean are triggered by deeper mixed layers. Indeed, the ocean's physical (significant wave height, H_s ; wave period, $T_{m-1,1}$) and dynamical properties (mixed-layer depth, MLD; sea surface height, SSH) are distinctly different in the positive and negative activation of LV8. These OV's suggest that favourable conditions for biological productivity in open-ocean iron-deficient waters correspond to a deepening of the mixed layer, perhaps driven by increased wind (u_{10N}) (Carranza and Gille, 2015) and wave-induced mixing. Although this results in a reduction of median light intensity available within the mixed layer (I_g), it is likely an important mechanism for facilitating mixed-layer entrainment of deep dissolved iron stores (Janssen et al., 2020; Carranza and Gille, 2015) that are otherwise inaccessible at locations away from the influences of landmass and sea ice. Increased salinity (S_{sw}) and an increase in phytoplankton produced detrital material (a_{nap}/a_p ; slope of detrital absorption, $a_{\text{nap slope}}$) with positive activation are additional indicators that the productivity regime depicted by LV8 is focused on the open-ocean areas during ACE, in contrast to LV6, which highlighted the IME.

The strong negative activations of LV8 during leg 2, when the ship was in open waters south of the SACCF, corresponded with the lowest measurements of photosynthetic efficiency ($F_V F_M$ and Φ'_{PSII}), further highlighting the severe iron-limitation that has been documented in waters south of the SACCF.

Interestingly, aerosol sulfate (SO_4^{2-}) was negatively correlated to LV8 and other atmospheric variables, e.g. CO_2 , CH_4 , CO , and O_3 . Its inclusion appears to be driven by enhanced values near the coast of Antarctica, likely due to the availability of atmospheric DMS oxidation products and their conversion to particulate mass in cloud droplets (Schmale et al., 2019). The appearance of the other atmospheric variables is likely coincidental rather than reflecting a causal relationship. LV8 activates positively at lower latitudes, where these trace gases are also more abundant.

In summary, LV8 highlights the microbiological regimes associated with the classical HNLC open-ocean environments in the Southern Ocean and emphasises the importance of water column mixing for accessing deep stores of essential nutrients for stimulating biological growth.

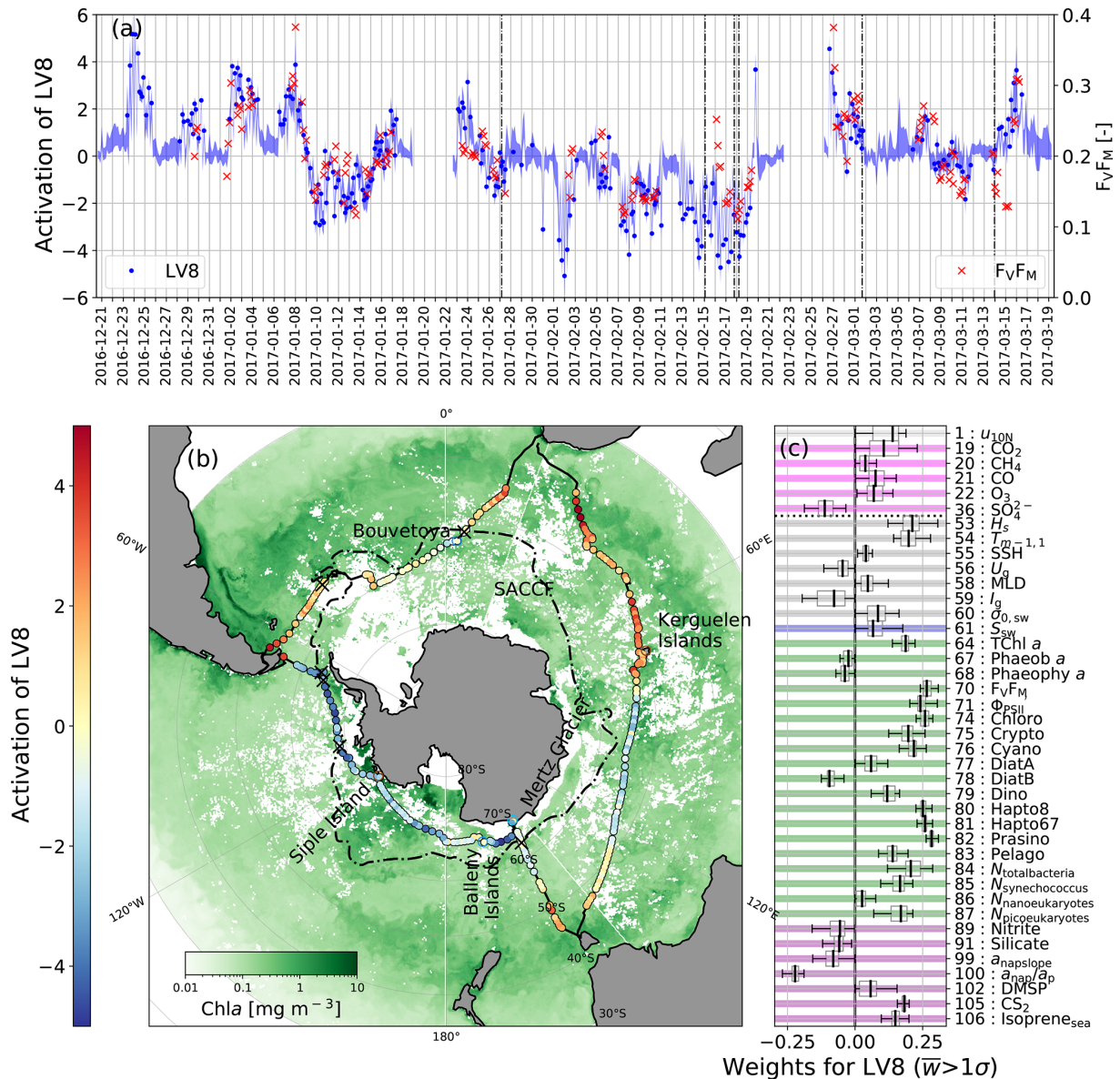


Figure A12. (a) Time series of the activation of LV8 (left axis) and of F_vF_M (right axis). (b) Map of the activation of LV8 and monthly average Chl *a* concentrations (18 December to 16 January for the Indian ocean sector, 17 January to 17 February for the Pacific sector, and 26 February to 21 March for the Atlantic sector). (c) Weights of the OVs contribution to LV8 for which the bootstrap median was larger than 1σ. See the caption of Fig. A1 for details on the oceanic fronts and frontal crossings.

A7 Solar forcing

A7.1 LV7 – Seasonal signal

LV7 decreases steadily throughout the cruise and appears to be driven by the seasonal trends of a number of original variables, including OVs related to incoming solar radiation, some atmospheric and oceanic trace gases, and nutrients in the water. The strongest contributions arise from atmospheric methane (CH₄), ozone (O₃), carbon monoxide (CO), median light intensity in the ocean mixed layer (*I_g*) and atmospheric isoprene (Isoprene_{air}). LV7 explains 3.5 % of the variance.

The decreasing seasonal trend typically observed for CH₄ (Dlugokencky et al., 2019), CO (Petron et al., 2019), and *I_g* over the duration of the cruise (December to March) is mirrored by the overall trend of LV7. Conversely, atmospheric ozone increases over the same timescale (McClure-Begley et al., 2013; Boylan et al., 2015) as captured by the negative weight attributed to O₃. The trends of atmospheric trace gases over the timescales of the ACE cruise are primarily driven by the seasonality of atmospheric photochemistry and primary emissions. Minimum abundances of CH₄ and CO are observed in the late summer and appear to lag 1

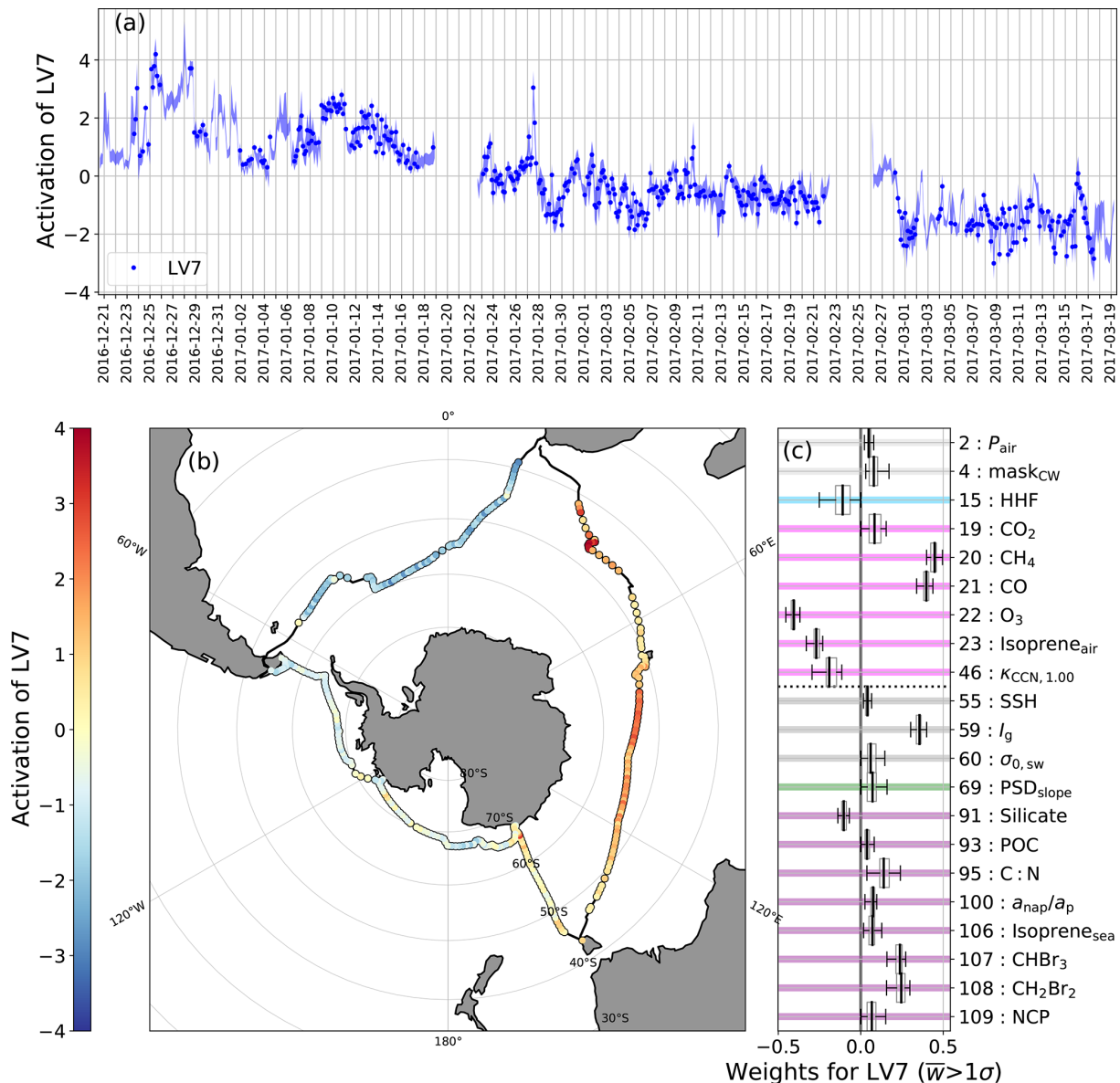


Figure A13. (a) Time series of the activation of LV7. (b) Map of the ship track coloured by the activation of LV7. (c) Box and whisker plots of the activated weights for which the bootstrap median was larger than 1σ .

to 2 months behind the seasonal peak in abundance of the hydroxyl radical (OH), which is the primary sink for both species (Khalil and Rasmussen, 1983, 1990). This lag is attributed to the complex interplay between oxidation reaction rates (driven by OH concentrations and temperature) and seasonality of emissions (e.g. biomass burning peaks in the late winter–early spring in the Southern Hemisphere). CO reaches its minimum during austral summer, as described by Duncan et al. (2003); Té et al. (2016). The seasonal cycle of O_3 is anticorrelated with those of CO and methane primarily as a result of the decreasing photolysis frequency of ozone due to decreasing light intensity (Wilson, 2015).

Isoprene dissolved in the ocean ($\text{Isoprene}_{\text{sea}}$) originating from microbial activity follows the overall decreasing trend of LV7. This is in line with trends of brominated trace gases of biological origin (CH_2Br_2 and CHBr_3), which decrease throughout the season as a result of reduced phytoplankton activity (Stemmler et al., 2015). $\text{Isoprene}_{\text{air}}$ is attributed a negative weight, indicating an increase in the mixing ratio with time, which is in contrast to the trend in $\text{Isoprene}_{\text{sea}}$. One potential explanation for these opposing trends may lie in the balance between isoprene sources and sinks: while marine isoprene emissions decrease throughout the ACE cruise, as they are driven by incoming solar radiation, phytoplankton biomass, and sea surface temperature (Rodríguez-Ros et al.,

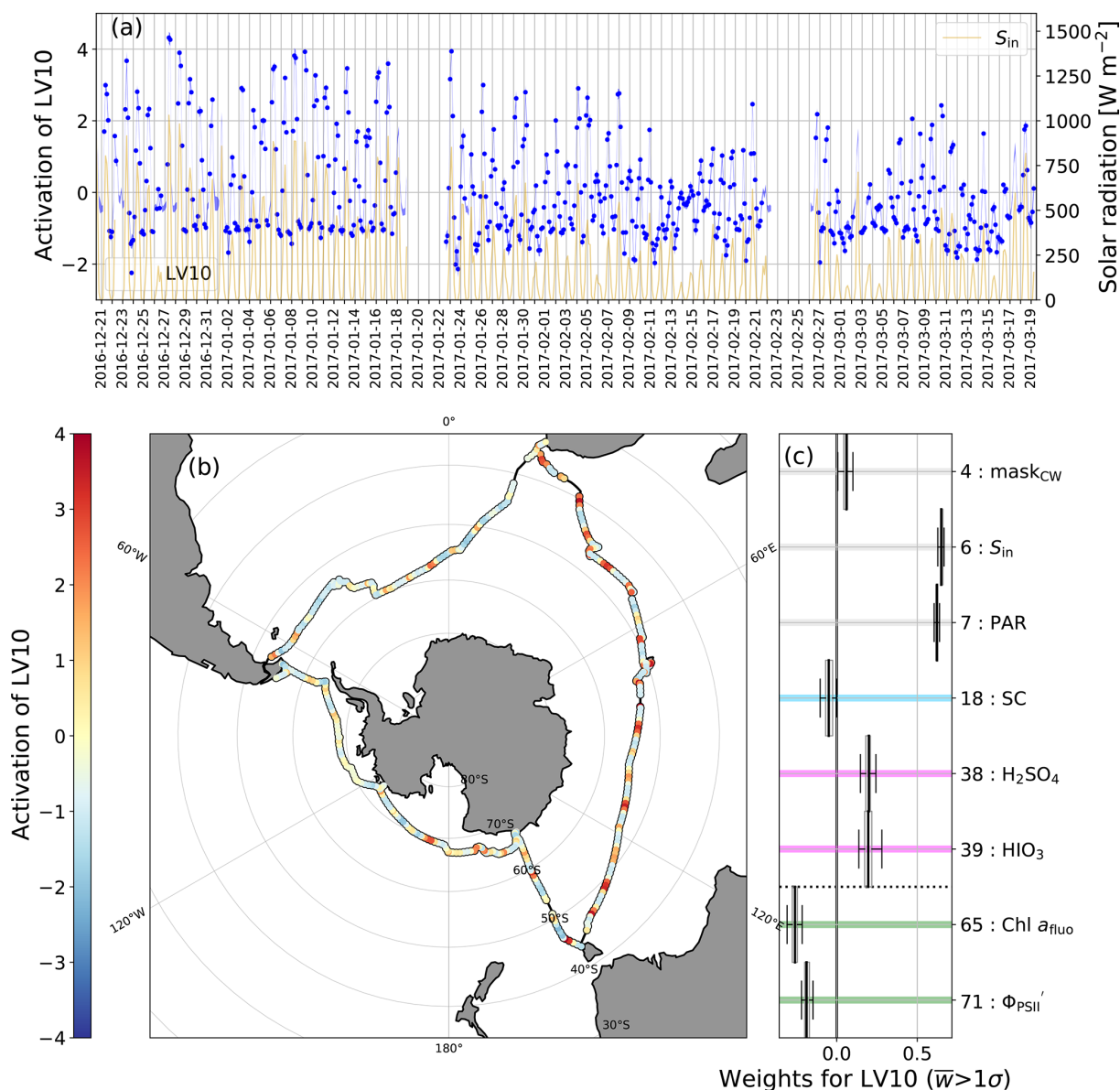


Figure A14. (a) Time series of the activation of LV10 “Diel cycle” (left axis) and of the incoming solar radiation (S_{in} , right axis). (b) Map of the ship track coloured by the activation of LV10. (c) Box and whisker plots of the activated weights for which the bootstrap median was larger than 1σ .

2020), the main sink for atmospheric isoprene (reaction with the OH radical) also decreases, potentially masking the effect of a decreasing marine source. The smaller weight attributed to dissolved isoprene might indicate that its decreasing trend is indeed weaker than that in OH abundance. Increasing mixing ratios at these latitudes over similar timescales have also been observed and modelled for other short-chain hydrocarbons (Pozzer et al., 2010). It is also worth noting that the observed trend in atmospheric isoprene may be influenced by terrestrial sources, as the lifetime of isoprene increases with increasing latitude (e.g. from about 2 h at 40° S to more than 10 h south of 55° S) based on numerical simulations by

Ferracci et al. (2018) and, coupled with high wind speeds, would enable long-range transport of isoprene from land-masses. The entanglement of marine and land sources might also explain why Isoprene_{air} does not occur in LV5 (distance to land) despite the fact that there are known terrestrial sources of isoprene on many of the visited islands and continents.

Trends in the oceanic variables particulate organic carbon (POC), the ratio of POC to particulate organic nitrogen (PON; C : N), and the slope of the marine particle size distribution (2 to $20\mu\text{m}$; PSDslope), which follow the LV activation pattern, i.e. decreasing over time, signal the end

of the productive phytoplankton season. POC and C : N decline to a minimum at the end of the summer season as surface macro- and micro-nutrients are progressively drawn down and exhausted and the available light decreases (Llort et al., 2015). The decline in PSDslope over time indicates that the proportion of smaller and larger particles in the surface ocean have become more equal, representative of seasonal succession in phytoplankton where community taxonomic diversity and size heterogeneity increase after the productive peak time in phytoplankton biomass where the community is generally dominated by a few taxa (Lourey and Trull, 2001; Eriksen et al., 2018). Interestingly, dissolved silicate appears to increase throughout the duration of the ACE cruise, despite documented declines in surface silicate concentration approaching autumn (Freeman et al., 2018). This increase may be due to reduced biological drawdown of silicate, which is controlled by diatom activity or may be due to increased time spent south of the Southern ACC Front in the Pacific and Atlantic sectors, where surface waters are more replete in silicate upwelled from deep waters. Net community production (NCP) also contributes to this seasonal LV with a decreasing trend over time, but it is not captured by the diel cycle LV10, which is likely due to the long integration time of oxygen and hence a lack of a pattern at short timescales.

The sea level pressure at high latitudes in the Southern Hemisphere decreases from December to March (Walland and Simmonds, 1999), which is reflected in the seasonal pattern of LV7. The seasonal decrease in the temperature difference between air and sea surface (mask_{cw}) indicates that the air temperature becomes cooler relative to the sea surface temperature as the summer progresses into autumn. This change of the temperature gradient towards negative values is thought to arise from an increase in cold-air advection during late summer–early autumn, which could stem from either an increase in cyclone frequency (leading to more atmospheric meridional large-scale advection) or an increase in the vertical intrusion of dry-air masses north of 40° S.

The hygroscopicity of CCN activating at a supersaturation of 1.0% ($\kappa_{\text{CCN},1.00}$) increases slightly over time, meaning that atmospheric Aitken mode particles might have changed in composition. Due to the inherent difficulty, the chemical composition of these particles was not measured. Information about the chemical composition would point towards a source of these particles, which in turn would allow for an interpretation. Hence, based on the available data no explanation for the occurrence of this OV in LV7 can be given.

In summary, LV7 confirms our understanding of the seasonal trends of a number of variables, including atmospheric and dissolved trace gases, incoming solar radiation, atmospheric pressure and both oceanic and atmospheric particulate matter. The seasonal behaviour of atmospheric isoprene and dissolved silicate, while initially somewhat counterintuitive, might point at the complex seasonal and marine-terrestrial interactions driving some of the OVs.

A7.2 LV10 – Diel cycle

LV10 describes the diurnal cycle. It peaks during the day and decreases during night following solar radiation, which was measured across visible and UV wavelengths in S_{in} and for photosynthetically active wavelengths only (PAR, 400 to 700 nm), which are the two main contributors to LV10. Moreover, the amplitude of LV10 decreases over the course of the expedition as a result of summer progressing into autumn and the consequent reduction of the amplitude of the daily cycle, which is in line with the reduction of solar radiation reaching the Southern Hemisphere. Active (Φ'_{PSII}) and passive (Chl a_{fluo}) chlorophyll fluorescence respond to the diurnal light cycle predictably, decreasing through the day as irradiance increases (Yentsch and Ryther, 1957; Falkowski and Kolber, 1995), hence the opposite signs of Φ'_{PSII} and Chl a_{fluo} compared to the solar radiation OVs. Under increased irradiance phytoplankton dissipate excess light energy through non-photochemical quenching (Krause and Jahns, 2004; Browning et al., 2014), reducing their passive fluorescence signal and photosynthetic efficiency. The physiological response can remain for hours after the peak irradiance period, resulting in a slight offset in the diurnal cycle to the solar radiation cycle and lower contribution to the LV.

Sulfuric acid and iodic acid (H_2SO_4 and HIO_3) also contribute to LV10, as they are both photochemically produced and have a short lifetime (minutes to hours). In the remote marine boundary layer, sulfuric acid is photochemically produced from DMS oxidation products (i.e. the reaction of SO_2 with OH or the thermal decay of the CH_3SO_3 radical). Observations of the sulfuric acid diurnal cycle have been reported both over the Southern Ocean and on the Antarctic plateau (Lucas and Prinn, 2002; Jefferson et al., 1998). The formation pathway of iodic acid in the atmosphere is still not resolved and observations are scarce (Sipilä et al., 2016; Baccarini et al., 2020; He et al., 2021). However, iodic acid would not form without the iodine radical, which can be produced by photolysis of different precursors (e.g. I_2 or CH_2I_2) (Saiz-Lopez et al., 2012) and explains the contribution of iodic acid to LV10.

Other minor contributors to LV10 are the cold and warm temperature advection mask (mask_{cw}) and the sky cover (SC). The contribution of mask_{cw} in this case does not indicate any large-scale advection but might be the result of a stronger diurnal cycle in the air than in the ocean surface temperature, which can leave a signal of more warm advection during the day than during the night. The contribution of SC has an opposite sign compared to solar irradiance because a higher cloud coverage would decrease the amount of solar radiation that can reach the surface.

In summary, LV10 clearly represents the diurnal cycle driven by solar radiation. OVs such as atmospheric trace gases and marine microbial activity that depend on solar radiation feature strongly in this LV.

A8 Short summary of all latent variables

The sPCA solution describes 55 % of the variability of the 111 OVs with 14 LVs. The largest signal by far originates from the large-scale horizontal temperature and pressure gradients that exist between the low and high latitudes. The effect of these gradients on physical properties of the surface ocean and its activity are mostly captured in the two climatic zone signals (LV1 and LV14). The meridional distribution of the nutrient availability and its effect on the productivity is further highlighted in LV11, LV6, and LV8. The meridional temperature and pressure gradients give rise to the meridional advection of cold and warm air (LV3) with implications on cyclone activity (LV13) and the freshwater cycle with the intermittent character of precipitation events (LV4). The sPCA solution also clearly highlights aerosol sources (especially for INP and fluorescent aerosol) on or in the proximity of islands and continents (LV5) and the positive effect of sea ice on microbial productivity (LV9), as well as the effect that both land and sea ice have on precipitation patterns. We observe a clear link between wind speed and sea state and the concentration of large sea spray aerosol (LV12), tying them to the most wind-driven regions of the Southern Ocean. In contrast to that, the smaller accumulation mode particles (LV2) are ubiquitous because of their long lifetime and various source processes contributing to their abundance. The sPCA successfully decouples the high spatial and temporal variability of iron-limited (LV8) and iron-fertilised blooms (LV6) and their dependence on nutrient availability (LV11), helping to identify the factors responsible for changes to the biogeochemistry and microbial community structure. The method further highlights the effects of diurnal variability of solar forcing on phytoplankton photosynthetic efficiency and trace gas oxidation (LV10) and that of the seasonal variation of the solar forcing on dissolved and atmospheric trace gas concentrations and seasonal cycle in microbial productivity (LV7).

Appendix B: Original variables

This section provides Tables B1 to B8 that list the OVs sorted into the eight categories. Each table provides the original variable IDs, the symbols, the SI units, the full name and a short description of the variable, the input normalisation used for the sPCA analysis (see Sect. 3.4), and a reference to the published dataset or to.

Table B1. Original variables used in this study that fall into the category “Atmospheric dynamics and thermodynamics”. The columns provide the original variable ID, the symbol, the SI units, a short description of the variable, the input normalisation used for the sPCA analysis, and a reference to the published dataset or to Sect. S1 in the Supplement.

OV ID	Symbol	Unit	Description	Norm	Reference
OV1	u_{10N}	m s^{-1}	10 m neutral wind speed derived from the flow-distortion-corrected in situ measurements	linear	10.5281/zenodo.3836439
OV2	P_{air}	hPa	Atmospheric pressure recorded 20 m above sea level	linear	10.5281/zenodo.3379590
OV3	mask_{cyc}	–	Surface cyclone mask	linear	10.5281/zenodo.3974312
OV4	mask_{CW}	–	Cold and warm temperature advection mask	linear	10.5281/zenodo.3989318
OV5	T_{air}	$^{\circ}\text{C}$	Air temperature measured 23.7 m above sea level	linear	10.5281/zenodo.3379590
OV6	S_{in}	W m^{-2}	Solar radiation	linear	10.5281/zenodo.3379590
OV7	PAR	$\mu\text{mol photons m}^{-2} \text{s}^{-1}$	Photosynthetically active radiation (PAR), sky irradiance over PAR wavelengths (400 to 700 nm)	linear	10.5281/zenodo.3859836

Table B2. Original variables used in this study that fall into the category “Atmospheric side of the hydrological cycle”. The columns provide the original variable ID, the symbol, the SI units, a short description of the variable, the input normalisation used for the sPCA analysis, and a reference to the published dataset or to Sect. S1 in the Supplement.

OV ID	Symbol	Unit	Description	Norm	Reference
OV8	RH	%	Relative humidity	linear	10.5281/zenodo.3379590
OV9	w	ppmv	Water vapour mixing ratio	log	10.5281/zenodo.3250790
OV10	$\delta^{18}\text{O}_{\text{vap}}$	‰	$\delta^{18}\text{O}$ of atmospheric water vapour	linear	10.5281/zenodo.3250790
OV11	$\delta^2\text{H}_{\text{vap}}$	‰	$\delta^2\text{H}$ of atmospheric water vapour	linear	10.5281/zenodo.3250790
OV12	$\text{dex}_{\text{c}_{\text{vap}}}$	‰	Deuterium excess of atmospheric water vapour	linear	10.5281/zenodo.3250790
OV13	RR	mm h^{-1}	Rainfall rate at 100 to 200 m a.s.l.	log	10.5281/zenodo.3367284
OV14	SR	mm h^{-1}	Snowfall rate	log	10.5281/zenodo.3367284
OV15	HHF	$\text{m}^2 \text{s}^{-1}$	Horizontal hydrometeor flux	log	10.5281/zenodo.4446616
OV16	visibility	m	Horizontal visibility	log	10.5281/zenodo.3379590
OV17	CL	m	Lowest cloud level estimated with a ceilometer	log	10.5281/zenodo.3379590
OV18	SC	octants	Sky cover at the lowest cloud level	linear	10.5281/zenodo.3379590

Table B3. Original variables used in this study, that fall into the category “Atmospheric chemistry”. The columns provide the original variable ID, the symbol, the SI units, a short description of the variable, the input normalisation used for the sPCA analysis, and a reference to the published dataset or to Sect. S1 in the Supplement.

OV ID	Symbol	Unit	Description	Norm	Reference
OV19	CO ₂	ppm	Dry mixing ratio of carbon dioxide in ambient air	linear	10.5281/zenodo.4028749
OV20	CH ₄	ppm	Dry mixing ratio of methane in ambient air	linear	10.5281/zenodo.4028749
OV21	CO	ppm	Mixing ratio of carbon monoxide in ambient air	linear	10.5281/zenodo.4028749
OV22	O ₃	ppb	Mixing ratio of ozone in ambient air	linear	10.5281/zenodo.2636779
OV23	Isoprene _{air}	ppb	Mixing ratio of isoprene in ambient air	log	See Supplement for details
OV24	N_{Aitken}	cm ⁻³	Particle number concentration in the Aitken mode	log	See Supplement for details
OV25	$N_{\text{accumulation}}$	cm ⁻³	Particle number concentration in the accumulation mode	log	See Supplement for details
OV26	N_{seaspray}	cm ⁻³	Particle number concentration in the sea spray mode	log	See Supplement for details
OV27	$N_{\text{oxalate,PM}_{10}}$	µg m ⁻³	Mass concentration of oxalate in PM ₁₀ dry aerosol particles from offline high-volume filter sampling	log	10.5281/zenodo.3922147
OV28	$N_{\text{bromide,PM}_{10}}$	µg m ⁻³	Mass concentration of bromide in PM ₁₀ dry aerosol particles from offline high-volume filter sampling	log	10.5281/zenodo.3922147
OV29	$N_{\text{MSA,PM}_{10}}$	µg m ⁻³	Mass concentration of MSA in PM ₁₀ dry aerosol particles from offline high-volume filter sampling	log	10.5281/zenodo.3922147
OV30	$N_{\text{sodium,PM}_{10}}$	µg m ⁻³	Mass concentration of sodium in PM ₁₀ dry aerosol particles from offline high-volume filter sampling	log	10.5281/zenodo.3922147
OV31	$N_{\text{ammonium,PM}_{10}}$	µg m ⁻³	Mass concentration of ammonium in PM ₁₀ dry aerosol particles from offline high-volume filter sampling	log	10.5281/zenodo.3922147
OV32	$N_{\text{potassium,PM}_{10}}$	µg m ⁻³	Mass concentration of potassium in PM ₁₀ dry aerosol particles from offline high-volume filter sampling	log	10.5281/zenodo.3922147
OV33	$N_{\text{magnesium,PM}_{10}}$	µg m ⁻³	Mass concentration of magnesium in PM ₁₀ dry aerosol particles from offline high-volume filter sampling	log	10.5281/zenodo.3922147
OV34	$N_{\text{calcium,PM}_{10}}$	µg m ⁻³	Mass concentration of calcium in PM ₁₀ dry aerosol particles from offline high-volume filter sampling	log	10.5281/zenodo.3922147
OV35	$N_{\text{nitrate,PM}_{10}}$	µg m ⁻³	Mass concentration of nitrate in PM ₁₀ dry aerosol particles from offline high-volume filter sampling	log	10.5281/zenodo.3922147
OV36	SO ₄ ²⁻	µg m ⁻³	Mass concentration of sulfate in non-refractory particulate matter (PM1)	log	10.5281/zenodo.3559982

Table B3. Continued.

OV ID	Symbol	Unit	Description	Norm	Reference
OV37	Cl ⁻	µg m ⁻³	Mass concentration of chloride in non-refractory particulate matter (PM1) (incomplete since chloride is refractory)	log	10.5281/zenodo.3559982
OV38	H ₂ SO ₄	molec. cm ⁻³	Concentration of gaseous sulfuric acid	log	10.5281/zenodo.3265832
OV39	HIO ₃	molec. cm ⁻³	Concentration of gaseous iodic acid	log	See Supplement for details
OV40	MSA	molec. cm ⁻³	Concentration of gaseous methanesulfonic acid	log	10.5281/zenodo.2636771
OV41	<i>N</i> _{CCN,0.15}	cm ⁻³	Particle number concentration acting as CCN at 0.15 % supersaturation	log	10.5281/zenodo.4415495
OV42	<i>N</i> _{CCN,0.30}	cm ⁻³	Particle number concentration acting as CCN at 0.3 % supersaturation	log	10.5281/zenodo.4415495
OV43	<i>N</i> _{CCN,1.00}	cm ⁻³	Particle number concentration acting as CCN at 1.0 % supersaturation	log	10.5281/zenodo.4415495
OV44	<i>κ</i> _{CCN,0.15}	–	Hygroscopicity parameter of particles acting as CCN at 0.15 % supersaturation	log	10.5281/zenodo.4415495
OV45	<i>κ</i> _{CCN,0.30}	–	Hygroscopicity parameter of particles acting as CCN at 0.5 % supersaturation	log	10.5281/zenodo.4415495
OV46	<i>κ</i> _{CCN,1.00}	–	Hygroscopicity parameter of particles acting as CCN at 1.0 % supersaturation	log	10.5281/zenodo.4415495
OV47	<i>N</i> _{INP,LV,-8}	dm ⁻³	INP number concentration at –8 °C from offline low-volume PM ₁₀ filter sampling	log	10.5281/zenodo.4311665
OV48	<i>N</i> _{INP,LV,-20}	dm ⁻³	INP number concentration at –20 °C from offline low-volume PM ₁₀ filter sampling	log	10.5281/zenodo.4311665
OV49	<i>N</i> _{INP,HV,-8}	dm ⁻³	INP number concentration at –8 °C from offline high-volume PM ₁₀ filter sampling	log	See Supplement for details
OV50	<i>N</i> _{INP,HV,-20}	dm ⁻³	INP number concentration at –20 °C from offline high-volume PM ₁₀ filter sampling	log	See Supplement for details
OV51	<i>r</i> _{fluo,fine3σ}	–	Ratio of fluorescent to total aerosol particles (for particles with optical diameter smaller than 1 µm)	log	See Supplement for details
OV52	<i>r</i> _{fluo,coarse3σ}	–	Ratio of fluorescent to total aerosol particles (for particles with optical diameter greater than 1 µm)	log	See Supplement for details

Table B4. Original variables used in this study that fall into the category “Oceanic dynamics and thermodynamics”. The columns provide the original variable ID, the symbol, the SI units, a short description of the variable, the input normalisation used for the sPCA analysis, and a reference to the published dataset or to Sect. S1 in the Supplement.

OV ID	Symbol	Unit	Description	Norm	Reference
OV53	<i>H</i> _s	m	Significant wave height	log	10.5281/zenodo.4541564
OV54	<i>T</i> _{<i>m</i>-1,1}	s	Spectral mean wave energy period	log	10.5281/zenodo.4541564
OV55	SSH	m	Sea surface height (satellite absolute dynamic topography)	linear	10.5281/zenodo.3660852
OV56	<i>U</i> _g	ms ⁻¹	Surface ocean geostrophic velocity (satellite)	log	10.5281/zenodo.3660852
OV57	<i>T</i> _{sw}	°C	Surface ocean temperature of seawater	linear	10.5281/zenodo.3660852
OV58	MLD	m	Surface ocean mixed layer depth	linear	10.5281/zenodo.3836648
OV59	<i>I</i> _g	µmol photons m ² s ⁻¹	Median light level over 24 h within the surface ocean mixed layer	log	10.5281/zenodo.3859836
OV60	<i>σ</i> _{0,sw}	kg m ⁻³	Surface ocean potential density anomaly of seawater	linear	10.5281/zenodo.3660852

Table B5. Original variables used in this study that fall into the category “Oceanic side of the hydrological cycle”. The columns provide the original variable ID, the symbol, the SI units, a short description of the variable, the input normalisation used for the sPCA analysis, and a reference to the published dataset or to Sect. S1 in the Supplement

OV ID	Symbol	Unit	Description	Norm	Reference
OV61	S_{sw}	PSU	Surface ocean salinity of seawater	linear	10.5281/zenodo.3660852
OV62	C_i	–	Sea ice concentration (satellite)	linear	10.5281/zenodo.3660852
OV63	$\delta^{18}O_{sw}$	‰	Surface ocean $\delta^{18}O$ of seawater	linear	10.5281/zenodo.1494915

Table B6. Original variables used in this study that fall into the category “Ocean microbial community”. The columns provide the original variable ID, the symbol, the SI units, a short description of the variable, the input normalisation used for the sPCA analysis, and a reference to the published dataset or to Sect. S1 in the Supplement.

OV ID	Symbol	Unit	Description	Norm	Reference
OV64	TChl <i>a</i>	mg m ⁻³	Total chlorophyll <i>a</i> concentration derived from high-performance liquid chromatography and particulate absorption line height	log	10.5281/zenodo.3816726
OV65	Chl <i>a</i> _{fluo}	µg l ⁻¹	In vivo fluorescence of chlorophyll <i>a</i>	log	See Supplement for details
OV66	Chlide <i>a</i>	mg m ⁻³	Chlorophyllide <i>a</i> pigment concentration	log	10.5281/zenodo.3816726
OV67	Phaeob <i>a</i>	mg m ⁻³	Pheophorbide <i>a</i> pigment concentration	log	10.5281/zenodo.3816726
OV68	Phaeophy <i>a</i>	mg m ⁻³	Pheophytin <i>a</i> pigment concentration	log	10.5281/zenodo.3816726
OV69	PSD _{slope}	–	Slope of the particle size distribution 2–60 µm	linear	See Supplement for details
OV70	FvF _M	–	Photochemical efficiency of photosystem II measured during the night	linear	See Supplement for details
OV71	Φ _{PSII} '	–	Photochemical efficiency of photosystem II during the day	linear	See Supplement for details
OV72	σ _{PSII}	Å ² RCII ⁻¹	Functional absorption cross section of PSII during the night	linear	See Supplement for details
OV73	σ _{PSII} '	Å ² RCII ⁻¹	Functional absorption cross section of PSII during the day	linear	See Supplement for details
OV74	Chloro	mg m ⁻³	Chlorophyte contribution to chlorophyll biomass	log	10.5281/zenodo.3816726
OV75	Crypto	mg m ⁻³	Cryptophyte contribution to chlorophyll biomass	log	10.5281/zenodo.3816726
OV76	Cyano	mg m ⁻³	Cyanobacteria type 2 contribution to chlorophyll biomass	log	10.5281/zenodo.3816726
OV77	DiatA	mg m ⁻³	Diatom type 1 contribution to chlorophyll biomass	log	10.5281/zenodo.3816726
OV78	DiatB	mg m ⁻³	Diatom type 2 contribution to chlorophyll biomass	log	10.5281/zenodo.3816726
OV79	Dino	mg m ⁻³	Dinoflagellate type 1 contribution to chlorophyll biomass	log	10.5281/zenodo.3816726
OV80	Hapto8	mg m ⁻³	Haptophyte type 8 contribution to chlorophyll biomass	log	10.5281/zenodo.3816726
OV81	Hapto67	mg m ⁻³	Haptophyte type 6&7 contribution to chlorophyll biomass	log	10.5281/zenodo.3816726

Table B6. Continued.

OV ID	Symbol	Unit	Description	Norm	Reference
OV82	Prasino	mg m^{-3}	Prasinophyte type 3 contribution to chlorophyll biomass	log	10.5281/zenodo.3816726
OV83	Pelago	mg m^{-3}	Pelagophyte contribution to chlorophyll biomass	log	10.5281/zenodo.3816726
OV84	$N_{\text{totalbacteria}}$	cells ml^{-1}	Abundance of phototrophic prokaryotes, (mainly free living bacteria)	log	See Supplement for details
OV85	$N_{\text{synechococcus}}$	cells ml^{-1}	Abundance of <i>Synechococcus</i>	log	See Supplement for details
OV86	$N_{\text{nanoeukaryotes}}$	cells ml^{-1}	Abundance of nanophytoplankton (roughly 3–10 μm size)	log	See Supplement for details
OV87	$N_{\text{picoeukaryotes}}$	cells ml^{-1}	Abundance of eukaryotic picophytoplankton ($\lesssim 3 \mu\text{m}$ size)	log	See Supplement for details

Table B7. Original variables used in this study that fall into the category “Ocean biogeochemistry”. The columns provide the original variable ID, the symbol, the SI units, a short description of the variable, the input normalisation used for the sPCA analysis, and a reference to the published dataset or to Sect. S1 in the Supplement.

OV ID	Symbol	Unit	Description	Norm	Reference
OV88	Nitrate	μM	Dissolved nitrate (NO_3^-) concentration	log	10.5281/zenodo.3903134
OV89	Nitrite	μM	Dissolved nitrite (NO_2^-) concentration	log	10.5281/zenodo.3903134
OV90	Phosphate	μM	Dissolved phosphate (PO_4^{3-}) concentration	log	10.5281/zenodo.3903134
OV91	Silicate	μM	Dissolved silicate ($\text{Si}(\text{OH})_4$) concentration	log	10.5281/zenodo.3903134
OV92	Ammonium	μM	Dissolved ammonium (NH_4^+) concentration	log	10.5281/zenodo.3751143
OV93	POC	μM	Particulate organic carbon concentration	log	10.5281/zenodo.3859515
OV94	PON	μM	Particulate organic nitrogen concentration	log	10.5281/zenodo.3859515
OV95	C : N	–	Particulate organic carbon to nitrogen ratio	log	10.5281/zenodo.3859515
OV96	TEP	$\mu\text{g XGeq L}^{-1}$	Concentration of transparent exopolymeric particles	log	See Supplement for details
OV97	CSP	$\mu\text{g BS Aeq L}^{-1}$	Concentration of Coomassie stainable particles	log	See Supplement for details
OV98	a_{CDOM}	m^{-1}	Absorption due to coloured dissolved organic matter at 350 nm	log	See Supplement for details
OV99	$a_{\text{nap slope}}$	nm^{-1}	Spectral slope of detrital absorption from 380 to 700 nm (reference wavelength 380 nm)	linear	See Supplement for details
OV100	$a_{\text{nap}}/a_{\text{p}}$	–	Ratio of detrital absorption relative to total particulate absorption at 440 nm	linear	See Supplement for details
OV101	acrylate	nM	Concentration of acrylate	log	See Supplement for details
OV102	DMSP	nM	Concentration of total (dissolved + particulate) dimethylsulfoniopropionate	log	See Supplement for details
OV103	DMS	nM	Concentration of dimethyl sulfide	log	See Supplement for details
OV104	CSO	pM	Concentration of carbonyl sulfide	log	See Supplement for details
OV105	CS_2	pM	Concentration of carbon disulfide	log	See Supplement for details
OV106	Isoprene _{sea}	pM	Concentration of isoprene (C_5H_8)	log	See Supplement for details
OV107	CHBr_3	pM	Concentration of tribromomethane (bromo-form)	log	See Supplement for details
OV108	CH_2Br_2	pM	Concentration of dibromomethane	log	See Supplement for details
OV109	NCP	$\text{Mmol O}_2 \text{ m}^{-2} \text{ d}^{-1}$	Net community production (O_2/Ar based)	linear	10.5281/zenodo.3979091

Table B8. Original variables used in this study that fall into the category “Topography”. The columns provide the original variable ID, the symbol, the SI units, a short description of the variable, the input normalisation used for the sPCA analysis, and a reference to the published dataset or to Sect. S1 in the Supplement.

OV ID	Symbol	Unit	Description	Norm	Reference
OV110	d_{land}	m	Distance to the nearest shore line in metres	log	10.5281/zenodo.3832045
OV111	d_{water}	m	Water depth calculated from the General Bathymetric Chart of the Oceans	log	10.5281/zenodo.3773102

Appendix C: Correlation between the latent variable time series

Figure C1a shows the correlation matrix between the LV times series. Figure C1b shows the p value for each correlation for pairs of LV. Shades of blue highlight LV pairs showing a level of correlation significant with a p value < 0.05 . The darker the blue, the more significant the correlation. Conversely, yellow to red cells correspond to non-significant correlations. The darker the red, the less significant the correlation. The permutation test is computed by taking pairs of LV and computing a correlation value. Following this, the first LV is shuffled randomly and a correlation value is computed 10 000 times. The p value is the fraction of times that the random correlation is larger than the correlation between actual non-shuffled LVs. Note the high correlation between LV1 and LV14 ($R = 0.74$) with a p value of 0.0002.

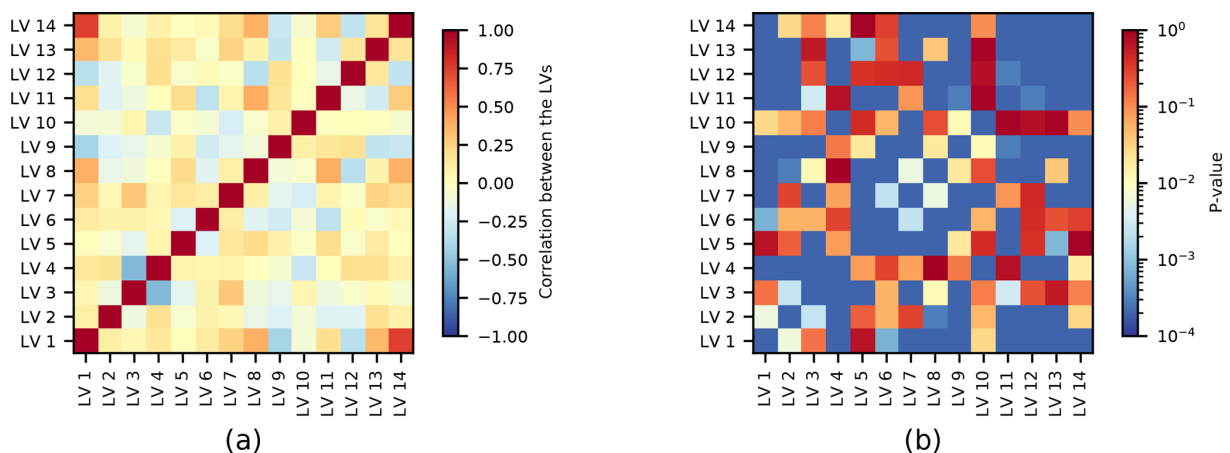


Figure C1. (a) Correlation between the LV time series and (b) the corresponding p value of a two-sample permutation test with 10 000 permutations.

Appendix D: Replacement of low values

Zero value observations would be lost when a log transformation is applied to the lognormal distributed OV time series. In addition, the log transformation puts larger weight on small variations, which may not necessarily reflect real variability if they are below the instrument's detection limit. For this reason we choose to replace low values in some of the OV series prior to applying the log transformation. Table D1 lists the OVs for which this was the case and provides the values that were chosen for the replacement of low values and the fraction of replaced data. The replacement for low values were chosen based on the instrument's limit of detection or based on the judgement of the data experts. Large fractions of data are replaced for the precipitation time series RR and SR due to the large fraction of observations without precipitation. In addition, a relatively large fraction of the ice nucleation particle number concentration measurements (N_{INP}) and some of the contributions to the chlorophyll biomass derived by the CHEMTAX analysis were below the respective detection limits. For the remaining OVs in Table D1, only a small fraction of data points (i.e. < 5 %) in each time series were replaced with the replacement values.

Table D1. Original variables used in this study to which a replacement was applied due to low values. The columns provide the original variable ID, the symbol, the SI units, the replacement for low values, and the fraction of replaced data.

OV ID	Symbol	Unit	Replacement for low values	Data fraction replaced
OV13	RR	mm h ⁻¹	1.00×10^{-2}	0.639
OV14	SR	mm h ⁻¹	1.00×10^{-2}	0.876
OV15	HHF	m ² s ⁻¹	3.50×10^1	0.056
OV36	SO ₄ ²⁻	μg m ⁻³	1.40×10^{-1}	0.015
OV37	Cl ⁻	μg m ⁻³	3.20×10^{-2}	0.004
OV47	$N_{\text{INP,LV,-8}}$	dm ⁻³	8.00×10^{-4}	0.882
OV48	$N_{\text{INP,LV,-20}}$	dm ⁻³	1.15×10^{-1}	0.599
OV49	$N_{\text{INP,HV,-8}}$	dm ⁻³	1.89×10^{-4}	0.403
OV50	$N_{\text{INP,HV,-20}}$	dm ⁻³	2.76×10^{-2}	0.299
OV53	H_s	m	3.00×10^{-1}	0.007
OV56	U_g	m s ⁻¹	1.00×10^{-2}	0.018
OV74	Chloro	mg m ⁻³	1.00×10^{-5}	0.412
OV75	Crypto	mg m ⁻³	1.00×10^{-5}	0.264
OV76	Cyano	mg m ⁻³	1.00×10^{-5}	0.389
OV77	DiatA	mg m ⁻³	1.00×10^{-5}	0.097
OV78	DiatB	mg m ⁻³	1.00×10^{-5}	0.125
OV79	Dino	mg m ⁻³	1.00×10^{-5}	0.060
OV80	Hapto8	mg m ⁻³	1.00×10^{-5}	0.065
OV82	Prasino	mg m ⁻³	1.00×10^{-5}	0.352
OV83	Pelago	mg m ⁻³	1.00×10^{-5}	0.093
OV92	Ammonium	μm	2.00×10^{-2}	0.006
OV96	TEP	μg XGeq L ⁻¹	5.00×10^0	0.024
OV104	CSO	pM	1.00×10^0	0.016
OV110	d_{land}	m	1.00×10^2	0.005
OV111	d_{water}	m	2.00×10^1	0.040

Appendix E: Sparse PCA results for different time resolutions

The sPCA analysis requires all OV_s to be resampled to the same temporal resolution. Choosing a resolution that is too high will result in large differences in the sparsity of the OV time series, and OV_s that are sampled at low resolution will likely not contribute to the sPCA solution. Conversely, resampling all variables to a low temporal resolution will result in a loss of information about small-scale variability. The optimal choice of the averaging time depends on the dataset and on the research questions. Figure E1 shows the correlation between the weight vectors obtained from sparse PCA decompositions of the 180 and 720 min time resolutions. Figure E2 shows the corresponding correlation of the time series. Here we label LVs from the 720 min time resolution run with lower-case letters (i.e. lv1 instead of LV1).

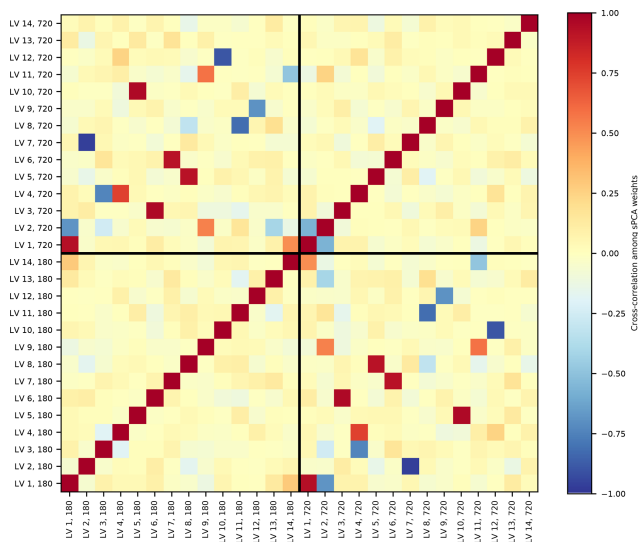


Figure E1. Correlation between the weight vectors obtained from sPCA decompositions of the 180 and 720 min time resolutions.

For both time resolutions, the climatic zones and large-scale horizontal gradients (LV1) provide the largest signal. The drivers of CCN population signal (LV2) explains relatively less variance in the 720 min where it corresponds to lv7. The signals of meridional cold and warm air advection (LV3) and precipitation (LV4), which both showed relatively large correlation in their time series, both correlate with lv4. The signals of the ship's distance to land (LV5), the iron-fertilised and iron-limited biological productivity (LV6 and LV8), the seasonal signal (LV7), the diel cycle (LV10), the surface nutrient concentration associated with mixing events, climatic and frontal zones (LV11), and the wind-driven conditions and sea spray aerosol (LV12) find very similar resemblance in the sPCA solution found for the 720 min resolution. On the other hand, the LVs describing the marginal sea ice zone and snowfall (LV9), the extratropical cyclone activ-

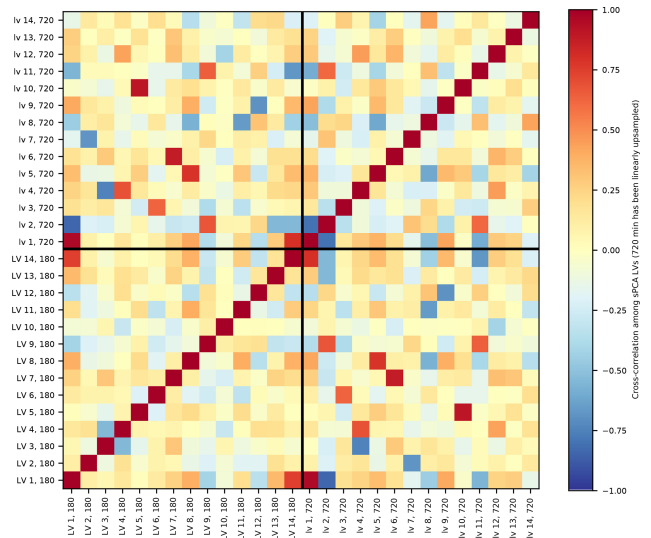


Figure E2. Correlation between the LV time series obtained from sPCA decompositions of the 180 and 720 min time resolutions.

ity (LV13), and the climatic zones with local high-latitude hotspots (LV14) appear to be somewhat redistributed in the 720 min sPCA, as can be seen by the weaker correlation to more than one of the lvs.

Appendix F: Variable glossary

OV1: 10 m neutral wind speed (u_{10N}).

The 10 m neutral wind speed is a standardised form to report the wind speed that would be measured under the given wind forcing at 10 m height and neutral atmospheric stability and provides a proxy for the wind forcing at the ocean surface and can be directly related to the surface friction velocity via the surface drag coefficient. The 10 m neutral wind speed is calculated from in situ wind speed measurements at a given measurement height under the assumption of a near-logarithmic height profile using bulk flux formula and an empirical relation for the wind speed dependence of the neutral drag coefficient.

OV2: atmospheric pressure (P_{air}).

Atmospheric pressure was measured at a height of approximately 20 m above sea level.

OV3: surface cyclone mask (mask_{cyc}).

The surface cyclone mask denotes time periods when a surface cyclone passes the ACE ship track. More specifically, if the ship track lies within a surface cyclone, which is defined by the outermost closed sea level pressure contour around a pressure minimum (see Sect. S1.2), the cyclone mask is active (1 in mask). During the passage of an extratropical cyclone, enhanced wind speed and high variability in surface pressure, air temperature, specific humidity, and

precipitation is expected. The actual environmental changes due to the passage of an extratropical cyclone depends on the measurement position relative to the cyclone centre and the cyclone's fronts.

OV4: cold and warm temperature advection mask (mask_{CW}). The cold and warm temperature advection mask denotes time periods of differences between the near-surface air temperature and the sea surface temperature. An air–sea temperature difference larger than 0°C (i.e. the atmosphere is warmer than the ocean surface) is defined as warm temperature advection (1 in mask), a difference smaller than 0°C as cold temperature advection (-1 in mask). The cold and warm temperature advection mask is an indicator of surface sensible and latent heat fluxes and is strongly influenced by the passage of extratropical cyclones, which lead to the large-scale advection of air masses. Furthermore, strong horizontal gradients in sea surface temperature, for example across oceanic fronts, lead to locally large air–sea temperature differences.

OV5: air temperature (T_{air}).

Air temperature was measured at approximately 24 m above sea level using a Vaisala MAWS420 meteorological station (sensor model QMH102).

OV6: solar radiation (S_{in}).

Solar radiation was measured at approximately 24 m above sea level.

OV7: photosynthetically active radiation (PAR).

Photosynthetically active radiation or sky irradiance over photosynthetically active wavelengths (400 to 700 nm; $\mu\text{mol photons m}^{-2}\text{s}^{-1}$) is an instantaneous measurement of the visible irradiance from the sun made above the surface of the ocean. It provides an estimate of the flux of visible light delivered to the surface ocean that is utilised by photosynthetic organisms, namely phytoplankton, as an energy source for their photosynthesis. Excess light in the visible range can also be harmful to photosynthetic organisms, inhibiting their photosynthesis for hours after exposure and has been linked to the production of secondary metabolites and trace gases by these organisms.

OV8: relative humidity (RH).

Relative humidity was measured at approximately 24 m above sea level using a Vaisala MAWS240 meteorological station (sensor model QMH102) and represents the humidity saturation of the atmosphere relative to the saturation vapour pressure. The relative humidity depends on the air temperature and the atmospheric pressure.

OV9: water vapour mixing ratio (w).

The water vapour mixing ratio w is the water vapour volume relative to the dry-air volume given in part per million

volume (ppmv) and is a measure of humidity in the air. w was measured using a cavity ring-down laser spectrometer and was calibrated with a dew point generator.

OV10: $\delta^{18}\text{O}$ of atmospheric water vapour ($\delta^{18}\text{O}_{\text{vap}}$).

$\delta^{18}\text{O}_{\text{vap}}$ gives the abundance of the heavy water molecule H_2^{18}O relative to the light water molecule H_2^{16}O in atmospheric water vapour and can be used as a tracer of phase change processes in the atmosphere. Various processes, e.g. ocean evaporation, the large-scale advection of air masses or vertical mixing of air masses influence the temporal and spatial variability of $\delta^{18}\text{O}_{\text{vap}}$.

OV11: $\delta^2\text{H}$ of atmospheric water vapour ($\delta^2\text{H}_{\text{vap}}$).

$\delta^2\text{H}_{\text{vap}}$ gives the abundance of the heavy water molecule $^1\text{H}^2\text{H}^{16}\text{O}$ relative to the light water molecule $^1\text{H}_2^{16}\text{O}$ in atmospheric water vapour and can be used as a tracer of phase change processes in the atmosphere. Various processes, e.g. ocean evaporation, the large-scale advection of air masses, or vertical mixing of air masses influence the temporal and spatial variability of $\delta^2\text{H}_{\text{vap}}$.

OV12: deuterium excess of atmospheric water vapour ($d_{\text{exc}_{\text{vap}}}$).

The second-order isotope variable deuterium excess is defined as $d_{\text{vap}} = \delta^2\text{H}_{\text{vap}} - 8 \cdot \delta^{18}\text{O}_{\text{vap}}$ and is often used as a measure of non-equilibrium processes in the atmospheric branch of the water cycle. For example, during ocean evaporation, d_{vap} increases in the atmospheric water vapour due to the diffusion of water vapour away from the ocean surface.

OV13: rainfall rate (RR).

The rainfall rate is derived from the 100 to 200 m a.s.l. bin of measurements using a micro-rain radar (MRR2, manufactured by Metek) using Metek software.

OV14: snowfall rate (SR).

The snowfall rate (SR) is estimated from radar effective reflectivity (Z) at 400 m a.s.l. height derived from a vertically profiling Doppler radar using the algorithm by Maahn and Kollias (2012) for snowfall. The Z – S relationship from Grazioli et al. (2017) was used. Influence of microphysical snow properties was considered less important for sPCA analysis compared to the variability due to snowfall rate.

OV15: horizontal hydrometeor flux (HHF).

Horizontal hydrometeor flux (HHF, $\text{m}^{-2}\text{s}^{-1}$) is the total flux of particles with sizes between 0.036 to 2 mm derived from snow particle counter (SPC; manufactured by Niigata) measurements and wind speed measurements (starboard anemometer). HHF includes (1) snowfall and blowing snow during snowfall, (2) drifting and blowing snow lifted from the ground (snow on sea ice, snow from the ice sheet when the ship was in vicinity), (3) rain drops, and (4) possible sea

spray.

OV16: horizontal visibility (visibility).

Horizontal visibility is defined as the “maximum distance at which an observer can see and identify an object lying close to the horizontal plane on which he or she is standing” (AMS glossary). During ACE, horizontal visibility (or meteorological optical range, from 10 m to 20 km) is derived from Vaisala’s MAWS Present Weather Detector (PWD22) measurements of the extinction in forward scattering by small particles suspended in the air (fog droplets, haze, smoke) and larger particles (rain drops, drizzle, snowflakes, ice grains, etc.).

OV17: lowest cloud level (CL).

The height of the lowest cloud level derived from ceilometer (CL31, pulsed diode laser lidar) attenuated backscatter profile. Vaisala’s CL31 provides information about up to three cloud layers, and here the lowest is taken.

OV18: sky cover at the lowest cloud level (SC).

Sky cover at the lowest cloud level is cloud amount of the lowest cloud layers at the corresponding layer height derived from the time series of ceilometer data by Vaisala CL31 Sky condition algorithm.

OV19: dry-air mixing ratio of carbon dioxide (CO₂).

Carbon dioxide (CO₂) dry mixing ratio in ambient air, reported in parts per million. CO₂ is a long-lived trace gas that disperses globally and is mainly produced by fossil fuel combustion. The Southern Ocean in summer is thought to be a net CO₂ sink. Data were cleaned from the influence of pollution using the same methodology applied to aerosol measurements.

OV20: dry-air mixing ratio of methane (CH₄).

Methane (CH₄) dry mixing ratio in ambient air, reported in parts per million. CH₄ is a long-lived trace gas which disperses globally and can be produced by a variety of different sources (e.g. wetlands, agriculture, biomass burning). The Southern Ocean is thought to be a net CH₄ sink. Data were cleaned from the influence of pollution using the same methodology applied to aerosol measurements.

OV21: air mixing ratio of carbon monoxide (CO).

Carbon monoxide (CO) mixing ratio in ambient air, reported in parts per billion. CO has a lifetime of few weeks to months and is produced by combustion processes and oxidation of other hydrocarbons (e.g. methane). The main sink for CO is reaction with the hydroxyl radical. Data were cleaned from the influence of pollution using the same methodology applied to aerosol measurements.

OV22: dry-air mixing ratio of ozone (O₃).

Ozone (O₃) mixing ratio in ambient air, reported in parts per

billion. Ozone is a reactive oxidant gas, it is photochemically produced from the oxidation of CO, CH₄, and other volatile organic compounds in the presence of NO_x. The remote marine boundary layer is a net sink for ozone, which is removed by photolysis and dry deposition to the ocean surface. Data were cleaned from the influence of pollution using the same methodology applied to aerosol measurements.

OV23: isoprene (Isoprene_{air}).

Molar fraction of isoprene or 2-methyl-1,3-butadiene (C₅H₈) in ambient air (reported in nmol of isoprene per mole of air, ppb).

OV24: number concentrations of Aitken mode particles (N_{Aitken}).

The number concentration of aerosol particles in the Aitken size distribution mode (N_{Aitken}) was derived from aerosol number size distributions measured with a scanning mobility particle sizer (SMPS) and aerodynamic particle sizer (APS) using the procedure following Modini et al. (2015). Co-located, 15 min median size distributions measured by the SMPS and APS were first joined together by interpolating the measurements to a common diameter scale represented in terms of geometric particle diameter. Electrical mobility diameters measured by the SMPS were simply assumed to represent geometric particle diameters (i.e. shape effects were neglected), and aerodynamic diameters measured by the APS were converted to geometric particle diameters by dividing by the square root of particle effective density. A constant particle effective density of 1.9 g cm⁻³ was assumed for all distributions. Following this, a sequential lognormal mode-fitting procedure was applied to the joined size distributions. A “sea spray” size distribution was first fitted to the upper portions of the joined size distributions (as described below for N_{seaspray}). Residual size distributions were then obtained by subtracting the fitted sea spray modes from the joined size distributions. Bi-lognormal functions were then fitted to the residual size distributions to represent the combined Aitken and accumulation size distribution modes. A total of 84 % of all joined size distributions were successfully fit with this procedure and retained for further analysis, where success was defined as having a mean absolute error (between the residual and fitted distributions) divided by total integrated particle concentration of less than 15 %. The fitted Aitken modes were constrained to have modal diameters between 10 and 100 nm and geometric standard deviations between 1.2 and 1.8. N_{Aitken} represents the integrated number concentrations in the fitted Aitken modes.

OV25: Number concentrations of accumulation mode particles (N_{accumulation}).

The number concentration of aerosol particles in the accumulation size distribution mode (N_{Accumulation}) was derived from aerosol number size distributions measured with a

scanning mobility particle sizer (SMPS) and aerodynamic particle sizer (APS) using the procedure following Modini et al. (2015). Co-located, 15 min median size distributions measured by the SMPS and APS were first joined together by interpolating the measurements to a common diameter scale represented in terms of geometric particle diameter, before a sequential lognormal mode-fitting procedure was applied to the joined size distributions, as described above for N_{Aitken} . The fitted accumulation modes were constrained to have modal diameters between 90 and 200 nm and geometric standard deviations between 1.2 and 1.8. $N_{\text{Accumulation}}$ represents the integrated number concentrations in the fitted accumulation modes.

OV26: number concentrations of sea spray mode particles (N_{seaspray}).

The number concentration of aerosol particles in the sea spray size distribution mode (N_{seaspray}) was derived from aerosol number size distributions measured with a scanning mobility particle sizer (SMPS) and aerodynamic particle sizer (APS) using the procedure following Modini et al. (2015). Co-located, 15 min median size distributions measured by the SMPS and APS were first joined together by interpolating the measurements to a common diameter scale represented in terms of geometric particle diameter, before a sequential lognormal mode-fitting procedure was applied to the joined size distributions, as described above for N_{Aitken} . The fitted sea spray lognormal modes were constrained to have modal diameters within 20 % of 180 nm and geometric standard deviations between 2 and 2.5, consistent with previous measurements of sea spray aerosol size distributions above breaking waves (Prather et al., 2013). N_{seaspray} represents the integrated number concentrations in the fitted sea spray modes. We estimate that the uncertainty in N_{seaspray} is $\pm 50\%$ based on a sensitivity analysis to the choice of constrained mode diameter over the range from 140 to 300 nm.

OV27: aerosol mass concentration of oxalate ($N_{\text{oxalate,PM}_{10}}$).
The mass concentration of oxalate in PM_{10} dry aerosol particles ($N_{\text{oxalate,PM}_{10}}$) was derived from offline high-volume sampled filters using ion chromatography. The formula for the oxalate di-anion is $\text{C}_2\text{O}_4^{2-}$.

OV28: aerosol mass concentration of bromide ($N_{\text{bromide,PM}_{10}}$).

The mass concentration of bromide in PM_{10} dry aerosol particles ($N_{\text{bromide,PM}_{10}}$) was derived from offline high-volume sampled filters using ion chromatography.

OV29: aerosol mass concentration of methanesulfonic acid ($N_{\text{MSA,PM}_{10}}$).

The mass concentration of methanesulfonic acid (MSA) in PM_{10} dry aerosol particles ($N_{\text{MSA,PM}_{10}}$) was derived from offline high-volume sampled filters using ion chromatogra-

phy. The formula for MSA is $\text{CH}_3\text{SO}_3\text{H}$.

OV30: aerosol mass concentration of sodium ($N_{\text{sodium,PM}_{10}}$).
The mass concentration of sodium in PM_{10} dry aerosol particles ($N_{\text{sodium,PM}_{10}}$) was derived from offline high-volume sampled filters using ion chromatography.

OV31: aerosol mass concentration of ammonium ($N_{\text{ammonium,PM}_{10}}$).

The mass concentration of ammonium in PM_{10} dry aerosol particles ($N_{\text{ammonium,PM}_{10}}$) was derived from offline high-volume sampled filters using ion chromatography.

OV32: aerosol mass concentration of potassium ($N_{\text{potassium,PM}_{10}}$).

The mass concentration of potassium in PM_{10} dry aerosol particles ($N_{\text{potassium,PM}_{10}}$) was derived from offline high-volume sampled filters using ion chromatography.

OV33: aerosol mass concentration of magnesium ($N_{\text{magnesium,PM}_{10}}$).

The mass concentration of magnesium in PM_{10} dry aerosol particles ($N_{\text{magnesium,PM}_{10}}$) was derived from offline high-volume sampled filters using ion chromatography.

OV34: aerosol mass concentration of calcium ($N_{\text{calcium,PM}_{10}}$).

Mass concentration of calcium in PM_{10} dry aerosol particles from offline high-volume filter sampling. The mass concentration of calcium in PM_{10} dry aerosol particles ($N_{\text{calcium,PM}_{10}}$) was derived from offline high-volume sampled filters using ion chromatography.

OV35: aerosol mass concentration of nitrate ($N_{\text{nitrate,PM}_{10}}$).

The mass concentration of nitrate in PM_{10} dry aerosol particles ($N_{\text{nitrate,PM}_{10}}$) was derived from offline high-volume sampled filters using ion chromatography.

OV36: sulfate (SO_4^{2-}).

Sulfate (SO_4^{2-}) is solid or liquid particles including sulfuric acid with a size of few micrometres. In this marine environment, it potentially originates from sea salt, ship exhaust, and natural marine emissions of dimethylsulfide.

OV37: chloride (Cl^-).

Chloride (Cl^-) is a clear reflection of the sea salt contribution to the aerosol concentrations. However, since the chloride signals were obtained via ToF-ACSM, only the non-refractory part of chloride is included, and the signal needs to be considered as a qualitative measurement.

OV38: gaseous sulfuric acid (H_2SO_4).

Atmospheric concentration of gaseous sulfuric acid (H_2SO_4) measured with a nitrate chemical ionisation mass spectrom-

eter. In the atmosphere, sulfuric acid is produced by the oxidation of sulfur dioxide, which can have both a natural or anthropogenic origin (e.g. phytoplankton emission or fossil fuel combustion). Data were cleaned from the influence of the ship exhaust, using the same methodology applied to all other aerosol measurements.

OV39: gaseous iodic acid (HIO₃).

Atmospheric concentration of gaseous iodic acid (HIO₃) measured with a nitrate chemical ionisation mass spectrometer. In the atmosphere, iodic acid is produced by the oxidation of the iodine radical, which can come from a variety of different iodine precursors (e.g. molecular iodine and diiodomethane). In the Southern Ocean the only known sources of iodine are natural, like phytoplankton, sea ice, and volcanoes. The ship exhaust was not found to influence the iodic acid concentration, and therefore the pollution mask was not applied to the data.

OV40: gaseous methanesulfonic acid (MSA).

Atmospheric concentration of gaseous methanesulfonic acid (CH₃SO₃H) measured with a nitrate chemical ionisation mass spectrometer. In the atmosphere, MSA is produced by the oxidation of dimethylsulfide, which can happen both in the gas phase and in the aqueous phase. The ship exhaust was not found to influence the MSA concentration, therefore the pollution mask was not applied to the data.

OV41: particle number concentration acting as CCN at 0.15 % supersaturation ($N_{\text{CCN},0.15}$).

The number concentration particles acting as CCN at 0.15 % ($N_{\text{CCN},0.15}$) was derived from in situ measurements using a CCN counter. In the instrument, the flow of sampled particles is directed through a column where a supersaturation of 0.15 % (equal to a relative humidity of 100.15 %) is upheld for 20 min during each measurement cycle. All particles that activate at set supersaturation are counted at the column exit by an optical particle counter. Assuming particle activation to be predominantly size dependent (Dusek et al., 2006), $N_{\text{CCN},0.15}$ hints at an abundance of the particles on the larger end of the sampled particle size range.

OV42: particle number concentration acting as CCN at 0.3 % supersaturation ($N_{\text{CCN},0.30}$).

The number concentration of particles acting as CCN at 0.3 % supersaturation ($N_{\text{CCN},0.3}$) was derived from in situ measurements using a CCN counter. In the instrument, the flow of sampled particles is directed through a column where a supersaturation of 0.3 % (equal to a relative humidity of 100.3 %) is upheld for 10 min during each measurement cycle. All particles that activate at set supersaturation are counted at column exit by an optical particle counter. $N_{\text{CCN},0.3}$ is a quantity relevant for aerosol–cloud interaction studies, as a supersaturation of 0.3 % is a typical value for

in-cloud conditions.

OV43: particle number concentration acting as CCN at 1.0 % supersaturation ($N_{\text{CCN},1.00}$).

The number concentration of particles acting as CCN at 1.0 % supersaturation ($N_{\text{CCN},1.0}$) was derived from in situ measurements using a CCN counter. In the instrument, the flow of sampled particles is directed through a column where a supersaturation of 1.0 % (equal to a relative humidity of 101 %) is upheld for 10 min during each measurement cycle. All particles that activate at set supersaturation are counted at column exit by an optical particle counter. Under the assumption that particle activation is predominantly size dependent Dusek et al. (2006), $N_{\text{CCN},1.0}$ hints at the abundance of the smaller end of the sampled particle size range when compared with N_{CCN} at a lower supersaturation.

OV44: hygroscopicity parameter of particles acting as CCN at 0.15 % supersaturation ($\kappa_{\text{CCN},0.15}$).

The hygroscopicity parameter for particles acting as CCN at 0.15 % supersaturation ($\kappa_{0.15}$) attempts to characterise the chemistry-dependent hygroscopicity of aerosol particles with a single parameter. κ was first proposed in Petters and Kreidenweis (2007) and is derived by integration of the particle number size distribution (PNSD) along decreasing particle diameter up until the diameter where the integral equals the respective N_{CCN} , i.e. the critical diameter (D_{crit}). Typical values are $\kappa = 0.0$ for insoluble material, $\kappa = 0.1$ for water-soluble organics, $\kappa = 0.61$ for ammonium sulfate, and $\kappa = 1.3$ for sodium chloride. Here, under the assumption that particle activation is predominantly size-dependent Dusek et al. (2006), $\kappa_{0.15}$ provides information on the chemical composition of the larger particles of our sampled size range.

OV45: hygroscopicity parameter of particles acting as CCN at 0.3 % supersaturation ($\kappa_{\text{CCN},0.30}$).

The hygroscopicity parameter for particles acting as CCN at 0.3 % supersaturation ($\kappa_{0.3}$) tries to describe the chemistry-dependent hygroscopicity of aerosol particles with a single parameter. κ was first proposed in Petters and Kreidenweis (2007) and is derived by integration of the PNSD along decreasing particle diameter, up until the diameter where the integral equals respective N_{CCN} , the critical diameter (D_{crit}). Typical values are $\kappa = 0.0$ for insoluble material, $\kappa = 0.1$ for water-soluble organics, $\kappa = 0.61$ for ammonium sulfate, and $\kappa = 1.3$ for sodium chloride. Here, $\kappa_{0.3}$ provides information on the chemical composition of particles relevant for in-cloud processes, as a supersaturation of 0.3 % is a typical value for in-cloud conditions.

OV46: hygroscopicity parameter of particles acting as CCN at 1.0 % supersaturation ($\kappa_{\text{CCN},1.00}$).

The hygroscopicity parameter for particles acting as CCN at 1.0 % supersaturation ($\kappa_{1.0}$) tries to describe the chemistry-dependent hygroscopicity of aerosol particles with a single

parameter. κ was first proposed in Petters and Kreidenweis (2007) and is derived by integration of the PNSD along decreasing particle diameter, up until the diameter where the integral equals respective N_{CCN} , the critical diameter (D_{crit}). Typical values are $\kappa = 0.0$ for insoluble material, $\kappa = 0.1$ for water-soluble organics, $\kappa = 0.61$ for ammonium sulfate, and $\kappa = 1.3$ for sodium chloride. Here, under the assumption that particle activation is predominantly size-dependent Dusek et al. (2006), $\kappa_{1.0}$ provides information on the chemical composition of the whole sampled size range, including both particles of larger and smaller diameter.

OV47: ice nuclei number concentration at -8°C from offline low-volume PM_{10} filter sampling ($N_{\text{INP,LV},-8}$).

The number concentration of INP at -8°C ($N_{\text{INP},-8,\text{LV}}$) is derived from offline low-volume filter sampling of PM_{10} particles. Ice activity at this temperature range is usually associated with biological particles (Kanji et al., 2017; O'Sullivan et al., 2018).

OV48: ice nuclei number concentration at -20°C from offline low-volume PM_{10} filter sampling ($N_{\text{INP,LV},-20}$).

The number concentration of INP at -20°C ($N_{\text{INP},-20,\text{LV}}$) is derived from offline low-volume filter sampling of PM_{10} particles. Ice activity at this temperature range is usually associated with mineral dust (Murray et al., 2012; Welti et al., 2018).

OV49: ice nuclei number concentration at -8°C from offline high-volume PM_{10} filter sampling ($N_{\text{INP,HV},-8}$).

The number concentration of INP at -8°C ($N_{\text{INP},-8,\text{HV}}$) is derived from offline high-volume filter sampling of PM_{10} particles. Ice activity at this temperature range is usually associated with signals from biological particles (Kanji et al., 2017; O'Sullivan et al., 2018).

OV50: ice nuclei number concentration at -20°C from offline high-volume PM_{10} filter sampling ($N_{\text{INP,HV},-20}$).

The number concentration of INP at -20°C ($N_{\text{INP},-20,\text{HV}}$) is derived from offline high-volume filter sampling of PM_{10} particles. Ice activity at this temperature range is usually associated with signals from mineral dust (Welti et al., 2018).

OV51: ratio of fluorescent to total aerosol particle number concentration for fine particles ($r_{\text{fluo},\text{fine}3\sigma}$).

The ratio of fluorescence to total aerosol particles number concentration with optical diameter smaller than $1\mu\text{m}$ and larger than 500nm . The aerosol particles were measured by a wideband integrated bioaerosol sensor.

OV52: ratio of fluorescent to total aerosol particle number concentration for coarse particles ($r_{\text{fluo},\text{coarse}3\sigma}$).

The ratio of fluorescence to total aerosol particles number concentration with optical diameter larger than $1\mu\text{m}$ and smaller than $20\mu\text{m}$. The aerosol particles were measured by

a wideband integrated bioaerosol sensor.

OV53: significant wave height (H_s).

Significant wave height is defined as 4 times the standard deviation of the surface elevation or equivalently as 4 times the square root of the zero-order moment (area) of the wave energy spectrum. Significant wave height is the integral measure of the total wave energy of the sea state and represents the average of the highest one-third of the waves.

OV54: spectral mean wave energy period ($T_{m-1,1}$).

Mean wave period is the characteristic time between two wave crests. It is associated with the wavelength and phase velocity (i.e. rate at which the wave propagates) via the linear dispersion relation. It provides a proxy of the distance from generation, i.e. short periods are associated to waves generated by the local wind, while long periods are linked to fully developed swell waves. Used in conjunction with the significant wave height (H_s), defines the shape of waves (steepness) a parameter that characterises that can be determined defining non-linear wave properties and can be used as a proxy of breaking probability. Here, the spectral mean wave energy period is used and is obtained using the reciprocal frequency moment of the wave spectrum.

OV55: sea surface height (SSH).

Sea surface height (SSH) is the satellite-derived absolute dynamic topography, which has been interpolated to the cruise track by Haumann et al. (2020b). Daily fields (0.25° resolution) are from the gridded and merged SSALTO/DUACS Delayed-Time Level-4 multi-satellite altimetry observations measurements (Altika Drifting Phase, Cryosat-2, Jason-3, OSTM/Jason-2 Interleaved, Sentinel-3A; version 5.9) distributed by CMEMS/Mercator Ocean (<http://marine.copernicus.eu>, last access: 9 March 2021) and created on 14 June 2018. We use the absolute dynamic topography, which is the sea surface height above geoid. We use the 1 min GPS date, latitude, and longitude record (Thomas and Pina Estany, 2019) to find the closest points in space and time in the gridded satellite product. We interpolate the four spatially closest satellite data points to the ship's location using a distance-weighted mean. This is done for the two closest fields in time, i.e. the daily average (centred at noon UTC) before and after the GPS record. These two points are then interpolated to the GPS time using a distance-weighted mean. Note that while the resolution of the record is 1 min along the cruise track, the actual temporal and spatial resolution is determined by the original product. That means that the dataset for example does not capture any daily cycle as the satellite data consists of daily means.

OV56: surface ocean geostrophic velocity (U_g).

Surface ocean geostrophic velocity (U_g) is calculated from the satellite-derived absolute geostrophic velocity zonal and meridional components, which have been interpolated

to the cruise track by Haumann et al. (2020b). Daily fields (0.25° resolution) are from the gridded and merged SSALTO/DUACS Delayed-Time Level-4 multi-satellite altimetry observations measurements (Altika Drifting Phase, Cryosat-2, Jason-3, OSTM/Jason-2 Interleaved, Sentinel-3A; version 5.9) distributed by CMEMS/Mercator Ocean (<http://marine.copernicus.eu>, last access: 9 March 2021) and created on 14 June 2018. We use both the zonal and meridional components of the absolute geostrophic velocity. We use the 1 min GPS date, latitude, and longitude record (Thomas and Pina Estany, 2019) to find the closest points in space and time in the gridded satellite product. We interpolate the four spatially closest satellite data points to the ship's location using a distance-weighted mean. This is done for the two closest fields in time, i.e. the daily average (centred at noon UTC) before and after the GPS record. These two points are then interpolated to the GPS time using a distance-weighted mean. Note that while the resolution of the record is 1 min along the cruise track, the actual temporal and spatial resolution is determined by the original product. That means that the dataset for example does not capture any daily cycle as the satellite data consists of daily means. We then calculate the magnitude of the surface ocean geostrophic velocity (U_g) as the square-root of the sum of the squared velocity components.

OV57: surface ocean temperature of seawater (T_{sw}).

Surface ocean temperature (T_{sw}) is largely derived from the thermosalinograph connected to the underway line (Haumann et al., 2020b), which has been corrected using the surface ocean temperature data from CTD (Henry et al., 2020) and expendable bathythermograph (XBT) probe (Haumann et al., 2020c) measurements. Temperature data from the thermosalinograph has been merged with satellite-derived sea surface temperature (Reynolds et al., 2007). For this purpose, we use satellite-derived, daily (0.25° resolution) NOAA optimally interpolated sea surface temperature data (version 2; Reynolds et al., 2007), which was downloaded 23 March 2018. We use the 1 min GPS date, latitude, and longitude record (Thomas and Pina Estany, 2019) to find the closest points in space and time in the gridded satellite product. We interpolate the four spatially closest satellite data points to the ship's location using a distance-weighted mean. This is done for the two closest fields in time, i.e. the daily average (centred at noon UTC) before and after the GPS record. These two points are then interpolated to the GPS time using a distance-weighted mean. Note that while the resolution of the record is 1 min along the cruise track, the actual temporal and spatial resolution is determined by the original product. That means that the satellite part of the temperature dataset for example does not capture any daily cycle as the satellite data consists of daily means. Missing data is filled with the satellite-derived temperature whenever no thermosalinograph temperature was available within ± 0.25 d. Any remaining gaps are

interpolated using the MATLAB modified Akima method. MATLAB's "modified Akima cubic hermite interpolation" is designed to avoid overshoots and is based on a piecewise function of third-order polynomials.

OV58: surface ocean mixed-layer depth (MLD).

Surface ocean mixed-layer depth (MLD) is estimated from both the CTD (Henry et al., 2020) and XBT vertical temperature profiles using the temperature threshold criterion (de Boyer Montégut et al., 2004) and is distributed as part of the XBT data publication (Haumann et al., 2020c). Note that due to the limited number of vertical temperature profiles, the spatio-temporal availability of MLD along the cruise track is very limited.

OV59: median light intensity within the mixed layer (I_g).

The median light intensity within the mixed layer (I_g ; $\mu\text{mol photons m}^{-2} \text{s}^{-1}$) is a derived parameter which aims to consolidate the vertical and diurnal variability in the photosynthetically active radiation (400 to 700 nm) light intensity within the upper mixed layer of the surface ocean into one parameter. Irradiance from the sun typically follows a sinusoidal pattern at the surface over the course of a day while decreasing exponentially with depth in the ocean. Phytoplankton cells are mixed freely within the upper mixed layer of the surface ocean and so this parameter represents the acclimation irradiance for phytoplankton and provides an indication of their "light history", which influences various photosynthetic and metabolic processes.

OV60: surface ocean potential density anomaly of seawater ($\sigma_{0,sw}$).

Potential density anomaly referenced to 0 dbar pressure ($\sigma_{0,sw}$) is calculated from merged surface ocean temperature (T_{sw}) and salinity (S_{sw}) data (Haumann et al., 2020b) using the MATLAB GSW toolbox (TEOS-10; McDougall and Barker, 2011). Here, the anomaly is defined with respect to 1000 kg m^{-3} .

OV61: surface ocean salinity of seawater (S_{sw}).

Surface ocean salinity (S_{sw}) is largely derived from the thermosalinograph connected to the underway line (Haumann et al., 2020b), which has been corrected using discrete seawater salinity samples collected from the underway line (Haumann et al., 2020a) whenever both products were available. Missing data in the thermosalinograph time series is filled with the measurements from the discrete seawater salinity samples whenever no thermosalinograph salinity was available within ± 0.25 d. Any remaining gaps are filled with interpolated values whenever at least one salinity measurement was available prior and after each time step within a 6 h window. The filling values are interpolated using MATLAB's modified Akima cubic hermite interpolation, which is designed to avoid overshoots and is based on a

piecewise function of third-order polynomials.

OV62: sea-ice concentration (C_i).

Sea-ice concentration (C_i) is the fraction of the surface area covered by sea ice. It is linearly interpolated to the cruise track Haumann et al. (2020b) from satellite-derived, daily (25 km by 25 km resolution) NOAA/NSIDC Climate Data Record of Passive Microwave Daily Southern Hemisphere Sea Ice Concentration (version 3; Meier et al., 2013; Peng et al., 2013), which was created on 30 November 2017. We use the 1 min GPS date, latitude, and longitude record (Thomas and Pina Estany, 2019) to find the closest points in space and time in the gridded satellite product. We interpolate the four spatially closest satellite data points to the ship's location using a distance-weighted mean. This is done for the two closest fields in time, i.e. the daily average (centred at noon UTC) before and after the GPS record. These two points are then interpolated to the GPS time using a distance-weighted mean. Note that while the resolution of the record is 1 min along the cruise track, the actual temporal and spatial resolution is determined by the original product. That means that the dataset for example does not capture any daily cycle as the satellite data consists of daily means.

OV63: surface ocean $\delta^{18}\text{O}$ of seawater ($\delta^{18}\text{O}_{\text{sw}}$).

The surface ocean seawater oxygen isotopic composition ($\delta^{18}\text{O}_{\text{sw}}$, OV202) was measured in discrete seawater samples collected from the underway line (Haumann et al., 2019). All samples were analysed for their oxygen isotopic composition (reported as per mille deviation of the oxygen-18 to oxygen-16 ratio from VSMOW2) by mass spectrometry at the British Geological Survey. $\delta^{18}\text{O}_{\text{sw}}$ provides insights into the type of surface freshwater fluxes (precipitation, evaporation, sea-ice melting and freezing, iceberg and land-ice melting) that determine the salinity of the seawater.

OV64: total chlorophyll a (TChl a).

Total chlorophyll a concentration (mg m^{-3}) is the sum of monovinyl and divinyl forms of chlorophyll a . Chlorophyll is the main light-harvesting pigment found in phytoplankton, photosynthetic microbes found in the sunlit layers of the ocean, and is responsible for primary production. The concentration of total chlorophyll a is often used as a proxy for overall phytoplankton abundance and biomass; however, the concentration per cell can vary depending on the species and environmental factors such as light and dissolved nutrient availability.

OV65: chlorophyll a fluorescence (Chl a_{fluo}).

Chlorophyll a fluorescence here refers to the in vivo pigment fluorescence as determined with a WetLabs ECO sensor located online in the ship's underway surface seawater flow. The sensor emits a light beam at 470 nm and measures backscatter fluorescence at 695 nm, which is specific for chlorophyll. Being an in vivo fluorescence measurement, it is

subject to light-driven fluctuations due to non-photochemical quenching. Thus, the signal is higher at night and lower during the day.

OV66: chlorophyllide a pigment concentration (Chlide a).

Chlorophyllide a (mg m^{-3}) is a transformation product of chlorophyll a (see TChl a), the dominant pigment found in phytoplankton, and has been associated with senescent phytoplankton cells and damaged diatoms.

OV67: pheophorbide a pigment concentration (Phaeob a).

Pheophorbide a (mg m^{-3}) is a transformation product of chlorophyll a (see TChl a), the dominant pigment found in phytoplankton, and has been associated with zooplankton grazing activity and found in sediments and material trapped in sea ice.

OV68: phaeophytin a pigment concentration (Phaeophy a).

Pheophytin a (mg m^{-3}) is a transformation product of chlorophyll a (see TChl a), the dominant pigment found in phytoplankton, and has been associated with senescent phytoplankton cells and damaged diatoms.

OV69: slope of the particle size distribution ($\text{PSD}_{\text{slope}}$).

The particle size distribution in the surface ocean was measured by counting particle concentrations (living and detrital) in discrete size bins between 2 to 60 μm , although the maximum particle size observed in the ACE dataset in the surface ocean was about 20 μm . The slope of the particle size distribution, estimated using a power law (or "Junge type" approximation), provides a numerical index that indicates shifts in the relative proportion of small vs. large particles, where a steeper slope indicates a greater proportion of small vs. large particles. In the open ocean, this parameter typically agrees with major shifts in the composition of the microbial community, particularly the phytoplankton. In locations closer to land masses or sea ice, the particle size distribution slope may also be influenced by additional contributions of detrital particles.

OV70: photochemical efficiency of photosystem II measured during the night.

F_{VF_M} is the maximum photochemical efficiency of photosystem II in phytoplankton when the cells are in their fully relaxed state (or after a period of darkness). More generally this parameter is considered the maximum photosynthetic efficiency or utilisation of absorbed light to drive the electron transport chain. F_{VF_M} is influenced by environmental factors such as light and dissolved nutrient availability, where excess light can result in an a reduction in F_{VF_M} that can last for hours after the event and a lack of available nutrients can also result in lower F_{VF_M} . Additionally, the maximum F_{VF_M} achievable can be constrained by taxonomic differences and hence the F_{VF_M} is influenced by phytoplankton community

structure. Note that this is a bulk water measurement.

OV71: photochemical efficiency of photosystem II during the day (Φ_{PSII}).

Φ_{PSII} is the effective photochemical efficiency of photosystem II in phytoplankton when the cells are exposed to light. Φ_{PSII} is lower than the $F_V F_M$ (see $F_V F_M$) of the sample because light exposure results in an increase in the baseline fluorescence due to closed photosynthetic reaction centres and quenching of the maximum fluorescence as a means to dissipate excess light. More generally this parameter $F_V F_M$ is considered the photosynthetic efficiency or utilisation of absorbed light to drive the electron transport chain. Like $F_V F_M$, Φ_{PSII} is influenced by environmental factors such as light and dissolved nutrient availability where excess light can result in an a further reduction in Φ_{PSII} , which can last for hours after the event and a lack of available nutrients can also result in lower Φ_{PSII} . Additionally, the maximum Φ_{PSII} achievable can be constrained by taxonomic differences, and hence the Φ_{PSII} is influenced by phytoplankton community structure. Note that this is a bulk water measurement.

OV72: functional absorption cross section of PSII during the night (σ_{PSII}).

σ_{PSII} ($\text{\AA}^2 \text{RCII}^{-1}$) is the functional absorption cross section of photosystem II in phytoplankton when cells are in a fully relaxed state (or after a period of darkness). More generally this parameter is the area of the cell harvesting incoming light and actively directing the light energy towards photosynthesis. The size of the functional absorption cross section reflects differences in taxa and short- and long-term responses to environmental conditions, namely light and dissolved nutrient concentrations. Note that this is a bulk water measurement.

OV73: functional absorption cross section of PSII during in the day (σ_{PSII}').

σ_{PSII}' ($\text{\AA}^2 \text{RCII}^{-1}$) is the functional absorption cross section of photosystem II in phytoplankton when the cells are exposed to light. More generally this parameter is the area of the cell harvesting incoming light and actively directing the light energy towards photosynthesis. σ_{PSII}' measured in the light is generally lower than σ_{PSII} (see σ_{PSII}') measured after darkness (or when cells are fully relaxed) due to fluorescence-quenching processes dissipating excess light. The size of the functional absorption cross section reflects differences in taxa and short- and long-term responses to environmental conditions, namely light and dissolved nutrient concentrations. Note that this is a bulk water measurement.

OV74: chlorophyte contribution to chlorophyll biomass (Chloro).

The parameter Chloro, shortened from “CHLORO-1 pigment type”, is an estimation of the contribution of phytoplankton species within the division *Chlorophyta* to the

chlorophyll *a* pigment biomass (mg m^{-3}) in a sample and by proxy contribution to the total phytoplankton biomass. Phytoplankton populations are composed of many species that have different biogeography in response to changing environmental conditions (e.g. light, temperature, dissolved macro- and micro-nutrients) and different biogeochemical or functional roles in the ocean. Examples of chlorophytes found in the Southern Ocean include *Chlorella* sp.

OV75: cryptophyte contribution to chlorophyll biomass (Crypto).

The parameter Crypto, shortened from “CRYPTO-1 pigment type”, is an estimation of the contribution of phytoplankton species within the division *Cryptophyta* to the chlorophyll *a* pigment biomass (mg m^{-3}) in a sample, and by proxy contribution to the total phytoplankton biomass. Phytoplankton populations are composed of many species that have different biogeography in response to changing environmental conditions (e.g. light, temperature, dissolved macro- and micro-nutrients) and different biogeochemical or functional roles in the ocean. Examples of cryptophytes found in the Southern Ocean include *Cyptomonas cf. actuta* and other *Cyptomonas* sp.

OV76: cyanobacteria type 2 contribution to chlorophyll biomass (Cyano).

The parameter Cyano, shortened from “CYANO-2 pigment type”, is an estimation of the contribution of phytoplankton species within the division *Cyanophyta* to the chlorophyll *a* pigment biomass (mg m^{-3}) in a sample and by proxy contribution to the total phytoplankton biomass. Phytoplankton populations are composed of many species that have different biogeography in response to changing environmental conditions (e.g. light, temperature, dissolved macro- and micro-nutrients) and different biogeochemical or functional roles in the ocean. Examples of cyanobacteria found in the Southern Ocean include *Synechococcus* sp.

OV77: diatom type contribution to chlorophyll biomass (DiatA).

The parameter DiatA, shortened from “DIATOM-1 pigment type” (chlorophyll *c1*, chlorophyll *c2*, and fucoxanthin containing), is an estimation of the contribution of phytoplankton species within the class *Bacillariophyceae* (commonly known as diatoms) to the chlorophyll *a* pigment biomass (mg m^{-3}) in a sample and by proxy contribution to the total phytoplankton biomass. Phytoplankton populations are composed of many species that have different biogeography in response to changing environmental conditions (e.g. light, temperature, dissolved macro- and micro-nutrients) and different biogeochemical or functional roles in the ocean. Examples of pigment type 1 bacillariophytes (commonly known as diatoms) found in the Southern Ocean include *Chaetoceros* sp. such as *C. debilis*, *C. brevis* and

C. dictyota and *Phaeodactylum tricornutum*.

OV78: diatom type 2 contribution to chlorophyll biomass (DiatB).

The parameter DiatB, shortened from “DIATOM-2 pigment type” (chlorophyll *c*2, chlorophyll *c*3, and fucoxanthin containing), is an estimation of the contribution of phytoplankton species within the class *Bacillariophyceae* (commonly known as diatoms) to the chlorophyll *a* pigment biomass (mg m^{-3}) in a sample and by proxy contribution to the total phytoplankton biomass. Phytoplankton populations are composed of many species which have different biogeography in response to changing environmental conditions (e.g. light, temperature, dissolved macro- and micro-nutrients) and different biogeochemical or functional roles in the ocean. Examples of pigment type 2 bacillariophytes (commonly known as diatoms) found in the Southern Ocean include *Pseudonitzschia* sp. such as *P. hemeii*, *P. barkeyi*.

OV79: dinoflagellate type 1 contribution to chlorophyll biomass (Dino).

The parameter DinoA, shortened from “DINO-1 pigment type” (lacking chlorophyll *c*3), is an estimation of the contribution of phytoplankton species within the class *Dinophyceae* (commonly known as dinoflagellates) to the chlorophyll *a* pigment biomass (mg m^{-3}) in a sample and by proxy contribution to the total phytoplankton biomass. Phytoplankton populations are composed of many species that have different biogeography in response to changing environmental conditions (e.g. light, temperature, dissolved macro- and micro-nutrients) and different biogeochemical or functional roles in the ocean. An example of a pigment type 1 dinophyte (commonly known as dinoflagellates) found in the Southern Ocean is *Amphidinium carterae*.

OV80: haptophyte type 8 contribution to chlorophyll biomass (Hapto8).

The parameter Hapto8, shortened from “HAPTO-8 pigment type” (lacking 19'-hexanoloxyfucoxanthin), is an estimation of the contribution of phytoplankton species within the division *Haptophyta* and class *Prymnesiophyceae* to the chlorophyll *a* pigment biomass (mg m^{-3}) in a sample and by proxy contribution to the total phytoplankton biomass. Phytoplankton populations are composed of many species that have different biogeography in response to changing environmental conditions (e.g. light, temperature, dissolved macro- and micro-nutrients) and different biogeochemical or functional roles in the ocean. An example of a pigment type 8 prymnesiophyte found in the Southern Ocean is *Phaeocystis antarctica*.

OV81: haptophyte types 6 and 7 contribution to chlorophyll biomass (Hapto67).

The parameter Hapto67, shortened from “HAPTO-67 pigment type” (containing 19'-hexanoloxyfucoxanthin), is

an estimation of the contribution of phytoplankton species within the division *Haptophyta* and class *Prymnesiophyceae* to the chlorophyll *a* pigment biomass (mg m^{-3}) in a sample and by proxy contribution to the total phytoplankton biomass. Phytoplankton populations are composed of many species that have different biogeography in response to changing environmental conditions (e.g. light, temperature, dissolved macro- and micro-nutrients) and different biogeochemical or functional roles in the ocean. An example of a pigment type 67 prymnesiophyte found in the Southern Ocean is *Emiliania huxleyi*.

OV82: prasinophyte type 3 contribution to chlorophyll biomass (Prasino).

The parameter Pras3, shortened from “PRAS-3 pigment type” (containing prasinoxanthin), is an estimation of the contribution of phytoplankton species within the class *Prasinophyceae* to the chlorophyll *a* pigment biomass (mg m^{-3}) in a sample, and by proxy contribution to the total phytoplankton biomass. Phytoplankton populations are composed of many species that have different biogeography in response to changing environmental conditions (e.g. light, temperature, dissolved macro- and micro-nutrients) and different biogeochemical or functional roles in the ocean. An example of a pigment type 3 prasinophyte found in the Southern Ocean is *Micromonas* sp.

OV83: pelagophyte contribution to chlorophyll biomass (Pelago).

The parameter Pelago, shortened from “PELAGO-1 pigment type”, is an estimation of the contribution of phytoplankton species within the class *Pelagophyceae* to the chlorophyll *a* pigment biomass (mg m^{-3}) in a sample and by proxy contribution to the total phytoplankton biomass. Phytoplankton populations are composed of many species that have different biogeography in response to changing environmental conditions (e.g. light, temperature, dissolved macro- and micro-nutrients) and different biogeochemical or functional roles in the ocean. An example of a pigment type 1 pelagophyte found in the Southern Ocean is *Pelagomonas* sp.

OV84: Total bacterial abundance ($N_{\text{totalbacteria}}$)

Total bacteria actually refers to total heterotrophic prokaryotes, which include non-chloroplast-containing bacteria and archaea. However, the abundance of bacteria largely overcomes the abundance of archaea. Because of the method used (flow cytometry of single cells), particle-attached cells are not counted, and the variable is to be considered free-living heterotrophic prokaryotes.

OV85: abundance of *Synechococcus* ($N_{\text{synechococcus}}$).

This is the abundance of the cosmopolitan unicellular cyanobacteria within the genus *Synechococcus*. They are identified by their unique autofluorescence vs. size signal in a flow cytometer. *Synechococcus* are primary producers

that belong in picophytoplankton. They are one of the most abundant organisms on Earth, yet they thrive better in warmer waters than in polar waters.

OV86: abundance of nanoeukaryotes ($N_{\text{nanoeukaryotes}}$).

Nano-eukaryotes here refer to nano-sized (3 to 10 μm) eukaryotic phytoplankton. Because of the method used to count them (autofluorescence vs. size in a flow cytometer) they only include chloroplast-containing cells. Nano-eukaryotes is an operational (not taxonomical) definition. The group actually embraces a great variety of taxonomic groups, including haptophytes, chlorophytes, small dinoflagellates, and small diatoms.

OV87: abundance of picoeukaryotes ($N_{\text{picoeukaryotes}}$).

Pico-eukaryotes here refer to pico-sized (< 3 μm) eukaryotic phytoplankton. Because of the method used to count them (autofluorescence vs. size in a flow cytometer) they only include chloroplast-containing cells. Pico-eukaryotes is an operational (not taxonomical) definition. The group actually embraces the smallest representatives of a great variety of taxonomic groups, typically including large numbers of haptophytes and prasinophytes.

OV88: dissolved nitrate concentration in seawater (Nitrate).

Nitrogen is an essential component of amino acids in phytoplankton and essential for their growth and productivity. In the ocean it is available to phytoplankton in three inorganic forms, nitrate (NO_3^-), nitrite (NO_2^-), and ammonium (NH_4^+), as well as organic forms. Dissolved nitrate (μm) is usually the most abundant form of the dissolved inorganic nitrogen sources in the ocean, and generally concentrations in the Southern Ocean are some of the highest of any ocean across the globe but do vary spatially and temporally.

OV89: dissolved nitrite concentration in seawater (Nitrite).

Nitrogen is an essential component of amino acids in phytoplankton and essential for their growth and productivity. In the ocean it is available to phytoplankton in three inorganic forms, nitrate (NO_3^-), nitrite (NO_2^-), and ammonium (NH_4^+), as well as organic forms. Nitrite (NO_2^- ; μm) is an intermediate form of inorganic nitrogen formed when microorganisms oxidise organic nitrogen back to inorganic nitrate. Dissolved nitrite is typically found in low concentrations, but concentrations in the Southern Ocean are generally higher than other oceans and varies spatially and temporally.

OV90: dissolved phosphate concentration in seawater (Phosphate).

Dissolved inorganic phosphate in seawater (PO_4^{3-} ; μm) is one of the essential macronutrients required for phytoplankton growth. Phytoplankton utilise phosphorus for protein synthesis, construction of phospholipids in cellular structures, storage and transmission of genetic informa-

tion, metabolic signalling, energy transduction (adenosine triphosphate; ATP), and stress responses. Generally phosphate concentrations in the Southern Ocean are some of the highest of any ocean across the globe; however, the distribution is spatially and temporally variable.

OV91: dissolved silicate concentration in seawater (Silicate).

Dissolved inorganic silicate in seawater ($\text{Si}(\text{OH})_4$; μm) is one of the essential macronutrients required for phytoplankton growth. Phytoplankton have a small demand for silicon for protein synthesis, but more importantly the phytoplankton phylum Bacillariophyta (more commonly known as Diatoms) require silicon for the synthesis of their cell walls. Diatoms play a significant biogeochemical role in the Southern Ocean and are responsible for increased productivity and carbon export. Generally silicate concentrations in the Southern Ocean are some of the highest of any ocean across the globe; however, the distribution is spatially and temporally variable.

OV92: dissolved ammonium in seawater (Ammonium).

Nitrogen is an essential component of amino acids in phytoplankton and essential for their growth and productivity. In the ocean it is available to phytoplankton in three inorganic forms, nitrate (NO_3^-), nitrite (NO_2^-), and ammonium (NH_4^+), as well as organic forms. Ammonium (NH_4^+) is an indicator of biological activity where the mixed-layer concentration is controlled by the balance between excretion from zooplankton and uptake by phytoplankton. Higher dissolved ammonium concentrations are associated with areas of increased biological activity, often in close proximity to landmasses.

OV93: particulate organic carbon (POC).

Particulate organic carbon (POC; μm) measurements are estimations of the organic carbon content of living and detrital particles (including fecal pellets, senescent cells, aggregated material, and terrestrially derived organic matter), and for this dataset includes particles > 0.7 μm in size in the surface ocean. Under the right conditions, particulate organic carbon is exported to the seafloor as part of the biological pump and the concentrations in the surface ocean are linked to the abundance and productivity of phytoplankton who synthesise POC through photosynthesis. Processes such as heterotrophy and grazing by zooplankton can also impact the POC concentration.

OV94: particulate organic nitrogen (PON).

Particulate organic nitrogen (PON; μm) measurements are estimations of the organic nitrogen content of living and detrital particles (including fecal pellets, senescent cells, aggregated material, and terrestrially derived organic matter), and for this dataset includes particles > 0.7 μm in size in the surface ocean. Particulate organic nitrogen enters the

ocean cycle through the uptake of various forms of nitrogen by microbes including phytoplankton and conversion into organic matter or the introduction of terrestrially derived organic matter containing nitrogen near landmasses or sea ice.

OV95: particulate organic carbon to nitrogen ratio (C : N). Particulate organic carbon (POC) and particulate organic nitrogen (PON) are key components of particulate organic matter found in the ocean. In this dataset, organic matter content was measured in particles $> 0.7 \mu\text{m}$ in size in the surface ocean including living and detrital particles (including fecal pellets, senescent cells, aggregated material and terrestrially derived organic matter). The ratio of POC:PON (or simply the C : N ratio) is often considered in the context of the ecological stoichiometry of plankton and in comparison to the Redfield ratio (C : N of ~ 6); a constant ratio of C : N (and other elements) is reflective of the elemental requirements for phytoplankton. Deviations from the Redfield ratio can indicate nutrient limitation and/or acclimation by phytoplankton to the nutrient supply but may also vary with taxa.

OV96: transparent exopolymeric particles (TEP). Transparent exopolymeric particles (TEP) are polysaccharide-rich, gel-like substances that account for a remarkable proportion of particulate organic carbon in the ocean. TEP is an operational definition, referring to the particles stainable with Alcian blue. Their concentration is calibrated against xanthan gum. TEP are produced mainly by phytoplankton and degraded by bacteria and UV radiation. They can make it to the atmosphere as part of primary organic aerosols.

OV97: Coomassie stainable particles (CSP). Coomassie stainable particles (CSP) are protein-rich, gel-like substances that account for a not yet quantified proportion of particulate organic carbon and nitrogen in the ocean. CSP is an operational definition, referring to the particles stainable with Coomassie brilliant blue. Their concentration is calibrated against bovine serum albumin. CSP are produced mainly by phytoplankton and expected to be degraded mainly by bacteria.

OV98: Absorption at 350 nm by coloured dissolved organic matter (a_{CDOM}). Light in the ocean is attenuated (absorbed and scattered) by seawater, particles, and dissolved matter, including coloured dissolved organic matter (CDOM). CDOM is the coloured optically active component of dissolved organic matter (DOM) also known as dissolved organic carbon (DOC). CDOM absorbs most strongly in the ultraviolet and blue wavelengths, decreasing exponentially towards the red and infrared wavelengths and is generally strongly positively correlated with the concentration of DOC, although this relationship can vary. The parameter absorption

by CDOM at 350 nm (m^{-1}) can be considered as both an indicator of factors controlling underwater light attenuation as part of the light absorption budget and as a proxy for DOC.

OV99: slope of detrital particulate absorption ($a_{\text{nap slope}}$). Detrital particles in the ocean are contributed by many inorganic and organic sources including phytoplankton through the decomposition of senescent cells, food web interactions with zooplankton, terrestrial run-off, melting sea-ice, and sediment resuspension. Absorption by detrital particles is strongest at ultraviolet wavelengths and decays exponentially with longer visible wavelengths. The spectral slope (nm^{-1}) parameterises the exponential decay and can offer additional information on the composition and source of the material. Some observations suggest that higher proportions of mineral to organic matter result in higher spectral slopes.

OV100: ratio of detrital absorption to total particulate absorption at 440 nm ($a_{\text{nap}}/a_{\text{p}}$). Light in the ocean is attenuated (absorbed and scattered) by seawater, dissolved matter, and particles, including phytoplankton and non-phytoplankton particles, sometimes referred to as detritus. Total particulate absorption is equal to the sum of absorption by phytoplankton particles and non-phytoplankton particles. Detritus comes from a variety of sources including the decomposition of senescent phytoplankton cells, from food web interactions with zooplankton, from terrestrial run-off, melting sea ice, and sediment resuspension. Generally in the open ocean the non-algal particulate contribution to the absorption co-varies with the phytoplankton component or chlorophyll *a*, and the non-algal particulate absorption is proportional to the phytoplankton absorption. Increases in the ratio of detrital to total absorption can indicate the additional input of material from terrestrial sources, melting sea ice, or sediment resuspension, as well a shift in the optically active components controlling the attenuation of underwater light.

OV101: acrylate (acrylate). The anion acrylate ($\text{CH}_2=\text{CHCOO}^-$) is produced (along with dimethyl sulfide) as a breakup product of the algal osmolyte dimethylsulfoniopropionate. It is toxic at high concentrations but rapidly consumed by bacteria at the nanomolar concentrations at which it occurs in the surface ocean.

OV102: dimethylsulfoniopropionate (DMSP). Dimethylsulfoniopropionate ($(\text{CH}_3)_2\text{S}+\text{CH}_2\text{CH}_2\text{COO}^-$) is a zwitterion that occurs in the surface ocean at nanomolar concentrations. It is a cosmopolitan compatible solute and osmolyte in phytoplankton and macroalgae, most abundant in haptophytes and dinoflagellates. When released from the algal cell, it is rapidly utilised by bacteria as a source of reduced sulfur for amino acids, with dimethyl sulfide, acrylate,

and methanethiol as by-products of DMSP catabolism.

OV103: dimethyl sulfide (DMS).

Dimethyl sulfide (DMS, $\text{H}_3\text{C-S-CH}_3$) is a biogenic volatile compound produced by the breakup of its major precursor, the algal osmolyte dimethylsulfoniopropionate. Enzymes for DMS production occur in phytoplankton and bacteria. DMS occurs at nanomolar concentrations in the surface ocean and accounts for 90 % of the oceanic emission of volatile sulfur. Once in the atmosphere, it is oxidised within hours mainly to sulfuric and methanesulfonic acids, which participate in aerosol formation and growth.

OV104: carbonyl sulfide (CSO).

Carbonyl sulfide (OCS) is a volatile compound produced in the surface ocean (where it occurs at picomolar concentrations) mainly through photochemical reactions of dissolved organic matter. It is by far the most abundant and stable sulfur gas in the atmosphere, from which it can return to the ocean, be taken up by terrestrial plants or reach the stratosphere, where it represents a major source of sulfate.

OV105: carbon disulfide (CS_2).

Carbon disulfide (CS_2) is a volatile compound produced by anaerobic decomposition of organic matter or in the surface ocean (where it occurs at picomolar concentrations) by photochemical reactions of dissolved organic matter. It oxidises rapidly in the atmosphere.

OV106: air mixing ratio of isoprene ($\text{Isoprene}_{\text{sea}}$).

Isoprene or 2-methyl-1,3-butadiene (C_5H_8) is a biogenic volatile organic compound produced by terrestrial plants and oceanic phytoplankton as a by-product of photosynthesis. It occurs in the surface ocean at picomolar concentrations and when emitted to the atmosphere oxidises within hours, thereby contributing to regulate the atmospheric oxidative capacity and participating in aerosol growth.

OV107: bromoform (CHBr_3).

Bromoform or tribromomethane (CHBr_3) is a volatile compound produced in the surface ocean (where it occurs at picomolar concentrations) by macroalgae and microalgae, probably as a by-product of oxidative stress. It is short-lived in the troposphere, where it acts to regulate ozone concentration.

OV108: Dibromomethane (CH_2Br_2).

Dibromomethane (CH_2Br_2) is a volatile compound produced in the surface ocean (where it occurs at picomolar concentrations) by macroalgae and microalgae, probably as a by-product of oxidative stress. It is short-lived in the troposphere, where it acts to regulate ozone concentration.

OV109: net community production (NCP).

Net community production (NCP) reflects the balance

between photosynthesis and respiration. It is a key parameter describing the marine carbon cycle. At steady state, NCP represents the carbon export production from the sunlit surface ocean. During ACE, NCP was estimated from biological oxygen saturation based on O_2/Ar ratios. In brief, surface seawater dissolved O_2 and Ar were continuously measured from the ship's flow-through seawater system by an equilibrator inlet mass spectrometer (Cassar et al., 2009). NCP in units of $\text{O}_2 \text{ m}^{-2} \text{ d}^{-1}$ was then derived as described in Eveleth et al. (2017) with a modification to wind parameterisation (Teeter et al., 2018) and a linear correction for sea ice.

OV110: distance to the nearest shore (d_{land}).

The distance to the nearest shore (in metres) has been derived from the GPS track of the R/V *Akademik Tryoshnikov* (<https://doi.org/10.5281/zenodo.3772377>). Shapefiles of continents have been downloaded from NaturalEarth physical (50 m grid, version 4.1.0). Small islands were added manually as single GPS locations. The distance of the GPS track with shores has been computed with NNJoin plugin (v3.1.2) of qGIS (v3.2.3).

OV111: water depth (d_{water}).

Depth of the seabed along the 5 min averaged cruise track was calculated from the General Bathymetric Chart of the Oceans (GEBCO Compilation Group, 2019) gridded 30 arcsec bathymetry data. The nearest gridded value from the bathymetry dataset was used to find the depth at the averaged position.

Code and data availability. The python code that was used for the analysis and to create the plots is available at <https://renkulab.io/gitlab/ACE-ASAID/spca-decomposition> (last access: 29 March 2021; Volpi, 2021) and as a Renku project <https://renkulab.io/projects/ACE-ASAID/spca-decomposition> (last access: 29 March 2021; Volpi and Landwehr, 2021).

For the availability of the data used in this study please refer to Tables B1 to B8 in Appendix B.

Supplement. The supplement related to this article is available online at: <https://doi.org/10.5194/esd-12-1295-2021-supplement>.

Author contributions. JS, DW, AT, NC, and RS conceived the idea. JS supervised the project. DW coordinated the ACE research cruise. CT, IT, JT, CGB, MHD, GC, NC, VF, CMR, YL, RA, AA, FAH, AB, PRR, RS, IG, SEF, HJF, AM, PCG, PRR, LX, MZ, JS, SL, and KCL provided the datasets that were used in this study. MV, FPC, and SL developed the analysis and implemented the data ingestion. SL and MV produced the results of the sPCA. SL and JS organised meetings with the co-authors where the results were interpreted and discussed and coordinated the writing process. SL, MV, FAH, IT, CMR, CT, SH, RLM, JS, VF, AB, RS, IG, HJF, CH, RA,

NC, and JT wrote the manuscript together. All authors commented on the manuscript.

Competing interests. The authors declare that they have no conflict of interest.

Disclaimer. Publisher's note: Copernicus Publications remains neutral with regard to jurisdictional claims in published maps and institutional affiliations.

Acknowledgements. This work would not have been possible without the following contributions. Our gratitude goes first to David Walton, Chief scientist of the ACE cruise and early supporter of this project; we also thank Danièle Rod, Philippe Gillet, and Franziska Aemisegger for their contribution to the ACE-DATA proposal. We thank the members of ACE Project 1, David Antoine, Sandy Thomalla, Thomas Ryan-Keogh, Nina Schuback, Hazel Little, David Berliner, William Moutier, and Alexandra Olivier-Morgan, for providing datasets to this project. We thank members of ACE Project 7, Fiona Tummon for installing the iDirac instrument and operating it during leg 1; Markus Hartmann and André Welti for operating instruments on leg 1 and 3, respectively; and Martin Gysel-Beer for great discussions on data analysis and interpretation. We thank Heini Wernli (ACE Project 11) for his ideas and advice during the starting phase of the ACE-DATA project. We thank the members and collaborators of ACE Project 8 Gonzalo L. Pérez, Eva Ortega-Retuerta, Miguel Cabrera, Yaiza Castillo, and David J. Kieber for assistance with data processing. We thank the crew of the *Akademik Tryoshnikov*. The Antarctic Circumnavigation Expedition was funded by the Swiss Polar Institute and Ferring Pharmaceuticals. Michele Volpi, Sebastian Landwehr, and Julia Schmale were supported by the Swiss Data Science Center (project no. C17-02). Jenny Thomas, Sebastian Landwehr, and Iris Thurnherr were supported by the Swiss Polar Institute. Jenny Thomas was supported by the ACE Foundation. F. Alexander Haumann was supported by the National Science Foundation (NSF) Southern Ocean Carbon and Climate Observations and Modeling (SOCCOM) Project under the NSF Award PLR-1425989, and through a grant from the BNP Paribas Foundation. Irina Gorodetskaya thanks SPI and also FCT/MCTES for the national support to CESAM (UIDP/500017/2020+UIDB/500017/2020) and the FCT Project ATLACE (CIRCNA/CAC/0273/2019) through national funds. Sarah E. Fawcett and Heather J. Forrer were supported by the South African National Antarctic Programme and National Research Foundation. Sarah E. Fawcett also recognises the support of a Royal Society/African Academy of Sciences FLAIR fellowship. Alberto Alberello and Alessandro Toffoli were supported by the Australian Antarctic Science Program (project 4434). Alberto Alberello is supported by the Japanese Society for the Promotion of Science (PE19055). Gang Chen was supported by the cost action of Chemical On-Line cOmpoSition and Source Apportionment of fine aerosol (COLOSSAL, CA16109), a COST-related project of the Swiss National Science Foundation; Source apportionment using long-term Aerosol Mass Spectrometry and Aethalometer Measurements (SAMSAM, IZCOZO_177063); and the EU Horizon 2020 Framework Programme via the ERA-PLANET project

SMURBS (grant agreement no. 689443). Ruth Airs was supported by the UK Research and Innovation Natural Environment Research Council grants NE/P008526/1 and NE/P021409/1. Neil Harris, Conor G. Bolas, and Valerio Ferracci were supported by NERC grants NE/K016377/1 and NE/S00579X/1. A workshop funded by NE/P008526/1 aided early discussions for combining ACE datasets. Christel Hassler was supported by the Swiss National Foundation for scientific research professor fellowship PP00P2_166197. Nicolas Cassar was supported by the “Laboratoire d’Excellence” LabexMER (ANR-10-LABX-19) and cofunded by a grant from the French government under the program “Investissements d’Avenir”. Christian Tatzelt and Silvia Henning were supported by the Deutsche Forschungsgemeinschaft (DFG) in the framework of the priority programme “Antarctic Research with comparative investigations in Arctic ice areas” by grants STR 453/12-1 and HE 6770/3-1. This research was partially supported by the Australian Government through the Australian Research Council’s Discovery Projects funding scheme (project DP160103387). Charlotte M. Robinson was supported by the Australian Government through the Australian Research Council’s Discovery Projects funding scheme (project DP DP160103387). Rafel Simó, Marina Zamanillo, Pau Cortés-Greus, and Pablo Rodríguez-Ros were supported by the Spanish Ministry of Science through the BIOGAPS project (CTM2016-81008-R). Julia Schmale holds the Ingvar Kamprad Chair for Extreme Environments Research sponsored by Ferring Pharmaceuticals.

Financial support. This research has been supported by the Schweizerischer Nationalfonds zur Förderung der Wissenschaftlichen Forschung (grant nos. PZ00P2_142684, P2E2P2_175162, P400P2_186681, 200021_169090, and PP00P2_166197), the Council for Scientific and Industrial Research, South Africa (grant no. SNA2011112600001), and the CSIR Southern Ocean Carbon and Climate Observatory (SOCCO) programme).

Review statement. This paper was edited by Christoph Heinze and reviewed by three anonymous referees.

References

- Aemisegger, F. and Sjolte, J.: A Climatology of Strong Large-Scale Ocean Evaporation Events. Part II: Relevance for the Deuterium Excess Signature of the Evaporation Flux, *J. Climate*, 31, 7313–7336, <https://doi.org/10.1175/JCLI-D-17-0592.1>, 2018.
- Alberello, A., Bennets, L., Heil, P., Eayrs, C., Vichi, M., MacHutchon, K., Onorato, M., and Toffoli, A.: Drift of pancake ice floes in the winter Antarctic marginal ice zone during polar cyclones, *J. Geophys. Res.-Oceans*, 125, e2019JC015418, <https://doi.org/10.1029/2019JC015418>, 2020.
- Ardhuin, F., Otero, M., Merrifield, S., Grouazel, A., and Terrill, E.: Ice break-up controls dissipation of wind-waves across Southern Ocean sea ice, *Geophys. Res. Lett.*, 47, e2020GL087699, <https://doi.org/10.1029/2020gl087699>, 2020.
- Arrigo, K. R., Mills, M. M., Kropuenske, L. R., van Dijken, G. L., Alderkamp, A.-C., and Robinson, D. H.: Photophysiology in two major Southern Ocean phytoplankton taxa: photosynthesis and

- growth of *Phaeocystis antarctica* and *Fragilariopsis cylindrus* under different irradiance levels, *Integr. Comp. Biol.*, 50, 950–966, <https://doi.org/10.1093/icb/icq021>, 2010.
- Arteaga, L. A., Boss, E., Behrenfeld, M. J., Westberry, T. K., and Sarmiento, J. L.: Seasonal Modulation of Phytoplankton Biomass in the Southern Ocean, *Nat. Commun.*, 11, 5364, <https://doi.org/10.1038/s41467-020-19157-2>, 2020.
- Atkinson, A., Whitehouse, M. J., Priddle, J., Cripps, G. C., Ward, P., and Brandon, M. A.: South Georgia, Antarctica: A Productive, Cold Water, Pelagic Ecosystem, *Marine Ecol. Prog. Ser.*, 216, 279–308, <https://doi.org/10.3354/meps216279>, 2001.
- Baccarini, A., Karlsson, L., Dommen, J., Duplessis, P., Vüllers, J., Brooks, I. M., Saiz-Lopez, A., Salter, M., Tjernström, M., Baltensperger, U., Zieger, P., and Schmale, J.: Frequent new particle formation over the high Arctic pack ice by enhanced iodine emissions, *Nat. Commun.*, 11, 4924, <https://doi.org/10.1038/s41467-020-18551-0>, 2020.
- Baccarini, A., Dommen, J., Lehtipalo, K., Henning, S., Modini, R. L., Gysel-Beer, M., Baltensperger, U., and Schmale, J.: Low-volatility vapors and new particle formation over the Southern Ocean during the Antarctic Circumnavigation Expedition, *Earth and Space Science Open Archive*, p. 31, <https://doi.org/10.1002/essoar.10506899.1>, 2021.
- Baden, T., Berens, P., Franke, K., Rosón, M. R., Bethge, M., and Euler, T.: The functional diversity of retinal ganglion cells in the mouse, *Nature*, 529, 345–350, <https://doi.org/10.1038/nature16468>, 2016.
- Barnes, I., Hjorth, J., and Mihalopoulos, N.: Dimethyl sulfide and dimethyl sulfoxide and their oxidation in the atmosphere, *Chem. Rev.*, 106, 940–975, <https://doi.org/10.1021/cr020529+>, 2006.
- Behrenfeld, M. J., Boss, E., Siegel, D. A., and Shea, D. M.: Carbon-based ocean productivity and phytoplankton physiology from space, *Global Biogeochem. Cycles*, 19, GB1006, <https://doi.org/10.1029/2004gb002299>, 2005.
- Bigg, E. K.: Ice Nucleus Concentrations in Remote Areas, *J. Atmos. Sci.*, 30, 1153–1157, [https://doi.org/10.1175/1520-0469\(1973\)030<1153:INCIRA>2.0.CO;2](https://doi.org/10.1175/1520-0469(1973)030<1153:INCIRA>2.0.CO;2), 1973.
- Blain, S., Tréguer, P., Belviso, S., Bucciarelli, E., Denis, M., Desabre, S., Fiala, M., Martin Jézéquel, V., Le Fèvre, J., Mayzaud, P., Marty, J.-C., and Razouls, S.: A biogeochemical study of the island mass effect in the context of the iron hypothesis: Kerguelen Islands, Southern Ocean, *Deep-Sea Res. Pt. I*, 48, 163–187, [https://doi.org/10.1016/s0967-0637\(00\)00047-9](https://doi.org/10.1016/s0967-0637(00)00047-9), 2001.
- Blain, S., Quéguiner, B., Armand, L., Belviso, S., Bombled, B., Bopp, L., Bowie, A., Brunet, C., Brussaard, C., Carlotti, F., Christaki, U., Corbière, A., Durand, I., Ebersbach, F., Fuda, J.-L., Garcia, N., Gerringa, L., Griffiths, B., Guigue, C., Guillerm, C., Jacquet, S., Jeandel, C., Laan, P., Lefèvre, D., Lo Monaco, C., Malits, A., Mosseri, J., Obernosterer, I., Park, Y.-H., Picheral, M., Pondaven, P., Remenyi, T., Sandroni, V., Sarthou, G., Savoye, N., Scouarnec, L., Souhaut, M., Thullier, D., Timmermans, K., Trull, T., Uitz, J., van Beek, P., Veldhuis, M., Vincent, D., Viollier, E., Vong, L., and Wagener, T.: Effect of Natural Iron Fertilization on Carbon Sequestration in the Southern Ocean, *Nature*, 446, 1070–1074, <https://doi.org/10.1038/nature05700>, 2007.
- Blair, G. S., Henrys, P., Leeson, A., Watkins, J., Eastoe, E., Jarvis, S., and Young, P. J.: Data Science of the Natural Environment: A Research Roadmap, *Front. Environ. Sci.*, 7, 121, <https://doi.org/10.3389/fenvs.2019.00121>, 2019.
- Boyd, P. W.: The role of iron in the biogeochemistry of the Southern Ocean and equatorial Pacific: a comparison of in situ iron enrichments, *Deep-Sea Res. Pt. II*, 49, 1803–1821, [https://doi.org/10.1016/s0967-0645\(02\)00013-9](https://doi.org/10.1016/s0967-0645(02)00013-9), 2002.
- Boyd, P. W., Jickells, T., Law, C. S., Blain, S., Boyle, E. A., Buesseler, K. O., Coale, K. H., Cullen, J. J., de Baar, H. J. W., Follows, M., Harvey, M., Lancelot, C., Levasseur, M., Owens, N. P. J., Pollard, R., Rivkin, R. B., Sarmiento, J., Schoemann, V., Smetacek, V., Takeda, S., Tsuda, A., Turner, S., and Watson, A. J.: Mesoscale iron enrichment experiments 1993–2005: synthesis and future directions, *Science*, 315, 612–617, <https://doi.org/10.1126/science.1131669>, 2007.
- Boylan, P., Helmig, D., and Oltmans, S.: Ozone in the Atlantic Ocean Marine Boundary Layer, *Elementa*, 3, 000045, <https://doi.org/10.12952/journal.elementa.000045>, 2015.
- Browning, K. A.: Organization of Clouds and Precipitation in Extratropical Cyclones, pp. 129–153, *American Meteorological Society*, Boston, MA, https://doi.org/10.1007/978-1-944970-33-8_8, 1990.
- Browning, K. A.: The Sting at the End of the Tail: Damaging Winds Associated with Extratropical Cyclones, *Q. J. Roy. Meteor. Soc.*, 130, 375–399, <https://doi.org/10.1256/qj.02.143>, 2004.
- Browning, T., Bouman, H., and Moore, C.: Satellite-detected fluorescence: Decoupling nonphotochemical quenching from iron stress signals in the South Atlantic and Southern Ocean, *Global Biogeochem. Cycles*, 28, 510–524, <https://doi.org/10.1002/2013gb004773>, 2014.
- Butterworth, B. J. and Miller, S. D.: Air-Sea Exchange of Carbon Dioxide in the Southern Ocean and Antarctic Marginal Ice Zone, *Geophys. Res. Lett.*, 43, 7223–7230, <https://doi.org/10.1002/2016GL069581>, 2016.
- Campagne, P., Crosta, X., Houssais, M. N., Swingedouw, D., Schmidt, S., Martin, A., Devred, E., Capo, S., Marieu, V., Closset, I., and Massé, G.: Glacial Ice and Atmospheric Forcing on the Mertz Glacier Polynya over the Past 250 Years, *Nat. Commun.*, 6, 6642, <https://doi.org/10.1038/ncomms7642>, 2015.
- Carranza, M. M. and Gille, S. T.: Southern Ocean wind-driven entrainment enhances satellite chlorophyll-a through the summer, *J. Geophys. Res.-Oceans*, 120, 304–323, <https://doi.org/10.1002/2014jc010203>, 2015.
- Cassar, N., Bender, M. L., Barnett, B. A., Fan, S., Moxim, W. J., Levy, H., and Tilbrook, B.: The Southern Ocean biological response to aeolian iron deposition, *Science*, 317, 1067–1070, <https://doi.org/10.1126/science.1144602>, 2007.
- Cassar, N., Barnett, B. A., Bender, M. L., Kaiser, J., Hamme, R. C., and Tilbrook, B.: Continuous High-Frequency Dissolved O₂/Ar Measurements by Equilibrator Inlet Mass Spectrometry, *Anal. Chem.*, 81, 1855–1864, <https://doi.org/10.1021/ac802300u>, 2009.
- Cassar, N., DiFiore, P. J., Barnett, B. A., Bender, M. L., Bowie, A. R., Tilbrook, B., Petrou, K., Westwood, K. J., Wright, S. W., and Lefevre, D.: The influence of iron and light on net community production in the Subantarctic and Polar Frontal Zones, *Biogeosciences*, 8, 227–237, <https://doi.org/10.5194/bg-8-227-2011>, 2011.
- Cassar, N., Wright, S. W., Thomson, P. G., Trull, T. W., Westwood, K. J., de Salas, M., Davidson, A., Pearce, I., Davies,

- D. M., and Matear, R. J.: The relation of mixed-layer net community production to phytoplankton community composition in the Southern Ocean, *Global Biogeochem. Cycles*, 29, 446–462, <https://doi.org/10.1002/2014gb004936>, 2015.
- Catto, J. L., Jakob, C., Berry, G., and Nicholls, N.: Relating Global Precipitation to Atmospheric Fronts, *Geophys. Res. Lett.*, 39, L10805, <https://doi.org/10.1029/2012GL051736>, 2012.
- Charlson, R. J., Lovelock, J. E., Andreae, M. O., and Warren, S. G.: Oceanic Phytoplankton, Atmospheric Sulphur, Cloud Albedo and Climate, *Nature*, 326, 655–661, <https://doi.org/10.1038/326655a0>, 1987.
- Chelton, D. B., DeSzoeke, R. A., Schlax, M. G., El Naggar, K., and Siwertz, N.: Geographical variability of the first baroclinic Rossby radius of deformation, *J. Phys. Oceanogr.*, 28, 433–460, [https://doi.org/10.1175/1520-0485\(1998\)028<0433:gvotfb>2.0.co;2](https://doi.org/10.1175/1520-0485(1998)028<0433:gvotfb>2.0.co;2), 1998.
- Chen, Q., Sherwen, T., Evans, M., and Alexander, B.: DMS oxidation and sulfur aerosol formation in the marine troposphere: a focus on reactive halogen and multiphase chemistry, *Atmos. Chem. Phys.*, 18, 13617–13637, <https://doi.org/10.5194/acp-18-13617-2018>, 2018.
- Church, M. J., Hutchins, D. A., and Ducklow, H. W.: Limitation of bacterial growth by dissolved organic matter and iron in the Southern Ocean, *Appl. Env. Microb.*, 66, 455–466, <https://doi.org/10.1128/aem.66.2.455-466.2000>, 2000.
- Coale, K. H., Johnson, K. S., Chavez, F. P., Buesseler, K. O., Barber, R. T., Brzezinski, M. A., Cochlan, W. P., Millero, F. J., Falkowski, P. G., Bauer, J. E., et al.: Southern Ocean iron enrichment experiment: carbon cycling in high-and low-Si waters, *Science*, 304, 408–414, <https://doi.org/10.1126/science.1089778>, 2004.
- Cullen, J. J.: The deep chlorophyll maximum: comparing vertical profiles of chlorophyll a, *Can. J. Fish. Aquat. Sci.*, 39, 791–803, <https://doi.org/10.1139/f82-108>, 1982.
- de Boyer Montégut, C., Madec, G., Fischer, A. S., Lazar, A., and Iudicone, D.: Mixed layer depth over the global ocean: An examination of profile data and a profile-based climatology, *J. Geophys. Res.-Oceans*, 109, 1–20, <https://doi.org/10.1029/2004JC002378>, 2004.
- Demsar, U., Harris, P., Brunson, C., Fotheringham, A., and McLoone, S.: Principal Component Analysis on Spatial Data: An Overview, *Ann. Assoc. Am. Geogr.*, 103, 106–128, <https://doi.org/10.1080/00045608.2012.689236>, 2013.
- Denbo, D. W. and Allen, J. S.: Rotary Empirical Orthogonal Function Analysis of Currents near the Oregon Coast, *J. Phys. Oceanogr.*, 14, 35–46, [https://doi.org/10.1175/1520-0485\(1984\)014<0035:reofao>2.0.co;2](https://doi.org/10.1175/1520-0485(1984)014<0035:reofao>2.0.co;2), 1984.
- Derkani, M. H., Alberello, A., Nelli, F., Bennetts, L. G., Hessner, K. G., MacHutchon, K., Reichert, K., Aouf, L., Khan, S., and Toffoli, A.: Wind, waves, and surface currents in the Southern Ocean: observations from the Antarctic Circumnavigation Expedition, *Earth Syst. Sci. Data*, 13, 1189–1209, <https://doi.org/10.5194/essd-13-1189-2021>, 2021.
- Després, V., Huffman, J., Burrows, S. M., Hoose, C., Safatov, A., Buryak, G., Fröhlich-Nowoisky, J., Elbert, W., Andreae, M., Pöschl, U., and Jaenicke, R.: Primary biological aerosol particles in the atmosphere: a review, *Tellus B*, 64, 15598, <https://doi.org/10.3402/tellusb.v64i0.15598>, 2012.
- DeVries, T.: The oceanic anthropogenic CO₂ sink: Storage, air-sea fluxes, and transports over the industrial era, *Global Biogeochem. Cycles*, 28, 631–647, <https://doi.org/10.1002/2013GB004739>, 2014.
- Dragoklenky, E., Crotwell, A., Mund, J., Crotwell, M., and Thoning, K. W.: Atmospheric Methane Dry Air Mole Fractions from the NOAA ESRL Carbon Cycle Cooperative Global Air Sampling Network, 1983–2018, Version: 2019-07, <https://doi.org/10.15138/VNCZ-M766>, 2019.
- Dong, S., Sprintall, J., Gille, S. T., and Talley, L.: Southern Ocean mixed-layer depth from Argo float profiles, *J. Geophys. Res.-Oceans*, 113, C06013, <https://doi.org/10.1029/2006jc004051>, 2008.
- Dong, S., Garzoli, S. L., and Baringer, M.: An assessment of the seasonal mixed layer salinity budget in the Southern Ocean, *J. Geophys. Res.-Oceans*, 114, C12001, <https://doi.org/10.1029/2008JC005258>, 2009.
- Doty, M. S. and Oguri, M.: The island mass effect, *ICES Journal of Marine Science*, 22, 33–37, <https://doi.org/10.1093/icesjms/22.1.33>, 1956.
- Duncan, B. N., Martin, R. V., Staudt, A. C., Yevich, R., and Logan, J. A.: Interannual and Seasonal Variability of Biomass Burning Emissions Constrained by Satellite Observations, *J. Geophys. Res.-Atmos.*, 108, ACH 1-1–ACH 1-22, <https://doi.org/10.1029/2002JD002378>, 2003.
- Dusek, U., Frank, G. P., Hildebrandt, L., Curtius, J., Schneider, J., Walter, S., Chand, D., Drewnick, F., Hings, S., Jung, D., Borrmann, S., and Andreae, M. O.: Size matters more than chemistry for cloud-nucleating ability of aerosol particles, *Science*, 312, 1375–1378, <https://doi.org/10.1126/science.1125261>, 2006.
- Ellwood, M. J., Hutchins, D. A., Lohan, M. C., Milne, A., Nasemann, P., Nodder, S. D., Sander, S. G., Strzepek, R., Wilhelm, S. W., and Boyd, P. W.: Iron Stable Isotopes Track Pelagic Iron Cycling during a Subtropical Phytoplankton Bloom, *P. Natl. Acad. Sci. USA*, 112, E15–E20, <https://doi.org/10.1073/pnas.1421576112>, 2015.
- Engel, A., Endres, S., Galgani, L., and Schartau, M.: Marvelous Marine Microgels: On the Distribution and Impact of Gel-Like Particles in the Oceanic Water-Column, *Front. Marine Sci.*, 7, 405, <https://doi.org/10.3389/fmars.2020.00405>, 2020.
- Eriksen, R., Trull, T. W., Davies, D., Jansen, P., Davidson, A. T., Westwood, K., and van den Enden, R.: Seasonal succession of phytoplankton community structure from autonomous sampling at the Australian Southern Ocean Time Series (SOTS) observatory, *Marine Ecol. Prog. Ser.*, 589, 13–31, <https://doi.org/10.3354/meps12420>, 2018.
- Eveleth, R., Cassar, N., Sherrell, R., Ducklow, H., Meredith, M., Venables, H., Lin, Y., and Li, Z.: Ice melt influence on summertime net community production along the Western Antarctic Peninsula, *Deep-Sea Res. Pt. II*, 139, 89–102, <https://doi.org/10.1016/j.dsr2.2016.07.016>, 2017.
- Falkowski, P. and Kolber, Z.: Variations in chlorophyll fluorescence yields in phytoplankton in the world oceans, *Funct. Plant Biol.*, 22, 341–355, <https://doi.org/10.1071/pp9950341>, 1995.
- Ferracci, V., Heimann, I., Abraham, N. L., Pyle, J. A., and Archibald, A. T.: Global modelling of the total OH reactivity: investigations on the “missing” OH sink and its atmospheric implications, *Atmos. Chem. Phys.*, 18, 7109–7129, <https://doi.org/10.5194/acp-18-7109-2018>, 2018.

- Field, P. R. and Wood, R.: Precipitation and Cloud Structure in Midlatitude Cyclones, *J. Climate*, 20, 233–254, <https://doi.org/10.1175/JCLI3998.1>, 2007.
- Flato, G., Marotzke, J., Abiodun, B., Braconnot, P., Chou, S. C., Collins, W., Cox, P., Driouech, F., Emori, S., Eyring, V., Forest, C., Gleckler, P., Guilyardi, E., Jakob, C., Kattsov, V., Reason, C., and Rummukainen, M.: Evaluation of Climate Models, in: *Climate Change 2013: The Physical Science Basis. Contribution of Working Group I to the Fifth Assessment Report of the Intergovernmental Panel on Climate Change*, edited by Stocker, T. F., Qin, D., Plattner, G.-K., Tignor, M., Allen, S. K., Doschung, J., Nauels, A., Xia, Y., Bex, V., and Midgley, P. M., pp. 741–882, Cambridge University Press, Cambridge, UK, <https://doi.org/10.1017/CBO9781107415324.020>, 2013.
- Fossum, K. N., Ovadnevaite, J., Ceburnis, D., Preißler, J., Snider, J. R., Huang, R.-J., Zuend, A., and O’Dowd, C.: Sea-Spray Regulates Sulfate Cloud Droplet Activation over Oceans, *npj Climate and Atmospheric Science*, 3, 1–6, <https://doi.org/10.1038/s41612-020-0116-2>, 2020.
- Freeman, N. M., Lovenduski, N. S., Munro, D. R., Krumhardt, K. M., Lindsay, K., Long, M. C., and MacLennan, M.: The variable and changing Southern Ocean silicate front: insights from the CESM Large Ensemble, *Global Biogeochem. Cycles*, 32, 752–768, <https://doi.org/10.1029/2017gb005816>, 2018.
- Frölicher, T. L., Sarmiento, J. L., Paynter, D. J., Dunne, J. P., Krasting, J. P., and Winton, M.: Dominance of the Southern Ocean in Anthropogenic Carbon and Heat Uptake in CMIP5 Models, *J. Climate*, 28, 862–886, <https://doi.org/10.1175/JCLI-D-14-00117.1>, 2014.
- Fröhlich-Nowoisky, J., Kampf, C. J., Weber, B., Huffman, J. A., Pöhlker, C., Andreae, M. O., Lang-Yona, N., Burrows, S. M., Gunthe, S. S., Elbert, W., Su, H., Hoor, P., Thines, E., Hoffmann, T., Després, V. R., and Pöschl, U.: Bioaerosols in the Earth system: Climate, health, and ecosystem interactions, *Atmos. Res.*, 182, 346–376, <https://doi.org/10.1016/j.atmosres.2016.07.018>, 2016.
- Gat, J. R.: The Isotopic Composition of Evaporating Waters – Review of the Historical Evolution Leading up to the Craig–Gordon Model, *Isot. Environ. Health S.*, 44, 5–9, <https://doi.org/10.1080/10256010801887067>, 2008.
- GEBCO Compilation Group: GEBCO_2019 Grid – a continuous terrain model of the global oceans and land, available at: <https://www.bodc.ac.uk/resources/inventories/edmed/report/6934/> (last access: 16 November 2021), 2019.
- Gravuer, K., Sullivan, J. J., Williams, P. A., and Duncan, R. P.: Strong human association with plant invasion success for *Trifolium* introductions to New Zealand, *Proc. Nat. Acad. Sci. USA*, 105, 6344–6349, <https://doi.org/10.1073/pnas.0712026105>, 2008.
- Grazioli, J., Genthon, C., Boudevillain, B., Duran-Alarcon, C., Del Guasta, M., Madeleine, J.-B., and Berne, A.: Measurements of precipitation in Dumont d’Urville, Adélie Land, East Antarctica, *The Cryosphere*, 11, 1797–1811, <https://doi.org/10.5194/tc-11-1797-2017>, 2017.
- Gruber, N., Landschützer, P., and Lovenduski, N. S.: The Variable Southern Ocean Carbon Sink, *Annu. Rev. Marine Sci.*, 11, 159–186, <https://doi.org/10.1146/annurev-marine-121916-063407>, pMID: 30212259, 2019.
- Grung, B. and Manne, R.: Missing values in principal component analysis, *Chemometr. Intell. Lab.*, 42, 125–139, [https://doi.org/10.1016/s0169-7439\(98\)00031-8](https://doi.org/10.1016/s0169-7439(98)00031-8), 1998.
- Hamilton, D. S., Lee, L. A., Pringle, K. J., Reddington, C. L., Spracklen, D. V., and Carslaw, K. S.: Occurrence of pristine aerosol environments on a polluted planet, *P. Natl. Acad. Sci. USA*, 111, 18466–18471, <https://doi.org/10.1073/pnas.1415440111>, 2014.
- Hanley, K. E., Belcher, S. E., and Sullivan, P. P.: A Global Climatology of Wind–Wave Interaction, *J. Phys. Oceanogr.*, 40, 1263–1282, <https://doi.org/10.1175/2010JPO4377.1>, 2010.
- Haumann, F. A., Gruber, N., Münnich, M., Frenger, I., and Kern, S.: Sea-Ice Transport Driving Southern Ocean Salinity and Its Recent Trends, *Nature*, 537, 89–92, <https://doi.org/10.1038/nature19101>, 2016.
- Haumann, F. A., Leonard, K., Meredith, M. P., Arrowsmith, C., Gorodetskaya, I. V., Hutchings, J., Lehning, M., Leng, M. J., Stammerjohn, S., Tsukernik, M., and Weber, Y.: Seawater stable isotope sample measurements from the Antarctic Circumnavigation Expedition (ACE), Zenodo, <https://doi.org/10.5281/zenodo.1494915>, 2019.
- Haumann, F. A., Leonard, K., Meredith, M. P., Budéus, G., Gorodetskaya, I. V., Hutchings, J., Lehning, M., Stammerjohn, S., Tsukernik, M., and Weber, Y.: Seawater salinity sample measurements from the Antarctic Circumnavigation Expedition (ACE), Zenodo, <https://doi.org/10.5281/zenodo.1494924>, 2020a.
- Haumann, F. A., Robinson, C., Thomas, J., Hutchings, J., Pina Estany, C., Tarasenko, A., Gerber, F., and Leonard, K.: Physical and biogeochemical oceanography data from underway measurements with an AquaLine Ferrybox during the Antarctic Circumnavigation Expedition (ACE), Zenodo, <https://doi.org/10.5281/zenodo.3660852>, 2020b.
- Haumann, F. A., Thomas, J., Tsukernik, M., and Leonard, K.: Seawater temperature profiles from Expendable Bathythermograph (XBT) probe deployments during the Antarctic Circumnavigation Expedition (ACE), Zenodo, <https://doi.org/10.5281/zenodo.3836648>, 2020c.
- Haumann, F. A., Meredith, M. P., Leonard, K., Leng, M., Arrowsmith, C., and Budéus, G.: The Southern Ocean surface freshwater flux balance and its seawater isotopic constraints, in preparation, 2021.
- Hawkings, J. R., Wadham, J. L., Tranter, M., Raiswell, R., Benning, L. G., Statham, P. J., Tedstone, A., Nienow, P., Lee, K., and Telling, J.: Ice sheets as a significant source of highly reactive nanoparticulate iron to the oceans, *Nat. Commun.*, 5, 1–8, <https://doi.org/10.1038/ncomms4929>, 2014.
- He, X.-C., Tham, Y. J., Dada, L., Wang, M., Finkenzeller, H., Stolzenburg, D., Iyer, S., Simon, M., Kürten, A., Shen, J., Rörup, B., Rissanen, M., Schobesberger, S., Baalbaki, R., Wang, D. S., Koenig, T. K., Jokinen, T., Sarnela, N., Beck, L. J., Almeida, J., Amanatidis, S., Amorim, A., Ataei, F., Baccarini, A., Bertozzi, B., Bianchi, F., Brilke, S., Caudillo, L., Chen, D., Chiu, R., Chu, B., Dias, A., Ding, A., Dommen, J., Duplissy, J., El Haddad, I., Gonzalez Carracedo, L., Granzin, M., Hansel, A., Heinritzi, M., Hofbauer, V., Junninen, H., Kangasluoma, J., Kempainen, D., Kim, C., Kong, W., Krechmer, J. E., Kvashin, A., Laitinen, T., Lamkaddam, H., Lee, C. P., Lehtipalo, K., Leiminger, M., Li, Z., Makhmutov, V., Manninen, H. E., Marie, G., Marten, R., Mathot, S., Mauldin, R. L., Mentler, B., Möhler, O., Müller, T.,

- Nie, W., Onnela, A., Petäjä, T., Pfeifer, J., Philippov, M., Ranjithkumar, A., Saiz-Lopez, A., Salma, I., Scholz, W., Schuchmann, S., Schulze, B., Steiner, G., Stozhkov, Y., Tauber, C., Tomé, A., Thakur, R. C., Väisänen, O., Vazquez-Pufleau, M., Wagner, A. C., Wang, Y., Weber, S. K., Winkler, P. M., Wu, Y., Xiao, M., Yan, C., Ye, Q., Ylisirniö, A., Zauner-Wieczorek, M., Zha, Q., Zhou, P., Flagan, R. C., Curtius, J., Baltensperger, U., Kulmala, M., Kerminen, V.-M., Kurtén, T., Donahue, N. M., Volkamer, R., Kirkby, J., Worsnop, D. R., and Sipilä, M.: Role of Iodine Oxoacids in Atmospheric Aerosol Nucleation, *Science*, 371, 589–595, <https://doi.org/10.1126/science.abe0298>, 2021.
- Hennessey, J. P.: Some Aspects of Wind Power Statistics, *J. Appl. Meteorol. Climatol.*, 16, 119–128, [https://doi.org/10.1175/1520-0450\(1977\)016<0119:SAOWPS>2.0.CO;2](https://doi.org/10.1175/1520-0450(1977)016<0119:SAOWPS>2.0.CO;2), 1977.
- Henry, T., Robinson, C., Haumann, F. A., Thomas, J., Hutchings, J., Schuback, N., Tsukernik, M., and Leonard, K.: Physical and biogeochemical oceanography data from Conductivity, Temperature, Depth (CTD) rosette deployments during the Antarctic Circumnavigation Expedition (ACE), Zenodo, <https://doi.org/10.5281/zenodo.3813646>, 2020.
- Hobbs, P. V.: Organization and structure of clouds and precipitation on the mesoscale and microscale in cyclonic storms, *Rev. Geophys.*, 16, 741–755, <https://doi.org/10.1029/RG016i004p00741>, 1978.
- Hoffmann, E. H., Tilgner, A., Schrödner, R., Bräuer, P., Wolke, R., and Herrmann, H.: An Advanced Modeling Study on the Impacts and Atmospheric Implications of Multiphase Dimethyl Sulfide Chemistry, *P. Natl. Acad. Sci. USA*, 113, 11776–11781, <https://doi.org/10.1073/pnas.1606320113>, 2016.
- Holland, P. R. and Kwok, R.: Wind-driven trends in Antarctic sea-ice drift, *Nat. Geosci.*, 5, 872–875, <https://doi.org/10.1038/ngeo1627>, 2012.
- Hoppel, W. and Frick, G.: Submicron aerosol size distributions measured over the tropical and South Pacific, *Atmos. Environ. A*, 24, 64–659, [https://doi.org/10.1016/0960-1686\(90\)90020-N](https://doi.org/10.1016/0960-1686(90)90020-N), 1990.
- Hotelling, H.: Analysis of a complex of statistical variables into principal components, *J. Educ. Psychol.*, 24, 498–520, <https://doi.org/10.1037/h0070888>, 1933.
- Ingalls, A. E., Liu, Z., and Lee, C.: Seasonal trends in the pigment and amino acid compositions of sinking particles in biogenic CaCO₃ and SiO₂ dominated regions of the Pacific sector of the Southern Ocean along 170° W, *Deep-Sea Res. Pt. I*, 53, 836–859, <https://doi.org/10.1016/j.dsr.2006.01.004>, 2006.
- Ishikawa, A., Wright, S., Enden, R. V. D., Davidson, A. T., and Marchant, H.: Abundance, Size Structure and Community Composition of Phytoplankton in the Southern Ocean in the Austral Summer 1999/2000, *Polar Biosci.*, 15, 11–26, <https://doi.org/10.15094/00006180>, 2002.
- Jacobs, S. S.: Freshening of the Ross Sea During the Late 20th Century, *Science*, 297, 386–389, <https://doi.org/10.1126/science.1069574>, 2002.
- Janssen, D. J., Sieber, M., Ellwood, M. J., Conway, T. M., Barrett, P. M., Chen, X., de Souza, G. F., Hassler, C. S., and Jaccard, S. L.: Trace metal and nutrient dynamics across broad biogeochemical gradients in the Indian and Pacific sectors of the Southern Ocean, *Marine Chem.*, 221, 103773, <https://doi.org/10.1016/j.marchem.2020.103773>, 2020.
- Jefferson, A., Tanner, D. J., Eisele, F. L., and Berresheim, H.: Sources and Sinks of H₂SO₄ in the Remote Antarctic Marine Boundary Layer, *J. Geophys. Res.-Atmos.*, 103, 1639–1645, <https://doi.org/10.1029/97JD01212>, 1998.
- Jickells, T. D., An, Z. S., Andersen, K. K., Baker, A. R., Bergametti, G., Brooks, N., Cao, J. J., Boyd, P. W., Duce, R. A., Hunter, K. A., Kawahata, H., Kubilay, N., laRoche, J., Liss, P. S., Mahowald, N., Prospero, J. M., Ridgwell, A. J., Tegen, I., and Torres, R.: Global iron connections between desert dust, ocean biogeochemistry, and climate, *Science*, 308, 67–71, <https://doi.org/10.1126/science.1105959>, 2005.
- Jullien, N., Vignon, É., Sprenger, M., Aemisegger, F., and Berne, A.: Synoptic conditions and atmospheric moisture pathways associated with virga and precipitation over coastal Adélie Land in Antarctica, *The Cryosphere*, 14, 1685–1702, <https://doi.org/10.5194/tc-14-1685-2020>, 2020.
- Kanji, Z. A., Ladino, L. A., Wex, H., Boose, Y., Burkert-Kohn, M., Cziczo, D. J., and Krämer, M.: Overview of ice nucleating particles, *Meteorol. Monogr.*, 58, 1–1, <https://doi.org/10.1175/AMSMONOGRAPHS-D-16-0006.1>, 2017.
- Khalil, M. A. K. and Rasmussen, R. A.: Sources, Sinks, and Seasonal Cycles of Atmospheric Methane, *J. Geophys. Res.-Oceans*, 88, 5131–5144, <https://doi.org/10.1029/JC088iC09p05131>, 1983.
- Khalil, M. A. K. and Rasmussen, R. A.: The Global Cycle of Carbon Monoxide: Trends and Mass Balance, *Chemosphere*, 20, 227–242, [https://doi.org/10.1016/0045-6535\(90\)90098-E](https://doi.org/10.1016/0045-6535(90)90098-E), 1990.
- Kinsey, J. D., Kieber, D. J., and Neale, P. J.: Effects of iron limitation and UV radiation on *Phaeocystis* antarctica growth and dimethylsulfoniopropionate, dimethylsulfoxide and acrylate concentrations, *Environ. Chem.*, 13, 195–211, <https://doi.org/10.1071/en14275>, 2016.
- Kirchman, D. L., Morán, X. A. G., and Ducklow, H.: Microbial growth in the polar oceans – role of temperature and potential impact of climate change, *Nat. Rev. Microbiol.*, 7, 451–459, <https://doi.org/10.1038/nrmicro2115>, 2009.
- Kolstad, E. W.: Higher Ocean Wind Speeds during Marine Cold Air Outbreaks, *Q. J. Roy. Meteor. Soc.*, 143, 2084–2092, <https://doi.org/10.1002/qj.3068>, 2017.
- Korhonen, H., Carslaw, K. S., Spracklen, D. V., Mann, G. W., and Woodhouse, M. T.: Influence of Oceanic Dimethyl Sulfide Emissions on Cloud Condensation Nuclei Concentrations and Seasonality over the Remote Southern Hemisphere Oceans: A Global Model Study, *J. Geophys. Res.-Atmos.*, 113, D15204, <https://doi.org/10.1029/2007JD009718>, 2008.
- Krause, G. H. and Jahns, P.: Non-photochemical energy dissipation determined by chlorophyll fluorescence quenching: characterization and function, in: *Chlorophyll a fluorescence*, 463–495, Springer, https://doi.org/10.1007/978-1-4020-3218-9_18, 2004.
- Lana, A., Bell, T. G., Simó, R., Vallina, S. M., Ballabrera-Poy, J., Kettle, A. J., Dachs, J., Bopp, L., Saltzman, E. S., Stefels, J., Johnson, J. E., and Liss, P. S.: An updated climatology of surface dimethylsulfide concentrations and emission fluxes in the global ocean, *Global Biogeochem. Cycles*, 25, GB1004, <https://doi.org/10.1029/2010gb003850>, 2011.
- Landwehr, S., Volpi, M., Derkani, M. H., Nelli, F., Alberello, A., Toffoli, A., Gysel-Beer, M., Modini, R. L., and Schmale, J.: Sea State and Boundary Layer Stability Limit Sea

- Spray Aerosol Lifetime over the Southern Ocean, ESSOAR, <https://doi.org/10.1002/essoar.10504508.1>, 2020.
- Lannuzel, D., Schoemann, V., De Jong, J., Chou, L., Delille, B., Becquevort, S., and Tison, J.-L.: Iron study during a time series in the western Weddell pack ice, *Marine Chem.*, 108, 85–95, <https://doi.org/10.1016/j.marchem.2007.10.006>, 2008.
- Lannuzel, D., Schoemann, V., De Jong, J., Pasquer, B., Van der Merwe, P., Masson, F., Tison, J.-L., and Bowie, A.: Distribution of dissolved iron in Antarctic sea ice: Spatial, seasonal, and inter-annual variability, *J. Geophys. Res.-Bioge.*, 115, G03022, <https://doi.org/10.1029/2009jg001031>, 2010.
- Lannuzel, D., Vancoppenolle, M., van der Merwe, P., de Jong, J., Meinert, K., Grotti, M., Nishioka, J., and Schoemann, V.: Iron in Sea Ice: Review and New Insights, *Elementa*, 4, 000130, <https://doi.org/10.12952/journal.elementa.000130>, 2016.
- Lee, D., Lee, W., Lee, Z., and Pawitan, Z.: Super-sparse principal component analyses for high-throughput genomic data, *BMC Bioinformatics*, 11, 296, <https://doi.org/10.1186/1471-2105-11-296>, 2010.
- Lee, L. A., Pringle, K. J., Reddington, C. L., Mann, G. W., Stier, P., Spracklen, D. V., Pierce, J. R., and Carslaw, K. S.: The magnitude and causes of uncertainty in global model simulations of cloud condensation nuclei, *Atmos. Chem. Phys.*, 13, 8879–8914, <https://doi.org/10.5194/acp-13-8879-2013>, 2013.
- Lewis, E. R. and Schwartz, S. E.: Sea Salt Aerosol Production: Mechanisms, Methods, Measurements and Models ; a Critical Review, no. 152 in *Geophysical Monograph*, American Geophysical Union, Washington, D.C., <https://doi.org/10.1029/gm152>, 2004.
- Li, J., Min, Q., Peng, Y., Sun, Z., and Zhao, J.-Q.: Accounting for Dust Aerosol Size Distribution in Radiative Transfer, *J. Geophys. Res.-Atmos.*, 120, 6537–6550, <https://doi.org/10.1002/2015JD023078>, 2015.
- Li, Z., Safo, S. E., and Long, Q.: Incorporating biological information in sparse principal component analysis with application to genomic data, *BMC Bioinformatics*, 18, <https://doi.org/10.1186/s12859-017-1740-7>, 2017.
- Llort, J., Lévy, M., Sallée, J.-B., and Tagliabue, A.: Onset, intensification, and decline of phytoplankton blooms in the Southern Ocean, *ICES Journal of Marine Science*, 72, 1971–1984, <https://doi.org/10.1093/icesjms/fsv053>, 2015.
- Lourey, M. J. and Trull, T. W.: Seasonal nutrient depletion and carbon export in the Subantarctic and Polar Frontal Zones of the Southern Ocean south of Australia, *J. Geophys. Res.-Oceans*, 106, 31463–31487, <https://doi.org/10.1029/2000jc000287>, 2001.
- Lucas, D. D. and Prinn, R. G.: Mechanistic Studies of Dimethylsulfide Oxidation Products Using an Observationally Constrained Model, *J. Geophys. Res.-Atmos.*, 107, ACH 12-1–ACH 12-26, <https://doi.org/10.1029/2001JD000843>, 2002.
- Maahn, M. and Kollias, P.: Improved Micro Rain Radar snow measurements using Doppler spectra post-processing, *Atmos. Meas. Tech.*, 5, 2661–2673, <https://doi.org/10.5194/amt-5-2661-2012>, 2012.
- Mairal, J., Back, F., Ponce, J., and Sapiro, G.: Online dictionary learning for sparse coding, in: *International Conference on Machine Learning (ICML)*, Proceedings of the 26th Annual International Conference on Machine Learning, Association for Computing Machinery, Montreal, Quebec, Canada, <https://doi.org/10.1145/1553374.1553463>, 2009.
- Marinov, I., Gnanadesikan, A., Toggweiler, J. R., and Sarmiento, J. L.: The Southern Ocean Biogeochemical Divide, *Nature*, 441, 964–967, <https://doi.org/10.1038/nature04883>, 2006.
- Mason, R. H., Si, M., Li, J., Chou, C., Dickie, R., Toom-Sauntry, D., Pöhlker, C., Yakobi-Hancock, J. D., Ladino, L. A., Jones, K., Leaitch, W. R., Schiller, C. L., Abbatt, J. P. D., Huffman, J. A., and Bertram, A. K.: Ice nucleating particles at a coastal marine boundary layer site: correlations with aerosol type and meteorological conditions, *Atmos. Chem. Phys.*, 15, 12547–12566, <https://doi.org/10.5194/acp-15-12547-2015>, 2015.
- McClure-Begley, A., Petropavlovskikh, I., Oltmans, S., and ESRL, N.: Earth System Research Laboratory Surface Ozone Measurements, Version 1, NOAA National Centers for Environmental Information, <https://doi.org/10.7289/V57P8WBF>, 2013.
- McCluskey, C. S., Ovadnevaite, J., Rinaldi, M., Atkinson, J., Belosi, F., Ceburnis, D., Marullo, S., Hill, T. C. J., Lohmann, U., Kanji, Z. A., O’Dowd, C., Kreidenweis, S. M., and DeMott, P. J.: Marine and terrestrial organic ice-nucleating particles in pristine marine to continentally influenced Northeast Atlantic air masses, *J. Geophys. Res.-Atmos.*, 123, 6196–6212, <https://doi.org/10.1029/2017jd028033>, 2018.
- McDougall, T. and Barker, P.: Getting started with TEOS-10 and the Gibbs Seawater (GSW) Oceanographic Toolbox, Tech. rep., available at: http://www.teos-10.org/pubs/gsw/v3_04/pdf/Getting_Started.pdf (last access: 5 February 2021), 2011.
- Meier, W., Fetterer, F., Savoie, M., Mallory, S., Duerr, R., and Stroeve, J.: NOAA/NSIDC Climate Data Record of passive microwave sea ice concentration, version 2. 1979–2018, NSIDC, <https://doi.org/10.7265/N55M63M1>, 2013.
- Meylan, M. H., Bennetts, L. G., Mosig, J. E. M., Rogers, W. E., Doble, M. J., and Peter, M. A.: Dispersion Relations, Power Laws, and Energy Loss for Waves in the Marginal Ice Zone, *J. Geophys. Res.-Oceans*, 123, 3322–3335, <https://doi.org/10.1002/2018JC013776>, 2018.
- Moallemi, A., Landwehr, S., Robinson, C. M., Simó, R., Zamanillo, M., Chen, G., Baccarini, A., Schnaiter, M., Henning, S., Modini, R. L., Gysel-Beer, M., and Schmale, J.: Sources, Occurrence and Characteristics of Fluorescent Biological Aerosol Particles Measured over the Pristine Southern Ocean, ESSOAR, <https://doi.org/10.1029/2021jd034811>, 2021.
- Modini, R. L., Frossard, A. A., Ahlm, L., Russell, L. M., Corrigan, C. E., Roberts, G. C., Hawkins, L. N., Schroder, J. C., Bertram, A. K., Zhao, R., Lee, A. K. Y., Abbatt, J. P. D., Lin, J., Nenes, A., Wang, Z., Wonaschütz, A., Sorooshian, A., Noone, K. J., Jonsen, H., Seinfeld, J. H., Toom-Sauntry, D., Macdonald, A. M., and Leaitch, W. R.: Primary Marine Aerosol-Cloud Interactions off the Coast of California, *J. Geophys. Res.-Atmos.*, 120, 4282–4303, <https://doi.org/10.1002/2014JD022963>, 2015.
- Monahan, E. C., Spiel, D. E., and Davidson, K. L.: A Model of Marine Aerosol Generation Via Whitecaps and Wave Disruption, in: *Oceanic Whitecaps*, edited by: Monahan, E. C. and Niocaill, G. M., Springer Netherlands, Dordrecht, 2, 167–174, https://doi.org/10.1007/978-94-009-4668-2_16, 1986.
- Mongin, M., Molina, E., and Trull, T. W.: Seasonality and scale of the Kerguelen plateau phytoplankton bloom: A remote sensing and modeling analysis of the influence of natural iron fertilization in the Southern Ocean, *Deep-Sea Res. Pt. II*, 55, 880–892, <https://doi.org/10.1016/j.dsr2.2007.12.039>, 2008.

- Moore, C. M., Lucas, M. I., Sanders, R., and Davidson, R.: Basin-scale variability of phytoplankton bio-optical characteristics in relation to bloom state and community structure in the Northeast Atlantic, *Deep-Sea Res. Pt. I*, 52, 401–419, <https://doi.org/10.1016/j.dsr.2004.09.003>, 2005.
- Moore, C. M., Mills, M. M., Arrigo, K. R., Berman-Frank, I., Bopp, L., Boyd, P. W., Galbraith, E. D., Geider, R. J., Guieu, C., Jaccard, S. L., Jickells, T. D., Roche, J. L., Lenton, T. M., Mahowald, N. M., Marañón, E., Marinov, I., Moore, J. K., Nakatsuka, T., Oschlies, A., Saito, M. A., Thingstad, T. F., Tsuda, A., and Ulloa, O.: Processes and patterns of oceanic nutrient limitation, *Nat. Geosci.*, 6, 701–710, <https://doi.org/10.1038/ngeo1765>, 2013.
- Moreau, S., Boyd, P. W., and Strutton, P. G.: Remote Assessment of the Fate of Phytoplankton in the Southern Ocean Sea-Ice Zone, *Nat. Commun.*, 11, 3108, <https://doi.org/10.1038/s41467-020-16931-0>, 2020.
- Murray, B. J., O’Sullivan, D., Aitkenison, J. D., and Webb, M. E.: Ice nucleation by particles immersed in super-cooled cloud droplets, *Chem. Soc. Rev.*, 41, 6519–6554, <https://doi.org/10.1039/C2CS35200A>, 2012.
- Nicholson, S.-A., Lévy, M., Lloret, J., Swart, S., and Monteiro, P. M. S.: Investigation into the Impact of Storms on Sustaining Summer Primary Productivity in the Sub-Antarctic Ocean, *Geophys. Res. Lett.*, 43, 9192–9199, <https://doi.org/10.1002/2016GL069973>, 2016.
- Orsi, A. H., Whitworth, T., and Nowlin, W. D.: On the meridional extent and fronts of the Antarctic Circumpolar Current, *Deep-Sea Res. Pt. I*, 42, 641–673, [https://doi.org/10.1016/0967-0637\(95\)00021-W](https://doi.org/10.1016/0967-0637(95)00021-W), 1995.
- O’Sullivan, D., Adams, M., Tarn, M. D., Harrison, A. D., Vergara-Temprado, J., Porter, G. C., Holden, M. A., Sanchez-Marroquin, A., Carotenuto, F., Whale, T. F., et al.: Contributions of biogenic material to the atmospheric ice-nucleating particle population in North Western Europe, *Sci. Rep.-UK*, 8, 1–9, <https://doi.org/10.1038/s41598-018-31981-7>, 2018.
- Papritz, L., Pfahl, S., Rudeva, I., Simmonds, I., Sodemann, H., and Wernli, H.: The Role of Extratropical Cyclones and Fronts for Southern Ocean Freshwater Fluxes, *J. Climate*, 27, 6205–6224, <https://doi.org/10.1175/JCLI-D-13-00409.1>, 2014.
- Pedregosa, F., Varoquaux, G., Gramfort, A., Michel, V., Thirion, B., Grisel, O., Blondel, M., Prettenhofer, P., Weiss, R., Dubourg, V., Vanderplas, J., Passos, A., Cournapeau, D., Brucher, M., Perrot, M., and Duchesnay, E.: Scikit-learn: Machine Learning in Python, *J. Mac. Learn. Res.h*, 12, 2825–2830, 2011.
- Peng, G., Meier, W. N., Scott, D. J., and Savoie, M. H.: A long-term and reproducible passive microwave sea ice concentration data record for climate studies and monitoring, *Earth Syst. Sci. Data*, 5, 311–318, <https://doi.org/10.5194/essd-5-311-2013>, 2013.
- Perissinotto, R., Laubscher, R., and McQuaid, C.: Marine productivity enhancement around Bouvet and the South Sandwich Islands (Southern Ocean), *Marine Ecology-Progress Series*, 88, 41–41, <https://doi.org/10.3354/meps088041>, 1992.
- Petron, G., Crotwell, A. M., Dlugokencky, E., and Mund, J. W.: Atmospheric Carbon Monoxide Dry Air Mole Fractions from the NOAA ESRL Carbon Cycle Cooperative Global Air Sampling Network, 1988–2018, Version: 2019-08, <https://doi.org/10.15138/33bv-s284>, 2019.
- Petters, M. D. and Kreidenweis, S. M.: A single parameter representation of hygroscopic growth and cloud condensation nucleus activity, *Atmos. Chem. Phys.*, 7, 1961–1971, <https://doi.org/10.5194/acp-7-1961-2007>, 2007.
- Pfahl, S. and Sodemann, H.: What controls deuterium excess in global precipitation?, *Clim. Past*, 10, 771–781, <https://doi.org/10.5194/cp-10-771-2014>, 2014.
- Pierce, J. R. and Adams, P. J.: Global Evaluation of CCN Formation by Direct Emission of Sea Salt and Growth of Ultrafine Sea Salt, *J. Geophys. Res.-Atmos.*, 111, D06203, <https://doi.org/10.1029/2005JD006186>, 2006.
- Pollard, R., Lucas, M., and Read, J.: Physical controls on biogeochemical zonation in the Southern Ocean, *Deep-Sea Res. Pt. II*, 49, 3289–3305, [https://doi.org/10.1016/s0967-0645\(02\)00084-x](https://doi.org/10.1016/s0967-0645(02)00084-x), 2002.
- Pozzer, A., Pollmann, J., Taraborrelli, D., Jöckel, P., Helmig, D., Tans, P., Hueber, J., and Lelieveld, J.: Observed and simulated global distribution and budget of atmospheric C₂-C₅ alkanes, *Atmos. Chem. Phys.*, 10, 4403–4422, <https://doi.org/10.5194/acp-10-4403-2010>, 2010.
- Prather, K. A., Bertram, T. H., Grassian, V. H., Deane, G. B., Stokes, M. D., DeMott, P. J., Aluwihare, L. I., Palenik, B. P., Azam, F., Seinfeld, J. H., Moffet, R. C., Molina, M. J., Cappa, C. D., Geiger, F. M., Roberts, G. C., Russell, L. M., Ault, A. P., Baltrusaitis, J., Collins, D. B., Corrigan, C. E., Cuadrado-Rodriguez, L. A., Ebben, C. J., Forestieri, S. D., Guasco, T. L., Hersey, S. P., Kim, M. J., Lambert, W. F., Modini, R. L., Mui, W., Pedler, B. E., Ruppel, M. J., Ryder, O. S., Schoepp, N. G., Sullivan, R. C., and Zhao, D.: Bringing the ocean into the laboratory to probe the chemical complexity of sea spray aerosol, *P. Natl. Acad. Sci. USA*, 110, 7550–7555, <https://doi.org/10.1073/pnas.1300262110>, 2013.
- Prend, C. J., Gille, S. T., Talley, L. D., Mitchell, B. G., Rosso, I., and Mazloff, M. R.: Physical Drivers of Phytoplankton Bloom Initiation in the Southern Ocean’s Scotia Sea, *J. Geophys. Res.-Oceans*, 124, 5811–5826, <https://doi.org/10.1029/2019JC015162>, 2019.
- Quinn, P. K. and Bates, T. S.: The case against climate regulation via oceanic phytoplankton sulphur emissions, *Nature*, 480, 51–56, <https://doi.org/10.1038/nature10580>, 2011.
- Quinn, P. K., Collins, D. B., Grassian, V. H., Prather, K. A., and Bates, T. S.: Chemistry and Related Properties of Freshly Emitted Sea Spray Aerosol, *Chem. Rev.*, 115, 4383–4399, <https://doi.org/10.1021/cr500713g>, 2015.
- Quinn, P. K., Coffman, D. J., Johnson, J. E., Upchurch, L. M., and Bates, T. S.: Small Fraction of Marine Cloud Condensation Nuclei Made up of Sea Spray Aerosol, *Nat. Geoscience*, 10, 674–679, <https://doi.org/10.1038/ngeo3003>, 2017.
- Raes, F., Van Dingenen, R., Vignati, E., Wilson, J., Putaud, J. P., Seinfeld, J. H., and Adams, P.: Formation and cycling of aerosols in the global troposphere, *Atmos. Environ.*, 34, 4215–4240, [https://doi.org/10.1016/s1352-2310\(00\)00239-9](https://doi.org/10.1016/s1352-2310(00)00239-9), 2000.
- Ren, L., Speer, K., and Chassignet, E. P.: The Mixed Layer Salinity Budget and Sea Ice in the Southern Ocean, *J. Geophys. Res.-Oceans*, 116, C08031, <https://doi.org/10.1029/2010JC006634>, 2011.
- Renfrew, I. A. and Moore, G. W. K.: An Extreme Cold-Air Outbreak over the Labrador Sea: Roll Vortices and Air–Sea Interaction, *Mon. Weather Rev.*, 127, 2379–2394, [https://doi.org/10.1175/1520-0493\(1999\)127<2379:AECAOO>2.0.CO;2](https://doi.org/10.1175/1520-0493(1999)127<2379:AECAOO>2.0.CO;2), 1999.

- Reynolds, R. W., Smith, T. M., Liu, C., Chelton, D. B., Casey, K. S., and Schlax, M. G.: Daily high-resolution-blended analyses for sea surface temperature, *J. Climate*, 20, 5473–5496, <https://doi.org/10.1175/2007JCLI1824.1>, 2007.
- Rintoul, S. R.: The Global Influence of Localized Dynamics in the Southern Ocean, *Nature*, 558, 209–218, <https://doi.org/10.1038/s41586-018-0182-3>, 2018.
- Rodríguez-Ros, P., Cortés, P., Robinson, C. M., Nunes, S., Hassler, C., Royer, S.-J., Estrada, M., Sala, M. M., and Simó, R.: Distribution and Drivers of Marine Isoprene Concentration across the Southern Ocean, *Atmosphere*, 11, 556, <https://doi.org/10.3390/atmos11060556>, 2020.
- Rodríguez-Ros, P., Galí, M., Cortés, P., Robinson, C. M., Antoine, D., Wohl, C., Yang, M., and Simó, R.: Remote Sensing Retrieval of Isoprene Concentrations in the Southern Ocean, *Geophys. Res. Lett.*, 47, e2020GL087888, <https://doi.org/10.1029/2020GL087888>, 2020.
- Saiz-Lopez, A., Plane, J. M. C., Baker, A. R., Carpenter, L. J., von Glasow, R., Gómez Martín, J. C., McFiggans, G., and Saunders, R. W.: Atmospheric Chemistry of Iodine, *Chem. Rev.*, 112, 1773–1804, <https://doi.org/10.1021/cr200029u>, 2012.
- Sarmiento, J. L., Gruber, N., Brzezinski, M. A., and Dunne, J. P.: High-Latitude Controls of Thermocline Nutrients and Low Latitude Biological Productivity, *Nature*, 427, 56–60, <https://doi.org/10.1038/nature02127>, 2004.
- Schlosser, E., Haumann, F. A., and Raphael, M. N.: Atmospheric influences on the anomalous 2016 Antarctic sea ice decay, *The Cryosphere*, 12, 1103–1119, <https://doi.org/10.5194/tc-12-1103-2018>, 2018.
- Schmale, J., Schneider, J., Nemitz, E., Tang, Y. S., Dragosits, U., Blackall, T. D., Trathan, P. N., Phillips, G. J., Sutton, M., and Braban, C. F.: Sub-Antarctic marine aerosol: dominant contributions from biogenic sources, *Atmos. Chem. Phys.*, 13, 8669–8694, <https://doi.org/10.5194/acp-13-8669-2013>, 2013.
- Schmale, J., Henning, S., Henzing, B., Keskinen, H., Sellegri, K., Ovadnevaite, J., Bougiatioti, A., Kalivitis, N., Stavroulas, I., Jefferson, A., Park, M., Schlag, P., Kristensson, A., Iwamoto, Y., Pringle, K., Reddington, C., Aalto, P., Äijälä, M., Baltensperger, U., Bialek, J., Birmili, W., Bukowiecki, N., Ehn, M., Fjæraa, A. M., Fiebig, M., Frank, G., Fröhlich, R., Fru-mau, A., Furuya, M., Hammer, E., Heikkinen, L., Herrmann, E., Holzinger, R., Hyono, H., Kanakidou, M., Kiendler-Scharr, A., Kinouchi, K., Kos, G., Kulmala, M., Mihalopoulos, N., Motos, G., Nenes, A., O’Dowd, C., Paramonov, M., Petäjä, T., Picard, D., Poulain, L., Prévôt, A. S. H., Slowik, J., Sonntag, A., Swietlicki, E., Svenningsson, B., Tsurumaru, H., Wiedensohler, A., Wittbom, C., Ogren, J. A., Matsuki, A., Yum, S. S., Myhre, C. L., Carslaw, K., Stratmann, F., and Gysel, M.: Collocated observations of cloud condensation nuclei, particle size distributions, and chemical composition, *Sci. Data*, 4, 170003, <https://doi.org/10.1038/sdata.2017.3>, 2017.
- Schmale, J., Baccarini, A., Thurnherr, I., Henning, S., Efrain, A., Regayre, L., Bolas, C., Hartmann, M., Welti, A., Lehtipalo, K., Aemisegger, F., Tatzelt, C., Landwehr, S., Modini, R. L., Tummou, F., Johnson, J. S., Harris, N., Schnaiter, M., Toffoli, A., Derkani, M., Bukowiecki, N., Stratmann, F., Dommen, J., Baltensperger, U., Wernli, H., Rosenfeld, D., Gysel-Beer, M., and Carslaw, K. S.: Overview of the Antarctic Circumnavigation Expedition: Study of Preindustrial-like Aerosols and Their Climate Effects (ACE-SPACE), *B. Am. Meteorol. Soc.*, 100, 2260–2283, <https://doi.org/10.1175/BAMS-D-18-0187.1>, 2019.
- Schoemann, V., Becquevort, S., Stefels, J., Rousseau, V., and Lancelot, C.: Phaeocystis blooms in the global ocean and their controlling mechanisms: a review, *J. Sea Res.*, 53, 43–66, <https://doi.org/10.1016/j.seares.2004.01.008>, 2005.
- Seinfeld, J. H. and Pandis, S. N.: *Atmospheric Chemistry and Physics: From Air Pollution to Climate Change*, vol. 51, John Wiley, New York, Chichester, Weinheim, Brisbane, Singapore, Toronto, 3rd edn., <https://doi.org/10.1063/1.882420>, 2016.
- Servettaz, A. P. M., Orsi, A. J., Curran, M. A. J., Moy, A. D., Landais, A., Agosta, C., Winton, V. H. L., Touzeau, A., McConnell, J. R., Werner, M., and Baroni, M.: Snowfall and Water Stable Isotope Variability in East Antarctica Controlled by Warm Synoptic Events, *J. Geophys. Res.-Atmos.*, 125, e2020JD032863, <https://doi.org/10.1029/2020JD032863>, 2020.
- Shuman, F. R. and Lorenzen, C. J.: Quantitative degradation of chlorophyll by a marine herbivore 1, *Limnol. Oceanogr.*, 20, 580–586, <https://doi.org/10.4319/lo.1975.20.4.0580>, 1975.
- Simmonds, I., Keay, K., and Lim, E.-P.: Synoptic Activity in the Seas around Antarctica, *Mon. Weather Rev.*, 131, 272–288, [https://doi.org/10.1175/1520-0493\(2003\)131<0272:SAITSA>2.0.CO;2](https://doi.org/10.1175/1520-0493(2003)131<0272:SAITSA>2.0.CO;2), 2003.
- Sipilä, M., Sarnela, N., Jokinen, T., Henschel, H., Junninen, H., Kontkanen, J., Richters, S., Kangasluoma, J., Franchin, A., Peräkylä, O., Rissanen, M. P., Ehn, M., Vehkamäki, H., Kurten, T., Berndt, T., Petäjä, T., Worsnop, D., Ceburnis, D., Kerminen, V.-M., Kulmala, M., and O’Dowd, C.: Molecular-Scale Evidence of Aerosol Particle Formation via Sequential Addition of HIO 3, *Nature*, 537, 532–534, <https://doi.org/10.1038/nature19314>, 2016.
- Squire, V. A.: Ocean Wave Interactions with Sea Ice: A Reappraisal, *Annu. Rev. Fluid Mech.*, 52, 37–60, <https://doi.org/10.1146/annurev-fluid-010719-060301>, 2020.
- Stemmler, I., Hense, I., and Quack, B.: Marine sources of bromoform in the global open ocean – global patterns and emissions, *Biogeosciences*, 12, 1967–1981, <https://doi.org/10.5194/bg-12-1967-2015>, 2015.
- Suggett, D. J., Moore, C. M., Hickman, A. E., and Geider, R. J.: Interpretation of fast repetition rate (FRR) fluorescence: signatures of phytoplankton community structure versus physiological state, *Marine Ecol. Prog. Ser.*, 376, 1–19, <https://doi.org/10.3354/meps07830>, 2009.
- Swart, S., Gille, S. T., Delille, B., Josey, S., Mazloff, M., Newman, L., Thompson, A. F., Thomson, J., Ward, B., du Plessis, M. D., Kent, E. C., Girton, J., Gregor, L., Heil, P., Hyder, P., Pezzi, L. P., de Souza, R. B., Tamsitt, V., Weller, R. A., and Zappa, C. J.: Constraining Southern Ocean Air-Sea-Ice Fluxes Through Enhanced Observations, *Front. Marine Sci.*, 6, 421, <https://doi.org/10.3389/fmars.2019.00421>, 2019.
- Tagliabue, A., Bowie, A. R., Boyd, P. W., Buck, K. N., Johnson, K. S., and Saito, M. A.: The Integral Role of Iron in Ocean Biogeochemistry, *Nature*, 543, 51–59, <https://doi.org/10.1038/nature21058>, 2017.
- Talley, L.: Closure of the Global Overturning Circulation Through the Indian, Pacific, and Southern Oceans: Schematics and Transports, *Oceanography*, 26, 80–97, <https://doi.org/10.5670/oceanog.2013.07>, 2013.

- Tamsitt, V., Abernathey, R. P., Mazloff, M. R., Wang, J., and Talley, L. D.: Transformation of Deep Water Masses Along Lagrangian Upwelling Pathways in the Southern Ocean, *J. Geophys. Res.-Oceans*, 123, 1994–2017, <https://doi.org/10.1002/2017JC013409>, 2018.
- Té, Y., Jeseck, P., Franco, B., Mahieu, E., Jones, N., Paton-Walsh, C., Griffith, D. W. T., Buchholz, R. R., Hadji-Lazaro, J., Hurtmans, D., and Janssen, C.: Seasonal variability of surface and column carbon monoxide over the megacity Paris, high-altitude Jungfraujoch and Southern Hemispheric Wollongong stations, *Atmos. Chem. Phys.*, 16, 10911–10925, <https://doi.org/10.5194/acp-16-10911-2016>, 2016.
- Teeter, L., Hamme, R. C., Ianson, D., and Bianucci, L.: Accurate Estimation of Net Community Production From O₂/Ar Measurements, *Global Biogeochem. Cycles*, 32, 1163–1181, <https://doi.org/10.1029/2017GB005874>, 2018.
- Thomas, J. and Pina Estany, C.: Quality-checked, one-minute resolution cruise track of the Antarctic Circumnavigation Expedition (ACE) undertaken during the austral summer of 2016/2017, Zenodo, <https://doi.org/10.5281/zenodo.3483166>, 2019.
- Thorpe, S. A.: An introduction to ocean turbulence, vol. 10, Cambridge University Press, Cambridge, <https://doi.org/10.1017/cbo9780511801198>, 2007.
- Thurnherr, I., Kozachek, A., Graf, P., Weng, Y., Bolshiyarov, D., Landwehr, S., Pfahl, S., Schmale, J., Sodemann, H., Steen-Larsen, H. C., Toffoli, A., Wernli, H., and Aemisegger, F.: Meridional and vertical variations of the water vapour isotopic composition in the marine boundary layer over the Atlantic and Southern Ocean, *Atmos. Chem. Phys.*, 20, 5811–5835, <https://doi.org/10.5194/acp-20-5811-2020>, 2020.
- Thurnherr, I., Hartmuth, K., Jansing, L., Gehring, J., Boettcher, M., Gorodetskaya, I., Werner, M., Wernli, H., and Aemisegger, F.: The role of air–sea fluxes for the water vapour isotope signals in the cold and warm sectors of extratropical cyclones over the Southern Ocean, *Weather Clim. Dynam.*, 2, 331–357, <https://doi.org/10.5194/wcd-2-331-2021>, 2021.
- Tilzer, M., Gieskes, W., Heusel, R., and Fenton, N.: The impact of phytoplankton on spectral water transparency in the Southern Ocean: implications for primary productivity, *Polar Biol.*, 14, 127–136, <https://doi.org/10.1007/bf00234975>, 1994.
- Toffoli, A., McConochie, J., Ghantous, M., Loffredo, L., and Babanin, A. V.: The effect of wave-induced turbulence on the ocean mixed layer during tropical cyclones: Field observations on the Australian North-West Shelf, *J. Geophys. Res.-Oceans*, 117, <https://doi.org/10.1029/2011JC007780>, 2012.
- Trenberth, K. E. and Fasullo, J. T.: Simulation of Present-Day and Twenty-First-Century Energy Budgets of the Southern Oceans, *J. Climate*, 23, 440–454, <https://doi.org/10.1175/2009JCLI3152.1>, 2010.
- Uchida, T., Balwada, D., Abernathey, R., Prend, C. J., Boss, E., and Gille, S. T.: Southern Ocean Phytoplankton Blooms Observed by Biogeochemical Floats, *J. Geophys. Res.-Oceans*, 124, 7328–7343, <https://doi.org/10.1029/2019JC015355>, 2019.
- Uchida, T., Balwada, D., Abernathey, R., McKinley, G., K. Smith, S., and Lévy, M.: Vertical Eddy Iron Fluxes Support Primary Production in the Open Southern Ocean, *Nat. Commun.*, 11, 1125, <https://doi.org/10.1038/s41467-020-14955-0>, 2020.
- Uemura, R., Matsui, Y., Yoshimura, K., Motoyama, H., and Yoshida, N.: Evidence of Deuterium Excess in Water Vapor as an Indicator of Ocean Surface Conditions, *J. Geophys. Res.-Atmos.*, 113, D19114, <https://doi.org/10.1029/2008JD010209>, 2008.
- Vergara-Temprado, J., Miltenberger, A. K., Furtado, K., Grosvenor, D. P., Shipway, B. J., Hill, A. A., Wilkinson, J. M., Field, P. R., Murray, B. J., and Carslaw, K. S.: Strong Control of Southern Ocean Cloud Reflectivity by Ice-Nucleating Particles, *P. Natl. Acad. Sci. USA*, 115, 2687–2692, <https://doi.org/10.1073/pnas.1721627115>, 2018.
- Vernet, M., Martinson, D., Iannuzzi, R., Stammerjohn, S., Kozłowski, W., Sines, K., Smith, R., and Garibotti, I.: Primary production within the sea-ice zone west of the Antarctic Peninsula: I-Sea ice, summer mixed layer, and irradiance, *Deep-Sea Res. Pt. II*, 55, 2068–2085, <https://doi.org/10.1016/j.dsr2.2008.05.021>, 2008.
- Vichi, M., Eayrs, C., Alberello, A., Bekker, A., Bennetts, L., Holland, D., de Jong, E., Joubert, J., MacHutchon, K., Messori, G., Mojica, J. F., Onorato, M., Sounders, C., Skatulla, S., and Toffoli, A.: Effects of an explosive polar cyclone crossing the Antarctic marginal ice zone, *Geophys. Res. Lett.*, 46, 5948–5958, <https://doi.org/10.1029/2019GL082457>, 2019.
- Vignon, É., Traullé, O., and Berne, A.: On the fine vertical structure of the low troposphere over the coastal margins of East Antarctica, *Atmos. Chem. Phys.*, 19, 4659–4683, <https://doi.org/10.5194/acp-19-4659-2019>, 2019.
- Volpi, M.: sparse-pca-decomposition, GitLab [code], available at: <https://renkulab.io/gitlab/ACE-ASAIID/spca-decomposition> (last access: 29 March 2021), 2021.
- Volpi, M. and Landwehr, S.: sparse-pca-decomposition, Renku [code], available at: <https://renkulab.io/projects/ACE-ASAIID/spca-decomposition> (last access: 29 March 2021), 2021.
- Walland, D. and Simmonds, I.: Baroclinicity, Meridional Temperature Gradients, and the Southern Semiannual Oscillation, *J. Climate*, 12, 3376–3382, [https://doi.org/10.1175/1520-0442\(1999\)012<3376:BMTGAT>2.0.CO;2](https://doi.org/10.1175/1520-0442(1999)012<3376:BMTGAT>2.0.CO;2), 1999.
- Walton, D. W. H. and Thomas, J.: Cruise Report - Antarctic Circumnavigation Expedition (ACE) 20th December 2016 - 19th March 2017, Tech. rep., Zenodo, <https://doi.org/10.5281/zenodo.1443511>, 2018.
- Wanninkhof, R., Asher, W. E., Ho, D. T., Sweeney, C., and McGillis, W. R.: Advances in Quantifying Air-Sea Gas Exchange and Environmental Forcing, *Annu. Rev. Marine Sci.*, 1, 213–244, <https://doi.org/10.1146/annurev.marine.010908.163742>, 2009.
- Weber, T. S. and Deutsch, C.: Ocean nutrient ratios governed by plankton biogeography, *Nature*, 467, 550–554, <https://doi.org/10.1038/nature09403>, 2010.
- Weller, R., Wagenbach, D., Legrand, M., Elsassser, C., Tian-Kunze, X., and König-Langlo, G.: Continuous 25-yr aerosol records at coastal Antarctica - I: inter-annual variability of ionic compounds and links to climate indices, *Tellus B*, 63, 901–919, <https://doi.org/10.1111/j.1600-0889.2011.00542.x>, 2011.
- Welti, A., Müller, K., Fleming, Z. L., and Stratmann, F.: Concentration and variability of ice nuclei in the subtropical maritime boundary layer, *Atmos. Chem. Phys.*, 18, 5307–5320, <https://doi.org/10.5194/acp-18-5307-2018>, 2018.
- Welti, A., Bigg, E. K., DeMott, P. J., Gong, X., Hartmann, M., Harvey, M., Henning, S., Herenz, P., Hill, T. C. J., Hornblow, B., Leck, C., Löffler, M., McCluskey, C. S., Rauker, A. M., Schmale, J., Tatzelt, C., van Pinxteren, M., and Stratmann, F.: Ship-based measurements of ice nuclei concentrations over the

- Arctic, Atlantic, Pacific and Southern oceans, *Atmos. Chem. Phys.*, 20, 15191–15206, <https://doi.org/10.5194/acp-20-15191-2020>, 2020.
- Wilson, S. R.: Characterisation of $J(O^1D)$ at Cape Grim 2000–2005, *Atmos. Chem. Phys.*, 15, 7337–7349, <https://doi.org/10.5194/acp-15-7337-2015>, 2015.
- Wilson, T. W., Ladino, L. A., Alpert, P. A., Breckels, M. N., Brooks, I. M., Browse, J., Burrows, S. M., Carslaw, K. S., Huffman, J. A., Judd, C., Kilhau, W. P., Mason, R. H., McFiggans, G., Miller, L. A., Nájera, J. J., Polishchuk, E., Rae, S., Schiller, C. L., Si, M., Temprado, J. V., Whale, T. F., Wong, J. P. S., Wurl, O., Yakobi-Hancock, J. D., Abbatt, J. P. D., Aller, J. Y., Bertram, A. K., Knopf, D. A., and Murray, B. J.: A marine biogenic source of atmospheric ice-nucleating particles, *Nature*, 525, 234, <https://doi.org/10.1038/nature14986>, 2015.
- Wolf, C., Frickenhaus, S., Kiliyas, E. S., Peeken, I., and Metfies, K.: Regional variability in eukaryotic protist communities in the Amundsen Sea, *Antarct. Sci.*, 25, 741, <https://doi.org/10.1017/s0954102013000229>, 2013.
- Woolhiser, D. A. and Roldán, J.: Stochastic Daily Precipitation Models: 2. A Comparison of Distributions of Amounts, *Water Resour. Res.*, 18, 1461–1468, <https://doi.org/10.1029/WR018i005p01461>, 1982.
- Wright, S. W., van den Enden, R. L., Pearce, I., Davidson, A. T., Scott, F. J., and Westwood, K. J.: Phytoplankton community structure and stocks in the Southern Ocean (30–80 E) determined by CHEMTAX analysis of HPLC pigment signatures, *Deep-Sea Res. Pt II*, 57, 758–778, <https://doi.org/10.1016/j.dsr2.2009.06.015>, 2010.
- Yentsch, C. S. and Ryther, J. H.: Short-Term Variations in Phytoplankton Chlorophyll and Their Significance 1, *Limnol. Oceanogr.*, 2, 140–142, <https://doi.org/10.4319/lo.1957.2.2.0140>, 1957.
- Zamanillo, M., Ortega-Retuerta, E., Nunes, S., Estrada, M., Sala, M. M., Royer, S.-J., López-Sandoval, D. C., Emelianov, M., Vaqué, D., Marrasé, C., and Simó, R.: Distribution of transparent exopolymer particles (TEP) in distinct regions of the Southern Ocean, *Sci. Total Environ.*, 691, 736–748, <https://doi.org/10.1016/j.scitotenv.2019.06.524>, 2019.
- Zou, H., Hastie, T., and Tibshirani, R.: Sparse principal component analysis, *J. Comput. Graph. Stat.*, 15, 265–286, <https://doi.org/10.1198/106186006x113430>, 2006.